Alma Mater Studiorum - Università di Bologna

DIPARTIMENTO DI CHIMICA "G. CIAMICIAN"

Dottorato di Ricerca in SCIENZE CHIMICHE
Ciclo XXVII

Settore concorsuale di afferenza: **03/A2**
Settore scientifico-disciplinare: **CHIM/02**

Computational insight into materials properties

Autore
Dott. **Marco Dallavalle**

Coordinatore Dottorato
Prof. **Aldo Roda**

Relatore
Prof. **Francesco Zerbetto**

Esame Finale Anno 2015

Ai miei genitori.

TABLE OF CONTENTS

List of symbols and abbreviations

CG - coarse-grained

CMC - critical micelle concentration

COM - center of mass

De - Deborah number

DPD - dissipative particle dynamics

FA - focal adhesion

FH - Flory-Huggins

FF - force field

GS - graphene nanosheets

HRTEM - high-resolution transmission electron microscopy

LAB - laser assisted bioprinting

LJ - Lennard-Jones

MC - Monte Carlo

MD - molecular dynamics

MM - molecular mechanics

NTs - nanotubes

PBC - periodic boundary conditions

PDE - partial differential equation

PLGA - poly(lactic-co-glycolic acid)

QEq - charge equilibration model

SDS - sodium dodecylsulfate

WCA - Weeks-Chandler-Andersen

1. Introduction

The desire to predict a property or a state dates back to ancient times. The first set of models to be conceived, it concerned the astronomical cycles. Our ancestors have had to develop an accurate calendar for agricultural reasons. They related the movement of celestial objects to phenomena such as seasons, tides, rain and drought. Multiple astronomical models and calendars were developed by mesoamerican and mesopotamic societies. At the present days, it is possible to model a broad range of physical phenomena, not just limited to the astronomical scale. Reliable models of increasing descriptive and predictive power apply to the molecular level.

However the ability to predict the evolution of a given physical system is not restricted to the formulation of a theory or a model. The advent of computers during the 1950s led to the birth of computer simulations. Computers are able to provide exact results – apart from discretization and numerical errors – for problems which would otherwise be soluble only by approximate methods. [1,2] There are only few non-trivial, exactly soluble problems to be discussed. Already the motion of three interacting particles can not be predicted in terms of an analytical solution. To address a classical many-body problem the help of computers is required. Computers ease the burden of calculation. They can carry out hundred of thousands of repetitive computations within a short time. The current teraflop speed of parallel machines allows for calculations that would require a lifetime's work.

We may consider computer simulations as "virtual laboratory", where perfect control of all parameters can be achieved. Different features of the model can be turned on or off in order to study the effects separately. In that way, it is possible to evaluate the contributing factors that are responsible for the phenomena. Computer simulations provide more than a simple visualization tool of processes at the molecular level. Simulations may have access to details that can prove difficult to study experimentally. In molecular dynamics, for instance, the trajectories and the resulting forces are calculated step-by-step solving the equations of motion. Gathered the information on the motion of the individual atoms, the properties of the material can be inferred, relying on statistical mechanics. A connection is provided between the microscopic and the macroscopic world, between atomic trajectories and properties of experimental interest (equation of state, diffusion, friction, structural order parameters,...).

As trivial as it sounds, computational chemistry is environmentally safe. The properties of a

system can be estimated without actually creating the system. Computer simulations may reduce the number of experiments needed to probe different conditions (solvents, temperatures) or design. We can use computer simulation to investigate a system at very high pressures or temperatures, that are difficult or expensive to inquire. The study of molecules that are too unstable to be studied experimentally is feasible. Information regarding the properties of materials that have not yet been made can be extracted from computer simulations.

Occasionally computer calculations may help to rectify incorrect experimental observations. Probably the most famous example of it, is related to the controversy concerning the structure of the methylene radical (:CH$_2$). Based on spectroscopic experimental data, Gerhard Herzberg, a Nobel laureate, concluded that the methylene radical with two unpaired electrons had a linear geometry. Calculations by Bender and Schaefer demonstrated that CH$_2$ is bend by 135.1°. The predictions were resolved in favour of theory as further experiments confirmed the bend methylene geometry. [3] That lesson proved that theory and experiment can contribute on an equal footing to the scientific debate. As Schaefer stated, *"theoretical chemistry has entered a new stage* […] *with the goal of being no less than full partner with experiment."* [3]

Limits and sources of errors in computational chemistry should not be left out of the picture. Caution is advised when choosing the level of theory, the parameters, and the initial state that applies to the system. Approximations intended to speed calculations can backfire, leading to inconclusive results or artifacts. Errors can be categorized as those due to the software and theory and those caused by the user. As far as the user errors are concerned, they are to be found at the beginning and at the end of the simulation process. The initial setup affects greatly the outcome of the computation. The user may choose a wrong level of coarse-graining, the wrong empirical force field, and so on. Also the late stage of the simulation is prone to errors. The interpretation of the results can be challenging and problematic, especially if it is not possible to compare the results to other theoretical outcomes or to the experimental data. As for the software errors, a good rule of thumbs states that any source code over 200 lines contains at least one error. [2] The reader is referred to the paper of Lipkowitz for an overview of the most common mistakes and pitfalls to avoid when using molecular mechanics. [4]

This dissertation summarizes the research progress over the last three years of PhD activity.

The work was mostly restricted to classical many-body systems, notably molecular dynamics. The aim of the work was to explore its practical applicability at different length and time scales. From nanoparticles system over colloids and polymers to biological systems like membranes and finally living cells, molecular dynamics has been put to the test. Depending on the case a different level of approximation had to be introduced. In order to study a system at the nanometer scale we relied on an atomistic description. At the mesoscopic and microscopic scale we used a coarse-grained approach. Mainly the dissipative particle dynamics thermostat was used.

Most of the results have already been published in peer reviewed journals. Each chapter, set aside the introduction and conclusion, corresponds roughly to a single publication. In the first part of the thesis, the interaction between nanoparticles and amphiphilic molecules is studied. The dispersion of fullerenes by surfactants is described by dissipative particle dynamics simulations (Paper [I]). A systematic study of the effect of the concentration, chain length, and charge of the stabilizer on fullerene aggregation is presented to explain the experimental results and to provide guidelines to understand the incorporation of C_{60} inside micelles. Both neutral and charged amphiphilic molecules are simulated. The long-discussed problem of the location of C_{60} in micelles is addressed and fullerenes are found in the hydrophobic region of the micelles.

We continued the work regarding carbon nanoparticles and amphiphilic molecules by shifting our attention from fullere to graphene. The interactions between graphene sheet of increasing size and phospholipid membrane are quantitatively investigated (Paper [II]). We report that the particle dimension of the graphene nanosheet strongly affects the final equilibrium configuration in the bilayer. Small graphene sheets pierce through without altering the order of the phospholipids. Larger sheets lie flat on the membrane surface leading to the upturning of phospholipids. The translocation from one layer to the other of multiple phospholipids is triggered by the adsorption of the graphene flake.

Next we focused on a material well-known for its tribological properties, molybdenum disulfide. A model is proposed to study structure, stability, and dynamics of MoS_2 (Paper [III]). We simulate the telescopic movement of nested nanotubes and the sliding of MoS_2 layers. The friction coefficient is calculated via Amontons and Green-Kubo formalism. In the idealized system, i.e. without defects, junctions, vacancies, asperities, and impurities, both models find a superlubrication regime, in agreement with some experiments. The picture that

emerges is that in nanotubes friction is an order of magnitude lower than in the layered systems.The calculations also show that there is a substantial stabilization for the formation of nested MoS$_2$ nanotubes with at least four walls.

In Paper [IV] we addressed the question: „is it possible to develop a mesoscopic simulation technique to model the interaction of cells with organic surfaces and devices?" To this end, we tested a soft-matter bead-based approach. Through DPD simulations, we showed that our model is able to portray distinctive features of cells. The simulated cells do not fuse when thay are in contact, their trajectories are not Brownian, they can be made to secrete molecules. We theoretically assessed the effect of the surface properties on the adhesion dynamics of cells. The adhesiveness of the cell is measured by the spreading of the cell soft beads onto the surface. Both a theoretical and an experimental perspective on the problem is provided. In the frame of the iONE FP7 project, the model predictions are validated with experimental data collected by Scriba nanotecnologie srl consortium partner.

Finally a mathematical model to gain understaning of the coupled diffusion-swelling process in poly(lactic-co-glycolic acid), PLGA, is proposed (Paper [V]). The model is solved numerically using the finite element method. The model explicity describes swelling. It is able to portray a range of diffusional behaviours, from Fickian to Case II. Non-ideal concentration effects on the diffusion coefficient can be included. In more detail, the numerical scheme is able to describe three regimes of the PLGA behaviour: initial swelling, relaxation, final swelling. The results were compared to the experimental data collected at CSIC.

In summary this thesis deals with a very diverse set of materials. Metal dichalcogenides, carbon materials, polymers, even cells, are considered from a computational standpoint. Each of these models comes along with its own limits and features. My work was mostly restricted to classical many-body systems. It was rather surprising to discover that, in a science where so much of the debate concerns quantum mechanics, classical mechanics is that effective in explaining important chemical phenomena.

2. Computational methods

A short introduction is provided to classical molecular dynamics (MD) and its theoretical background. In this section I present an overview of the main features of molecular dynamics, including integration algorithms, force fields and thermostats. Dissipative particle dynamics is introduced as a thermostat to molecular dynamics. Technical details of the simulation performed during the PhD study are described.

2.1 Classical MD simulations

The primary aim of molecular dynamics is to compute the equilibrium and off-equilibrium properties of classical many body systems. The term *classical* means that the motion of the particles of the system obeys the laws of classical mechanics. Everything that underlies the laws of quantum physics is neglected. Electrons are not present explicitly, they are introduced through the potential energy surface that is a function of the atomic positions only. The approximation holds as long as the translational, rotational or vibrational particle's motion has a frequency ν such that $h\nu < k_B T$. All atoms and molecules, except for the lightest ones such as He, Ne, H_2, D_2, fulfill this requirement.

In molecular dynamics the time evolution of an ensemble of interacting particles is followed via the solution of the equations of motion. Particles usually correspond to atoms, although they may represent portions of fluid or specific chemical groups that can be described in terms of a given interaction law. The choice of the formalism adopted to describe the equations of motion is mostly dictated by considerations of convenience. Newtonian mechanics represents the most intuitive one, since its equations directly relate to the macroscopic world. In the Lagrange's formalism the mechanics of a system is described in terms of generalized, not necessarily Cartesian, coordinates, which can be helpful to handle certain problems. The Hamiltonian's formalism provides an easier way to introduce aspects of quantum mechanics with respect to the formulations of other mechanics. Nevertheless different formulations of mechanics yield identical result. [1] Here the Newtonian formalism is adopted,

$$m \frac{d^2 r_i}{dt^2} = F_i \left(r_1, r_2, \ldots, r_N \right), \quad i = 1, 2, \ldots, N \quad (1)$$

where r_i are the position vectors and F_i the forces acting upon the N particles in the system. The microscopic state of the system is defined by the position and momentum of each particle

of the system at every time. Whenever a particle changes its position, or whenever any of the other particles with which it interacts changes position, the force acting on the particle will change accordingly. The forces are used to determine the updated accelerations and velocities. As the particles move, their trajectories may be displayed and analysed. However we are not interested in trajectories of individual atoms. Two configurations which are almost identical or very close at the beginning of the calculations will diverge exponentially with time (Lyapunov instability). [2] This could be seen as a serious blow to the prediction ability of molecular dynamics, but there is no need to obtain the exact trajectory of a single given particle. We do not have to calculate the orbit of a satellite or a spacecraft. MD is interested in statistical predictions and averaged properties are computed. Under hypothesis of ergodicity, it is possible to assume that the temporal average of an observable along a trajectory is equivalent to the ensemble-average over the phase space,

$$\langle A \rangle = \frac{1}{\tau} \int_0^{\tau} A(t) dt = \frac{1}{M} \sum_i^M A_i \quad (2)$$

where A is the observable, M the number of microstates constituting the ensemble, and τ is the total simulation time. [5] A stochastic process is said to be ergodic if all accessible microstates are equiprobable over a long period of time. This condition is fulfilled for τ e M $\rightarrow \infty$. From an operational point of view, for an ergodic process the autocorrelation function of the given observable tends to zero.

Any observable has to be expressed as a function of the positions and momenta of the particles in the system. For example, a convenient definition of the temperature is provided by equation 3. Temperature is related to the kinetic energy via the particle's momenta.

$$E_{kin} = \frac{\sum_{i=1}^N |p_i|^2}{2 m_i} = \frac{k_B T N_f}{2} \quad (3)$$

where N_f is the number of degrees of freedom (for a system of N particles with fixed total momentum $N_f = 3N-3$) and k_B is the Boltzmann constant.

2.2 Integration Algorithms

In molecular dynamics, the configurations of the system are obtained by integrating the equation of motion. The movements of all the particles are coupled togheter, leading to a many-body problem that cannot be solved analytically. For that reason the equations of motion are integrated using a finite difference approach. Several algorithm have been designed for integrating the equation of motion, all assuming that the positions and dynamical properties (velocities, accelerations,...) of the system can be approximated by a Taylor series expansions:

$$r(t+\delta t)=r(t)+\delta t v(t)+\frac{1}{2}\delta t^2 a(t)+\frac{1}{6}\delta t^3 b(t)+\frac{1}{24}\delta t^4 c(t)+\ldots \quad (4)$$

$$v(t+\delta t)=v(t)+\delta t a(t)+\frac{1}{2}\delta t^2 b(t)+\frac{1}{6}\delta t^3 c(t)+\ldots \quad (5)$$

$$a(t+\delta t)=a(t)+\delta t b(t)+\frac{1}{2}\delta t^2 c(t)+\ldots \quad (6)$$

$$b(t+\delta t)=b(t)+\delta t c(t)+\ldots \quad (7)$$

where v is the velocity (first derivative of position with respect to the time), a is the acceleration (second derivative), c is the third derivative and so on. The order of an integration algorithm is the degree to which Taylor series is approximated. It is the lowest term that is not included in the expansion. [5] If the expansion in equation 4 is truncated beyond the term δt^2, the Euler algorithm is obtained. Such algorithm suffers from energy drift issues and therefore is not recommended. [2] On the other hand, one of the most common implementations is given by the so-called Verlet algorithm. [6] The highest order derivative that appears in the Verlet formulae is the third-order term, so the Verlet is a fourth-order integration algorithm. This method uses the positions and accelerations at time t, and the positions from the previous step, r(t-δt), to calculate the new positions r(t+δt) at the time t+δt.

$$r(t+\delta t)=r(t)+\delta t v(t)+\frac{1}{2}\delta t^2 a(t)+\frac{1}{6}\delta t^3 b(t)+O(\delta t^4) \quad (8)$$

$$r(t-\delta t)=r(t)-\delta t v(t)+\frac{1}{2}\delta t^2 a(t)-\frac{1}{6}\delta t^3 b(t)+O(\delta t^4) \quad (9)$$

Summing the two equations the first and third-order terms from the Taylor expansion cancel out and one obtains,

$$r(t+\delta t)=2r(t)-r(t-\delta t)+\delta t^2 a(t)+O(\delta t^4) \quad (10)$$

The position estimated through equation 10 is correct except for errors of order δt^4. In the

Verlet integration algorithm velocities do not appear explicitly. It is possible to derive the velocity from knowledge of the trajectory using,

$$v(t) = \frac{r(t+\delta t) - r(t-\delta t)}{2\delta t} + O(\delta t^2) \quad (11)$$

Velocities are subject to errors of order δt^2. The errors are cumulative, as each step uses values produced by the previous step. Several variations of the Verlet algorithm have been proposed. An explicit inclusion of velocities was accomplished by the leap frog algorithm [7], and further developments lead to the velocity Verlet [8] and Beeman [9] scheme. The velocity Verlet algorithm is algebraically equivalent to the original one, but provides both the particle's position and velocity at the same time. It computes the particle velocity and position as follows,

$$r(t+\delta t) = r(t) + v(t)\delta t + \frac{1}{2}a(t)\delta t^2 \quad (12)$$

$$v(t+\delta t) = v(t) - \frac{1}{2}[a(t) + a(t+\delta t)]\delta t \quad (13)$$

It may resemble the Euler scheme, in the way it truncates the Taylor expansion. However the update of the velocities is different, using,

$$v\left(t+\frac{1}{2}\delta t\right) = v(t) - \frac{1}{2}a(t)\delta t \quad (14)$$

The overall scheme of Verlet, leap frog and velocity Verlet integration scheme is illustrated in Figure 2.1. Another Verlet-like algorithm is the Beeman scheme. Compared to Verlet it uses a more accurate expression for the determination of the velocities at the expense of a slightly increased computational effort. As a consequence of the more accurate expression for the velocity, the total energy conservation is better described.

$$r(t+\delta t) = r(t) + v(t)\delta t + \frac{2}{3}a(t)\delta t^2 - \frac{1}{6}a(t-\delta t)\delta t^2 \quad (15)$$

$$v(t+\delta t) = v(t) + \frac{1}{3}a(t)\delta t + \frac{5}{6}a(t)\delta t - \frac{1}{6}a(t-\delta t)\delta t^2 \quad (16)$$

For most molecular dynamics calculations, the Verlet-like algorithm ensures adequate accuracy, while being stable and "robust". An integration algorithm is required to provide a good approximation to the true trajectory (accuracy), has to avoid perturbations generating numerical instabilities (stability) and should allow integrations for relatively long time steps (robustness). A good algorithm should also be computationally efficient (low memory

requirements, fast execution) and has to be easy to implement.

We chose the Beeman algorithm to integrate the equation of motion to simulate the friction dynamics of molybdenum disulphide. The employed coefficients are Brooks' "Better Beeman" values [10]. While to study the interactions of nanoparticle and amphiphilic molecules we resorted to a modified velocity−Verlet scheme. [1] In contrast to the non-modified version of the velocity−Verlet, the modified algorithm follows a predictor-corrector procedure,

$$r(t+\delta t)=r(t)+v(t)\delta t+\frac{1}{2}f(t)\delta t^2 \quad (17)$$

$$\tilde{v}(t+\delta t)=v(t)+\lambda f(t)\delta t \quad (18)$$

$$f(t+\delta t)=f(r(t+\delta t),\tilde{v}(t+\delta t)) \quad (19)$$

$$v(t+\delta t)=v(t)+\frac{1}{2}(f(t)+f(t+\delta t))\delta t \quad (20)$$

A prediction for the velocity, denoted by $\tilde{v}$, is introduced and corrected afterwards in the last step. This integration scheme is considered the most suitable algorithm for dissipative particle dynamics simulation. [11]. The modified integration algorithm by Groot and Warren prevents the temperature drifts observed in the first dissipative particle dynamics calculations. It progressively replaced the original algorithm employed by Hoogerbrugge and Koleman. [12] The variable λ is added to the algorithm to account for the effects of stochastic interactions. Usually λ is set to ½.
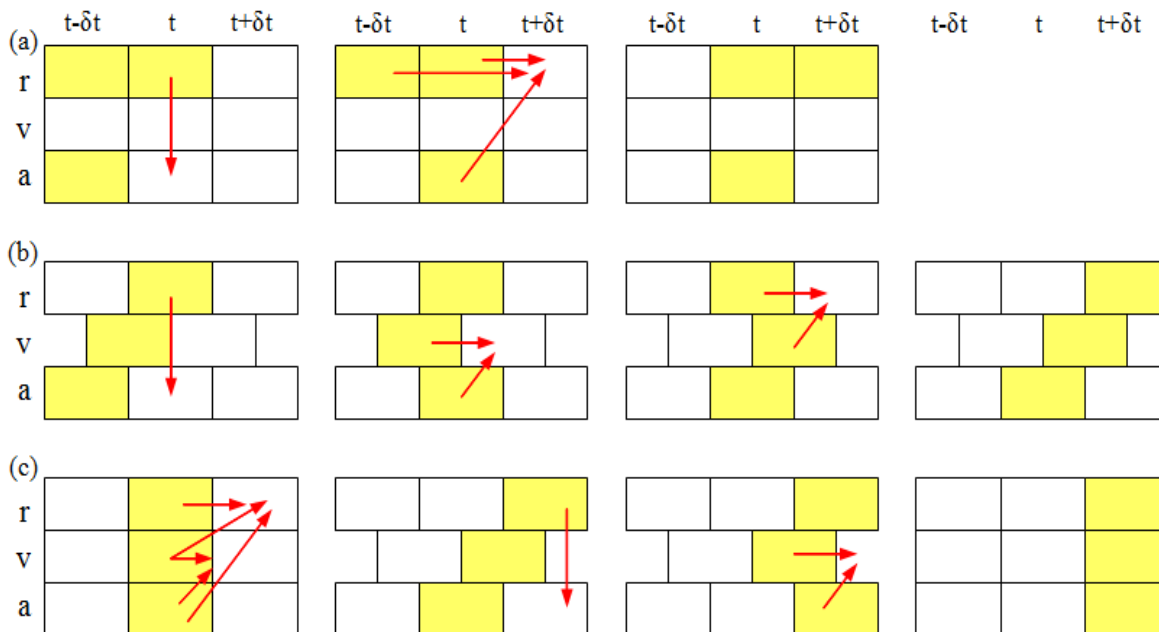
Figure 2.1 Three forms of the Verlet algorithm are shown: (a) Verlet's original method, (b) the leap-frog form, (c) the velocity form. Successive steps in the implementation of each algorithm are illustarted. The stored variables are depicted as yellow boxes.

2.3 Empirical force fields – atomistic description

The most time consuming part of a molecular dynamics simulation is the computation of the forces. We have to calculate the net force acting on every particle at each time step. In a N-particle system the forces are computed from a potential energy function $V(r_1,r_2,…,r_N)$ that depends on the positions of all N particles.

$$F_i = -\frac{\delta V}{\delta r_i} \quad (21)$$

It is possible to discuss MD in terms of either forces or potentials. The potential energy function V encloses all the information of the system. Given one potential, the particles are able to represent a dilute noble gas, given another, they might stand for covalently bonded atoms in a chromophore. A potential energy function may account for structural features like bond lengths, bond angles, electrostatic interactions and so on. The combination of these potential energy functions is called force field (FF). Molecular dynamics, like Monte Carlo (MC) and Molecular mechanics (MM), implement an empirical force field for what they need to accomplish. A force field used for an MM calculation can be usually employed in an MD simulation and vice versa. Sometimes *force field* and *Molecular mechanics* are considered as

synonyms. In this thesis we choose the point of view of Lipkowitz [4], who underlines how MM uses, but is not, an empirical force field. Molecular dynamics is often referred to as a subcategory of Molecular mechanics. Here we go with a different definition. MM can be seen as a computational tool for determining molecular structures and energies. It explores selected points on a potential energy surface, by performing energy minimization. In this strategy atoms are assumed to be at rest, that is to say, they have zero kinetic energy. Molecular mechanics provides a static point of view to the chemist. In the broadest sense, MD is concerned with particles motion. Molecular Dynamics, as the name implies, contributes with a dynamic description of the system.

There are no strict rules regarding how many or what types of potential should be used in an empirical force field. One can argue that the problem of modeling a system can be sometimes summarized as a search for an appropriate potential for that system. Several FF have been developed over the years, each of them featuring different formulations for the energy terms. The main contribution to a force field are usually grouped into covalent and non-covalent terms.

$$V_{TOT} = V_{COVALENT} + V_{NONCOVALENT} \quad (22)$$

$$V_{TOT} = \left(V_{STRETCHING} + V_{BENDING} + V_{TORSION} \right) + \left(V_{ELECTROSTATIC} + V_{VDW} \right) \quad (23)$$

A functional form of a widely used FF, the Amber Force Field [13], is

$$V_{TOT} = \left\{ \sum_i^N k_r \left(r - r_{eq} \right)^2 + \sum_i^N k_\theta \left(\theta - \theta_{eq} \right)^2 + \sum_i^N \frac{V_n}{2} \left[1 + \cos \left(n\varphi - \gamma \right) \right] \right\}$$
$$\left(+ \sum_{i<j} 4 \varepsilon_{ij} \left[\left(\frac{\sigma_{ij}}{R_{ij}} \right)^{12} - \left(\frac{\sigma_{ij}}{R_{ij}} \right)^6 \right] + \sum_{i<j} \frac{q_i q_j}{\varepsilon R_{ij}} \right) \quad (24)$$

The first and the second term account for stretching and bending contributions. They are expressed by harmonic potentials, with r_{eq} being the equilibrium bond length, θ_{eq} the equilibrium bond angle, k_r and k_θ the Hooke's spring constant. The third term is a torsional potential that represents how the energy changes as a bond rotates, where the V_n parameter controls the amplitude of the curve, the n parameter controls its periodicity and reflects the type symmetry in the dihedral angle, and γ shifts the curve along the rotation angle axis φ. The fourth term is a Lennard-Jones (LJ) potential accounting for van der Waals interactions between two atoms at distance R_{ij}, where ε_{ij} controls the well depth and σ_{ij} the collision diameter. The attractive long-range term r^{-6} describes attraction at long ranges (van der Waals

force, or dispersion force) and has a clear physical justification. The repulsive r^{-12} term accounts for the Pauli repulsion at short ranges due to overlapping electron orbitals. Occasionally the repulsive term is less steep, following a r^{-10}, r^{-8} rule. The final term describes the Coulombic interaction between two partial atomic charges q_i and q_j, set at a given distance R_{ij}, with ε as the permittivity. More complex force field can include additional term, e.g. in order to explicitly model hydrogen bonding or π-π interaction. Each force field comes with its own definition of atom types. In an atomistic setup, atom types are classifications based on element and bonding environment. They contain information about the hybridization state and the surrounding region of the atom. Each atom type is characterized by a set of parameters.

A force field can be parameterized based on experimental structural information and energies. Bond lengths, angles and spring constants can be fitted to spectroscopic data allowing to reproduce the frequencies of a given set of molecules. Force fields can be parameterized from the results of high-level quantum-chemical, ab initio or semi-empirical calculations as well.

In our case, a parametrization work is carried out to study the tribological properties of molybdenum disulfide. [III] A two-body term in the form of the Lennard-Jones potential, supplemented by a description of Coulomb interatomic interactions, is adopted. A description of the atomistic model is included in the fifth section of the thesis. The potential employed to simulate the dispersion of the fullerenes and the graphene are simple soft-sphere potential. [I,II] Pairwise all-atom potentials are computationally still too expensive for many applications and often place serious limitations on the scale of MD simulations. To access larger simulated time scales and system sizes a further simplification of the molecular models is required.

2.4 Empirical force fields – coarse-grained description

Computer simulations allow the study of many-particle systems. If we had infinite computing power at our disposal, it would be possible to perfom simulations that could provide us with the exact equilibrium properties of the system of interest. To date the largest atomistic calculations simulated 10^{12} Lennard-Jones atoms arranged into a simple cubic lattice [14]. The "record" simulation has been performed on 212,992 processors of LLNL's BlueGene/L cluster. The test run took around 30 minutes for only 40 timesteps of integration. However real systems comprise more than 10^{23} atoms. Even a trillion-atom molecular dynamics falls

short to describe a system for relevant length scales. The incremental approach where the larger the system and the longer the simulation, the better the results, is not the only way to proceed. It is possible to follow an approximate scheme, in which the number of degrees of freedom is reduced by clustering individual atoms into larger particles. Such coarse-grained (CG) approach allows to properly represent the system at the mesoscale. The loss in term of degree of freedom can be somewhat excused. By cutting down the number of solvent particles we mostly eliminate "uninteresting degrees of freedom". Often significant phenomena appear only on time scales larger than the motion of individual solvent particles. Due to the reduction in the degrees of freedom and elimination of fine interaction details, the simulation system requires less resources. Coarse-grained interactions are usually smoother, simplifying the energy landscape and allowing larger time step in integration. As a result, an increase of orders of magnitude in the simulated time and length scales can be obtained.

CG models are usually used to explore the area of the mesoscopic realm.The behavior of complex fluids like colloids and polymer melts can be simulated at the coarse-grained level. CG models are easily adapted for atomistically homogenous systems, consisting of repetitive structures such as carbon nanotubes (with a uniform cylindrical structure). Another key attractive feature of CG simulation is the possibility to describe membrane and protein dynamics.

Multiple methodologies have been developed to systematically derive coarse-grained force fields from the underlying atomistic-scale forces. [15-19] Español et al. proposed a coarse-graining procedure in which a set of Weeks-Chandler-Andersen (WCA) particles are lumped together into beads and the conservative force field is derived. [16] The WCA potential is a shifted Lennard-Jones potential truncated at the position of minimum potential energy. The WCA potential is hard and purely repulsive. Español et al. linked the radial distribution function g(r) to the potential of mean force V(r) as,

$$g(r) = e^{-[V(r)/k_B T]} \quad (25)$$

By running multiple simulations at a different degree of coarse-graining , they computed the radial distribution function and the corresponding potential of mean force. They found that the function that best fits the potential mean force is,

$$V(r) = \frac{V_0}{\cosh(r/R_0)} \quad (26)$$

where V_0 is the height of the energy barrier and R_0 represents the range of the potential. V_0 has

to assume finite values as the particles should be able to "interpenetrate." The potential is termed as soft to distinguish it from the hard core description of atomistic potentials. A comparison between hard and soft potentials is provided in Figure 2.2. Different methods for systematic (bottom-up) molecular coarse-graining have emerged, varying in the degree of coarse-graining and the "rule" that the coarse-graining procedure follows. They all share the approach of averaging the molecular field over the rapidly fluctuating motions of atoms during short time intervals to obtain an effective potential.
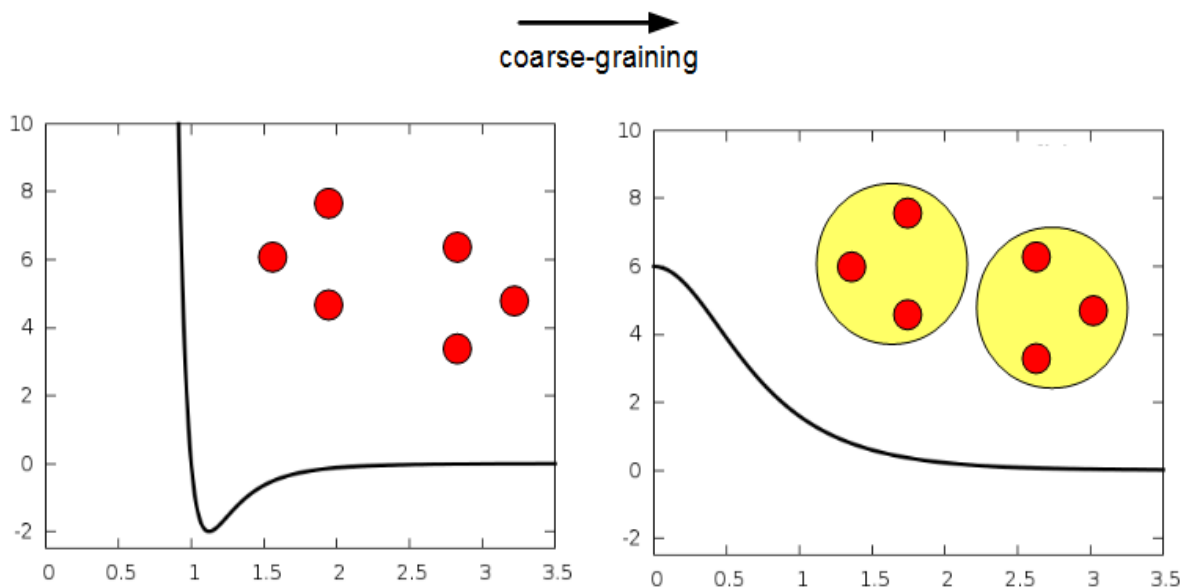

Figure 2.2 The process of coarse-graining groups atoms or collection of molecules into beads. They interact with each other through soft, repulsive-only, pairwise forces.

2.5 Dissipative particle dynamics

Dissipative particle dynamics (DPD) is, as the name suggests, a particle based simulation method that includes friction and noise terms. It provides a computationally cheap, off-lattice description of fluid and soft materials. Dissipative particle dynamics can be considered as a thermostat to molecular dynamics.

DPD is soon to be 23 years old. It has been originally proposed by Hoogerbrugge and Koelman [12], while Español and Warren revised the algorithm to reproduce a well-defined NVT ensemble. [20] At first, a crude Euler algorithm has been implemented, which led to a dependence of equilibrium properties to the time step. Groot and Warren rectified the issue by introducing a modified version of velocity-Verlet algorithm. [11] In 2003, Groot added the electrostatic interactions into the DPD scheme by using a variant of the particle-particle

particle-mesh (PPPM) approach. [21]

In dissipative particle dynamics the force acting on a particle is given by the sum of a conservative force, a dissipative force and a random force. The forces are assumed to be pairwise additive.

$$F_i = \sum_{i \neq j} \left(F_{ij}^C + F_{ij}^D + F_{ij}^R \right) \quad (27)$$

A force acting on an object is said to be conservative if it is function of the position only. The conservative force is described as

$$F_{ij}^C = f_{ij}^C \left(r_{ij} \right) \hat{r}_{ij} \quad (28)$$

where f_{ij}^C is a repulsive scalar function, $r_{ij} = r_j - r_i$ is the instantaneous particle separation and $\hat{r}_{ij} = r_j - r_i / \left(r_{ij} \right)$ is the unit vector from particles i to j. The repulsive scalar function is frequently taken as a soft repulsion term of the form,

$$f_{ij}^C = \begin{cases} a_{ij} \left(1 - r_{ij} / r_c \right) \hat{r}_{ij}; & r_{ij} < r_c \\ 0; & r_{ij} > r_c \end{cases} \quad (29)$$

where a_{ij} is the maximum repulsion parameter between particles i and j, and r_c is the cutoff distance, which is usually adopted as the unit of length in simulations. Additional conservative forces can be included. For example beads that belong to the same molecule may be connected by harmonic springs.

The second term is a dissipative force between the particles that is meant to describe the viscous resistance in a fluid. The force reduces velocity differences between particles and is described by,

$$F_{ij}^D = -\gamma \omega^D \left(r_{ij} \right) \left(\hat{r}_{ij} v_{ij} \right) \hat{r}_{ij} \quad (30)$$

F_{ij}^D is proportional to the relative velocities $v_{ij} = v_j - v_i$. If particle j moves towards particle i, the scalar product $\hat{r}_{ij} v_{ij}$ turns negative and the particle i and j repel each other. The coefficient γ controls the magnitude of the dissipative force and can be seen as a friction constant. ω_D represents the variation of the friction coefficient over distance.

The random force represents the thermal or vibrational energy of system. It is of the form,

$$F_{ij}^R = -\sigma \omega^R \left(r_{ij} \right) \hat{r}_{ij} \xi_{ij} \quad (31)$$

where σ is the amplitude of the statistical noise, ξ_{ij} is a random variable uniformly distributed between 0 and 1 with zero mean and unit variance (white noise), ω^R describes the variation of the random force with distance. Groot and Warren proved the integration algortithm to be

unstable for σ > 8. [11] The weights functions ω^D and ω^R cannot be chosen independently but must be coupled together through a fluctuation-dissipation relation. Two conditions on the weight functions and the amplitudes of the dissipative and random forces are set,

$$\omega^D = \left[\omega^R\right]^2 \quad (32)$$

and

$$\sigma^2 = 2\gamma k_B T \quad (33)$$

where k_B is the Boltzmann constant and T is the temperature. Equation 32 and 33 describe the fluctuation-dissipation theorem in the frame of dissipative particle dynamics. This relations ensure proper thermodynamic equilibrium conditions and generate a canonical ensemble distribution (NVT). The weight functions are selected as functions that decrease linearly or quadratically to zero at the cutoff distance r_c. For historical reasons ω^D and ω^R are similar in form to the conservative scalar function and we have that

$$\omega^D = \left[\omega^R\right]^2 = \begin{cases} \left(1 - r_{ij}/r_c\right); & r_{ij} < r_c \\ 0; & r_{ij} > r_c \end{cases} \quad (34)$$

The dissipative and the random force act as a heat sink and as a source. The dissipative contribution cools the system while the random term heats the particles. Their combined effect is a thermostat. The main features of the dissipative particle dynamics thermostat are three: (i) it conserves linear momentum, (ii) it conserves angular momentum, (iii) it is Galilean invariant. As the DPD thermostat is Galilean invariant, it does not see the translational motion of the particles as an increase in temperature (which for example the Nose-Hoover does). [22] The DPD thermostat captures momentum and mass conservation, which are responsible for the hydrodynamic behaviour of a fluid at large scales. [23]

Dissipative particle dynamics can be considered as a momentum-conserving thermostat completely decoupled from any arbitrary conservative potential. It is legitimate to use DPD for simulations with either soft or hard particles. [22] However DPD uses mostly soft particles, called beads, coarse-graining group of atoms or collection of molecules togheter. The introduction of a dissipative and a random force in DPD can be seen as a result of the coarse-graining process. There "*is a very general theme in non-equilibrium statistical mechanics: whenever a coarse-graining description is performed in such a way that the microscopic variables are eliminated in terms of a fewer number of macroscopic (or mesoscopic) variables, then the eliminated degrees of freedom show up in the dynamics of the*

macroscopic variables in the form of dissipation and noise." [16]

If we choose to use equation 29 to describe the conservative forces of the system, the repulsion parameter *a* has to be defined. Probably the most cited work in the DPD area is that of Groot and Warren [11] who specified the repulsion parameter between particles of the same type, a_{ii}, and between particle of a different type, a_{ij}. The compressibility of water is employed as reference parameter to deduce the effective interactions between DPD fluid particles. The dimensionless reciprocal compressibility κ^{-1} describes correctly the thermodynamic state of an arbitrary liquid when,

$$\kappa^{-1} = \frac{1}{\rho k_B T \kappa_T} = \frac{1}{k_B T} \left(\frac{\delta P}{\delta \rho} \right)_T \quad (35)$$

where ρ is the numerical density of the molecules, P is the pressure and κ_T stands for the isothermal compressibility of the liquid. Groot and Warren showed that the DPD equation of state can be approximated for sufficiently high density ($\rho > 2$) to [11]

$$P = \rho k_B T + a_{ii} \alpha \rho^2 \quad (\alpha = 0.101 \pm 0.001) \quad (36)$$

which led to a dimensionless reciprocal compressibility of

$$\kappa^{-1} \approx 1 + \frac{0.2 a_{ii} \rho}{k_B T} \quad (37)$$

Water has a compressibility of $\kappa^{-1} = 15.9835$ at room temperature (300 K). The soft-repulsive parameter for pure water can be expressed as,

$$a_{ii} = \frac{75 k_B T}{\rho} \quad (38)$$

The approximation holds for $\rho > 2$ and since the required CPU time per timestep increases with the square of the density, ρ is usually set to 3. To reproduce the compressibility of water the repulsion parameter is chosen as $a_{ii} = 25 k_B T$. The reader is referred to the original paper for more details. [11]

In order to consider the interactions in a fluid mixture between different types of dissipative particles the repulsion parameters a_{ij} has to be further defined. The process laid out by Groot and Warren linked the a_{ij} parameter to a_{ii} and to the exchange parameter χ_{ij}. [11] The exchange parameter represents the energetic cost of beginning with a system of pure i and j, and transferring a particle of j into a medium of pure i's and one i into a medium of pure j's. [24] When i and j are two components that do not favor mixing the exchange parameter χ_{ij} is positive; when they favor each other over ii and jj interactions, then it is negative. The

exchange parameter can be traced back to Hildebrand's theory of real solutions or to the Flory-Huggins (FH) theory. [24] The Flory-Huggins theory presents a lattice thermodynamic model for polymer solutions. The free mixing energy F_{mix} for a binary system which contains two components i and j equals,

$$\frac{F_{mix}}{k_B T} = \frac{\phi_i}{N_i} \ln \phi_i + \frac{\phi_j}{N_j} \ln \phi_j + \chi_{ij} \phi_i \phi_j \quad (39)$$

where N_i and N_j are the number of segments per i and j polymer, and ϕ_i and ϕ_j are volume fractions of i and j components with $\phi_i + \phi_j = 1$. From the equation of state 36, the following relation for a DPD fluid is inferred,

$$\rho k_B T + 0.1 a_{ii} k_B T \rho^2 = P = -\left(\frac{\delta F}{\delta V}\right)_T = -V \frac{\delta f_v}{\delta V} - f_v = \rho \frac{\delta f_v}{\delta \rho} - f_v \quad (40)$$

The free energy per volume f_v can be rewritten as,

$$\frac{f_v}{\rho k_B T} = \phi_i \ln \phi_i + \phi_j \ln \phi_j + \chi_{ij} \phi_i \phi_j + c \quad (41)$$

As one can see from that, the free energy per volume can be expressed in a way that is close to the Flory-Huggins description of the free energy per site. Groot and Warren determined a linear dependency between the FH exchange parameter and a_{ij}.

$$a_{ij} = a_{ii} + K_D(\rho) \chi_{ij} \quad (42)$$

where the constant K_D depends on the density (for $\rho=3$, $K_D=3.497$, for $\rho=5$, $K_D=1.451$).

The mapping scheme between the FH exchange parameter χ_{ij} and the DPD repulsion parameter a_{ij} provides a solid background to the soft-potential commonly used in DPD. A direct connection to polymer statistical mechanics is established.

The exchange parameter for polymers is often determined experimentally. It can be estimated from solubility parameters by the formula [25]

$$\chi_{ij} = \frac{V}{RT} (\delta_i - \delta_j)^2 \quad (43)$$

where V is the molar volume of the polymer, R is the univeral gas constant and δ_i, δ_j are the solubility parameters. Alternatively the exchange parameter is measured by spectroscopic ellipsometry, [26] or derived by processing atomic force microscopy images. [27]

2.6 Applications of dissipative particle dynamics

DPD is not limited to the simulation of fluids and polymer solutions. Solid objects of arbitrary shapes, such as colloidal particles, can be inserted in the fluid environment of the model. The

idea to simulate hard-sphere suspensions using dissipative particle dynamics was pioneered by Koelman and Hoogerbrugge [28] and has been explored in more detail by Boek et al. [29] Colloidal particles are built by freezing fluid particles within a given cut off distance and moving those beads as a rigid body, according to the equations of motion. For volume fractions of colloidal particles up to 30% the simulation results compare very well with experiments. At higher volume fractions unphysical interactions are reported. Solvent beads are cleared away from the region in between two colloidal particles. Rigid particles tend to get close to one another, to the point where they can be considered as "anchored". This leads to an increase in viscosity. So it is usually advised to simulate dilute colloidal suspensions rather than systems with high concentration of colloids. [29]

In this dissertation fullerene and graphene particles are modeled following Koelman and Hoogerbrugge scheme. [I,II] DPD has been successfully validated for studying interactions and self-assembly of amphiphilic molecules and carbon nanoparticles. [30] In the third section a computational strategy to describe the dispersion of C_{60} by surfactants is presented. The interactions between the particles in the solution are described by the soft-repulsive a_{ij} parameters in Table 2.1. These parameters worked well to reproduce the experimental self-assembly of surfactants with carbon nanotubes. [30] A similar set of parameters has been adopted to study the interactions between lipid bilayer and graphene flakes (Table 2.2). The structural components of the membrane are phospolipids, which are represented by three linearly connected hydrophilic soft beads that describe the polar region, and two tails of six hydrophobic soft beads. Amphiphiles possessing two hydrophobic tails require three or more head beads to shield the tails from the surrounding solvent, and form a well-ordered bilayer. [31] DPD parameters for the phospholipids were taken from the accurate model of Shillcock and Lipowsky that is capable of reproducing the structural properties and the stress profile of bilayers. [31] Phospolipids are constructed by tying beads together using Hookean springs with the potential

$$U_2(i,i+1) = \frac{1}{2k_2}\left(\left(r_{i,i+1} - l_0\right)\right)^2 \quad (44)$$

where i, i + 1 represents adjacent beads in the phospolipids. The spring constant, k_2, and unstretched length, l_0, are chosen so as to fix the average bond length to a desired value. Both parameters may be specified independently for each bead pair, allowing a bond strength to vary along its length. Chain stiffness is modeled by a three-body potential acting between

adjacent bead triples in a chain,

$$U_3(i-1,i,i+1)=k_3\left[1-\cos\left(\Phi-\Phi_0\right)\right] \quad (45)$$

where the angle Φ is defined by the scalar product of the two bonds connecting beads $i-1$, i, and i, $i+1$. The bending constant, k_3, and preferred angle, Φ_0, may be specified independently for different bead triples (Table 2.3).

Table 2.1 The a_{ij} parameters that determine the magnitude of the repulsion force between particles i and j (see equation 29) for the interaction between fullerene and amphiphilic molecules are presented. a_{ij} has unit $k_B T/r_c$.

	water	surfactant head	surfactant tail	fullerene
water	25	25	80	80
surfactant head	25	27	40	40
surfactant tail	80	40	25	25
fullerene	80	40	25	25

Table 2.2 The a_{ij} parameters that determine the magnitude of the repulsion force between particles i and j (see equation 29) for the interaction between graphene and phospolipids are presented. a_{ij} has unit $k_B T/r_c$.

	phospolipid head	phospolipid tail	water	graphene
phospolipid head	25	50	35	50
phospolipid tail	50	25	75	30
water	35	75	25	75
graphene	50	30	75	25

Table 2.3 Hookean spring force constants (see equation 44 and 45)

bond	k_2	l_0
head head	128	0.5
head tail	128	0.5
tail tail	128	0.5
angle	k_3	Φ_0
tail tail tail	20	180
head tail tail	20	180

Beyond the classical applications of dissipative particle dynamics, various cell models have been proposed. The cell model by Fedosov attempts to capture the main biophysical characteristics of human red blood cells. [32-34] A cell is described as a collection of beads immersed in a fluid. The cell particles interact with the fluid particles through soft potentials, while the temperature of the system is controlled by the DPD thermostat. An additional contribution provides membrane elasticity similar to that of a spectrin network of erythrocyte membrane. Fedosov's scheme is able to predict the cell mechanics, rheology, and microcirculation in agreement with experiments. [32,33] It provides an adequate representation of malaria-infected cell. [34]

In this thesis we present a simple model that describes the interactions of the outer layer of cells with the surfaces of materials. [IV] The beads are described by (very) few quantities/parameters related to fundamental chemical forces such as (hydro-)phylicity and (hydro-)phobicity that represent an average of the properties of a patch of material or an area of the cell(s) membrane. The investigation of morphology, dynamics of individuals, and collective behavior of clusters of cells on materials is possible.

2.7 Technical Details – Boundary conditions

In a simulated environment often a significative percentage of particles is located close to the boundaries. In a three-dimensional N-particle system the fraction of the particles that is at the surface of the box is equal to $6N^{-1/3}-12N^{-2/3}$ and thus for large number of particles is proportional to $N^{-1/3}$. For a cubic crystal of 1000 atoms, almost the 49% of all atoms is located at the surface, for 10^6 atoms this fraction lowers to 6%. Therefore the behaviour of the system at the borders should not be overlooked. In macroscopic systems, only a small fraction of the atoms are located at the boundaries. In order to simulate bulk phases surface effects must be ideally suppressed. Periodic boundary conditions (PBC) enable a simulation to be performed using a small number of particles, which experience forces as if they were in a bulk medium. The simulation box is replicated in all directions to give an infinite periodic array of identical cells. (Figure 2.3 a) Each particle in the simulation box has an exact duplicate in all surrounding cells. The velocities (indicated by the arrows) are kept the same. Should a particle leave the box during the simulation than its mirror particle would appear on the opposite side with the same velocity. Interactions between the original system and its images are managed through convenient cut-offs. The longest cutoff may be no longer than half of the

shortest box vector. In that way a particle will not be able to interact with its own duplicate image (minimum image convention). In principle any cell shape that fills all of space by translation of the central box can be used. The system is often considered to be of a cubical shape, which makes it easier to implement boundary conditions. However also the hexagonal prism, the truncated octahedron, the rhombic dodecahedron or the elongated dodecahedron can be used as periodic cell. [5] The use of PBC comes with some caveat. It may lead to spurious correlations that are absent in the macroscopic system, by allowing only fluctuations that have a wavelength compatible with the periodic array of cells.

Periodic boundary conditions are not the only kind of boundary that it is possible to implement. To model the containment of particles in a vessel reflective boundary conditions can be applied. (Figure 2.3 b) In that case a particle colliding with the border of the simulation box is reflected back into the simulation volume. The collision has to conserve the total energy of the system.
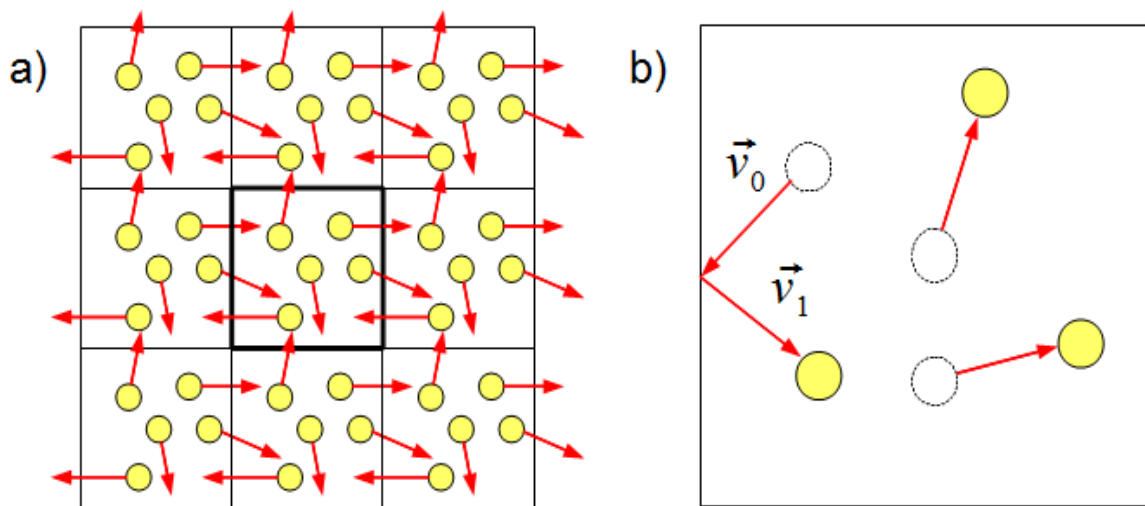
Figure 2.3 a) Schematic representation of periodic boundary conditions in two dimensions. Whenever a particle leaves the simulation cell, it is replaced by another with exactly the same velocity, entering from the opposite side. b) Schematic representation of reflective boundary conditions. $\vec{v}_0$ and $\vec{v}_1$ denote the particle's velocity vectors before and after the collision.

2.8 Technical Details – Calculating the center of mass in an environment with PBC

In general the center of mass (COM) of a set of particles in a 1D system is computed as

$$COM = \frac{\sum_{i}^{N} m_i X_i}{\sum_{i}^{N} m_i} \quad (46)$$

where m_i is the mass and X_i is the location. The center of mass is the weighted average of all points. The computation of the center of mass with periodic boundary conditions in not trivial. In a PBC system two particles can be close to one another even though they are on the opposite sides of the box. When a colloid particle, such as a graphene flake or a fullerene, straddles the boundaries a naive calculation of the center of mass will be incorrect. For this reason it is advised to resort to a different scheme. In order to compute the center of mass of a 2D system, the point masses are mapped onto 3D tubes, a provisional COM is evaluated and, in the final stage, projected back to the 2D environment. [35] The position of the particles in the 2D space are represented using the standard Cartesian coordinates, with values ranging from (i_0, j_0) to (i_{max}, j_{max}). The coordinates (x,y,z) denote the location of the point mass in the 3D space. The 2D to 3D tranformation is defined as,

$$x = r_i \cos\theta_i, \quad y = j, \quad z = r_i \sin\theta_i \quad (47) \text{ for}$$

$$r_i = \frac{i_{max}}{2\pi}, \quad \theta_i = \frac{i}{i_{max}} 2\pi \quad (48) \text{ and}$$

$$x = i, \quad y = r_j \cos\theta_j, \quad z = r_j \sin\theta_j \quad (49) \text{ for}$$

$$r_j = \frac{j_{max}}{2\pi}, \quad \theta_j = \frac{j}{j_{max}} 2\pi \quad (50)$$

After the point have been mapped onto the tubes, a provisional center of mass is calculated (x_p, y_p, z_p). These values are mapped back into new angles, θ_i and θ_j, from which the coordinate of the center of mass can be obtained,

$$\theta_i = atan2\left(-z_p, -x_p\right) + \pi, \quad i_{COM} = \frac{i_{imax}}{2\pi} \theta_i \quad (51)$$

$$\theta_j = atan2\left(-z_p, -y_p\right) + \pi, \quad j_{COM} = \frac{j_{imax}}{2\pi} \theta_i \quad (52)$$

3. Solubilization and encapsulation of fullerenes by amphiphilic molecules

Adapted from Dallavalle, M., Leonzio, M., Calvaresi, M., and F. Zerbetto "Explaining fullerene dispersion by using micellar solutions." ChemPhysChem, 15 (2014): 2998

3.1 Introduction

C_{60} is recognized as a prototypical nanomaterial. [36] Applications in lubricants, superconductors, sensors, solar cells, and, in general, in materials chemistry, [37] nanomedicine, and nanobiotechnology, have been proposed. [38] The extremely poor solubility of fullerene in water has partially hampered its exploitation. In water, the solubility of C_{60} is estimated to range from $2x10^{-24}$ to $1.1x10^{-11}$ M and the formation of fullerene aggregates (often termed nanoC_{60} or nC_{60}) has been reported .[39] The formation of difficult to characterize fullerene aggregates, with a broad size distribution (1−500 nm), is driven by van der Waals interactions.[39] The energy of interaction between C_{60} molecules is 176 kJmol-1. [40] Solvent–fullerene interactions are not strong enough to overcome the attraction between fullerene molecules, and clustering occurs both in water and in organic solvents. [39] The formation of aggregates is likely to decrease the molecular-based performance properties. The photophysics and photochemistry of C_{60} depend on the nature of the dispersion. [41] Toxicity also differs for isolated species and nC_{60} ; this makes it crucial to know if C_{60} present in the system is molecularly dispersed or in an aggregated form. [42] For example, the membrane permeability of fullerene depends on its aggregation state and functionalization of the surface. [43] Three approaches have been used to overcome the lack of solubility of fullerene: 1) mechanical dispersion–stabilization of C_{60}, [44] either through ultrasonication [45] or by solvent-exchange methods, [46] 2) synthesis of water-soluble fullerene derivatives by chemical functionalization, with hydrophilic groups, of pristine fullerene, [47] and 3) solvation of C_{60} by suitable carriers endowed with hydrophobic cores, such as γ-cyclodextrins, calixarenes, and other macrocyclic receptors, [48] molecular tweezers, [49] proteins, [50] aqueous micellar media, [51] block copolymers, [52] and liposomes. [53] Method 1 follows a mechanical-physical approach that generates metastable dispersions of fullerenes. They eventually reaggregate, because the method does not provide a way to overcome the strong fullerene-fullerene interactions. Moreover, mechanochemical treatment may often determine the surface chemical modification of C_{60}.[54] Method 2 shows some limitations, because

functionalization of C_{60} leads to alterations of its unique structure that can have a negative influence on its symmetry and electronic properties;[55] thus, restricting the potential for applications. Method 3, that is, the supramolecular approach, seems to be the most effective way to solvate pristine fullerenes, because it retains the physical properties of C_{60}. The micellar environment is almost chemically inert towards entrapped fullerene and screens it from the solvent and from aggressive reagents that may be present in solution. Moreover, micellar solutions may be considered as approximate models of biological systems. [43]

A simple but effective computational strategy [56] to describe the dispersion of fullerenes by surfactants is presented. We explore the influence of parameters such as surfactant concentration and molecular length on the final morphology of the system, to explain the experimental results and provide guidelines to understand the incorporation of C_{60} inside micelles. Both neutral and charged amphiphilic molecules are simulated. The amount of fullerene dispersion and the location of C_{60} inside micelles are examined. The computational model we selected for the investigation was dissipative particle dynamics.

3.2 Results and Discussion

Figure 3.1 shows the equilibrium morphologies of the self-assembly of charged and neutral surfactants around a single fullerene. All analyses were performed after equilibrium was reached. We take, as a representative example, one of the most used and simplest surfactants able to solvate carbon nanoparticles, namely, sodium dodecylsulfate (SDS). [57] All simulations lead to the formation of micelles, which are defined as a group of amphiphilic molecules, the tails of which are in contact with each other. The case with 15 surfactants in the simulation box, 15S, is borderline; the few surfactants adsorbed on the cage of C_{60} do not encapsulate it properly and the amphiphilic molecules form a monolayer of surfactants that protect the fullerene cage from contact with water In all other calculations, C_{60} is wrapped inside the micelle. The results underscore the ability of micellar solutions to disperse C_{60} in water. There are, however, differences in the behavior of the two kinds of surfactants. Neutral surfactants always form a single spherical micelle (Figure 3.1, top). Upon increasing the number of surfactants in the simulation box (i.e. increasing the concentration), the radius, r, of the micelle increases linearly (Figure 3.2 a). In contrast, charged surfactants prefer to self-assemble into smaller micelles, which minimize electrostatic repulsions between the charged heads. It is also possible to observe the formation of several micellar structures. By increasing

the number of surfactants, the average radius of the micelle increases as a step function, because the head-head repulsion governs the thermodynamics of self-assembly. [58] Neutral surfactants form micelles that have a larger hydrophobic space available to hold C_{60}. This behavior explains the greater propensity of neutral surfactants to solvate fullerenes in comparison to charged surfactants.
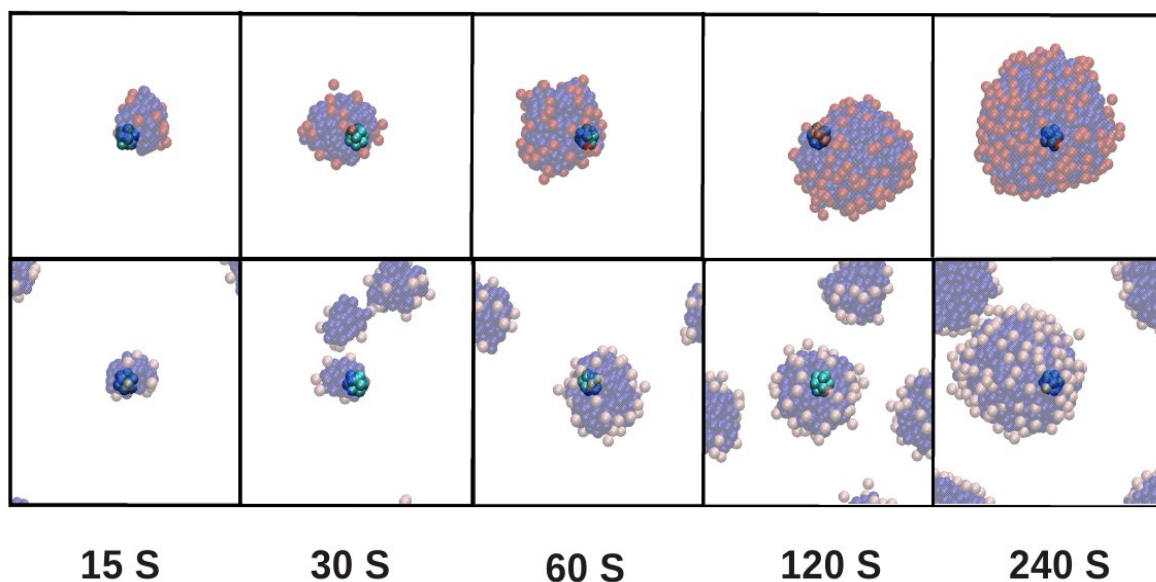

Figure 3.1 Snapshots of the equilibrium morphologies of the surfactant assemblies around C_{60}. Top: neutral surfactants (red: hydrophilic, blue: hydrophobic), fullerene (green). Bottom: charged surfactants (pink: hydrophilic, blue: hydrophobic), fullerene (green). Left to right: 15, 30, 60, 120, and 240 surfactants in the simulation box. All water molecules and counter ions are removed for clarity. The box is centered at the fullerene. Reproduced from [I].
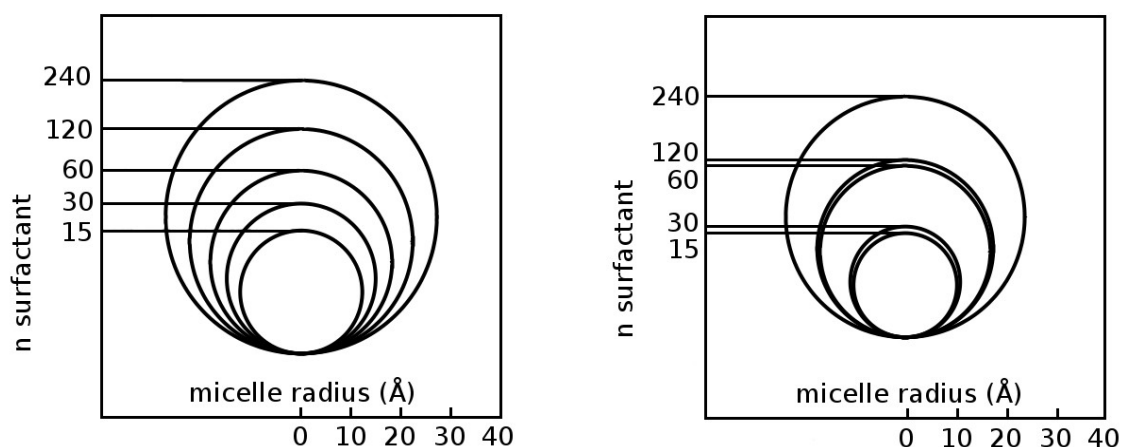
Figure 3.2 Schematic representation of the trend of the micelle radius with surfactant concentration, a) neutral and b) charged surfactants. Reproduced from [I].

Ever since the incorporation of C_{60} into micelles was observed for the first time in 1993 by Hungerbuehler et al., [53] its location in the micellar environment has been debated. The appearance of a broad band in the UV/Vis spectrum of fullerene at about $\approx$ 440 nm in the micellar solution is observed. This signal has been explained in two different ways. The first hypothesis is that the band at λ=440 nm is the same band, shifted to lower wavelengths, as the weak band at λ=540 nm observed when C_{60} is solvated in benzene, toluene, n-hexane, or 1,2-dichloroethane. A similar blueshift of this band is also observed when C_{60} is dissolved in alcohols. The solvatochromic effect observed in micellar solutions of fullerenes, may be taken as an indication that C_{60} is located close to the head groups of the surfactants. The blueshift of the fullerene band at at λ=540 nm has been explained as the result of the interaction between the polar heads of the surfactant and the π systems of C_{60}. [53] The implication is that C_{60} is not located in the inner hydrophobic part of the micelle, but in the neighborhood of the polar head groups. A second hypothesis emerged from subsequent UV/Vis and small-angle neutron scattering (SANS) studies, [51] which showed that C_{60} in micellar systems is present in molecular and colloidal states. A transition from molecular to colloidal C_{60} is induced by increasing the ratio of X=[C_{60}]/[surfactant]. At low values of X (10-4), the UV/Vis spectra are characteristic of monomeric C_{60}, as in conventional hydrocarbon solvents; no aggregates can be detected by SANS. Increasing the value of X up to 2.52×10^{-3} allows the developing broad band at $\lambda \approx$ 440 nm to be assigned to the presence of colloidal C_{60} aggregates. Similar spectroscopic behavior has been reported for C_{60} in water. An increase of fullerene concentration in water leads to aggregation and to a slight shift of the spectral bands into the long-wavelength region together with the appearance of an additional narrow spectral line at λ =450 nm. Even more accurate analysis of the spectroscopic data increased the consensus that, when dispersed by micellar solutions, fullerenes are localized in the hydrocarbon chain region, that is, in the inner part of the micelle. Further work confirmed that fullerenes were located preferentially inside the hydrophobic domain. [54,59] The results were corroborated by cyclic voltammetry, pyrene fluorescence, and micro-Raman measurements. [54,59] In the simulations, the position of C_{60} with respect to the micelle center of mass was recorded, step-by-step, during the dynamics. C_{60} molecules explore the entire core of the micelle several times by sampling the available space (Figure3.3). The region delimited by the sphere corresponds to the maximum probability of finding the hydrophilic heads of the surfactants. C_{60} is always inside the hydrophobic core of the micelle. When the volume of the available

hydrophobic region increases, C_{60} prefers to localize in the inner part of the micelle. The location of C_{60} does not depend on the charge of the surfactants. When the radius of the micelle becomes greater than 22 Å, C_{60} starts to localize in the micellar core, even if the available hydrophobic space increases. C_{60} seeks the micellar core to increase the interactions with the surrounding surfactants tails.

Figure 3.4 shows the number of surfactant tail beads that interact with C_{60} as a function of the micelle radius. The number of enthalpic interactions of C_{60} increases with increasing radius. In summary, C_{60} is in the hydrophobic inner region, which is in agreement with the interpretation of the experimental data. [54,59] The tendency of C_{60} to localize in the inner part of the micelle may be one of the reasons that explains why C_{60} also tends to form colloid aggregates inside micelles.[53]
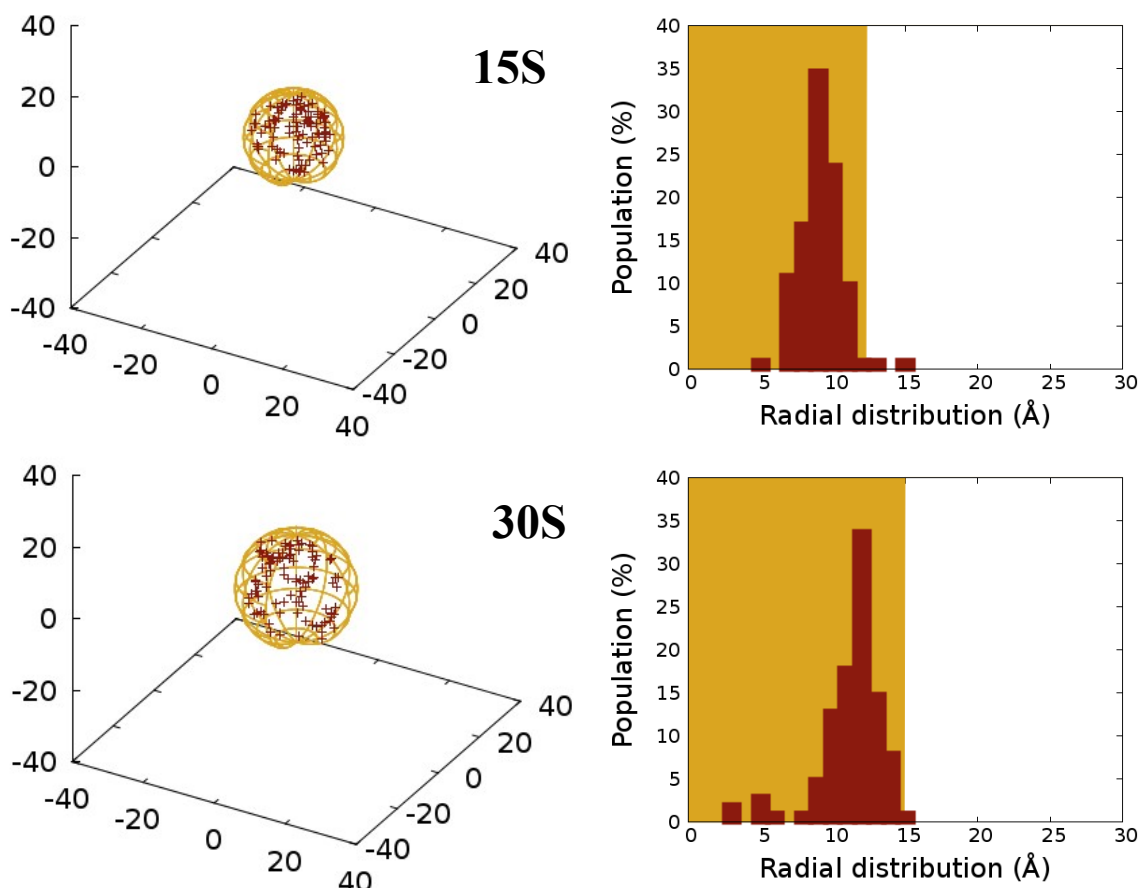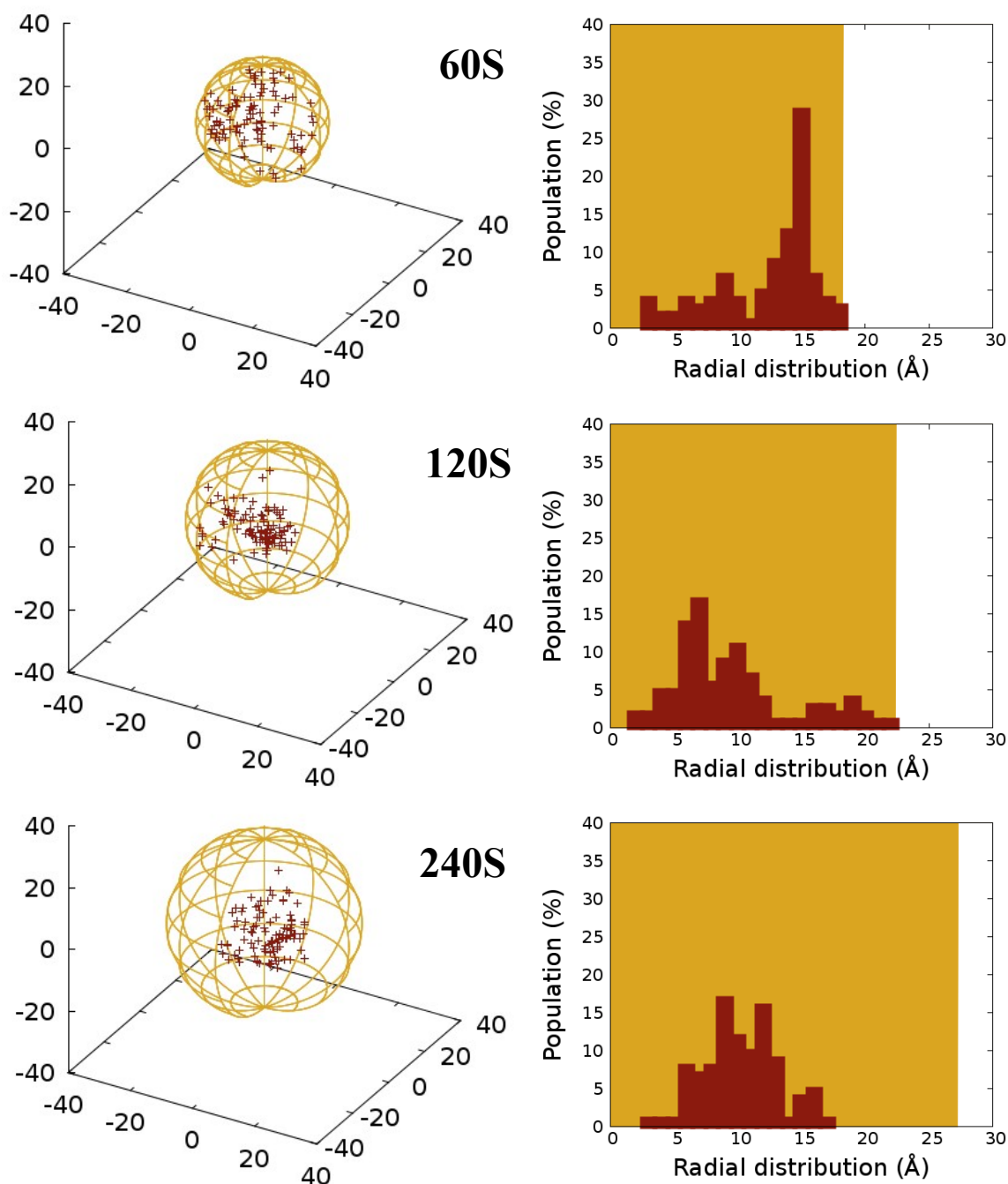
Figure 3.3 Fullerene distribution inside the micelle at different surfactant concentrations. The region inside the sphere corresponds to the maximum probability of finding the hydrophilic heads. The center of mass of C_{60}, recorded at different times, is represented by red spots. As the micelle dimension increases, the fullerene moves deeper into the micellar core. The charged surfactants show similar behavior that is dependent only on the micelle dimension. Back-to-back, we propose an alternative presentation of the data. The fullerene radial distribution with respect to the center of the micelle is displayed. The yellow area represents

the micellar environment. As the radius of the micelle increases the fullerene drift towards the micellar core. Reproduced from [I].
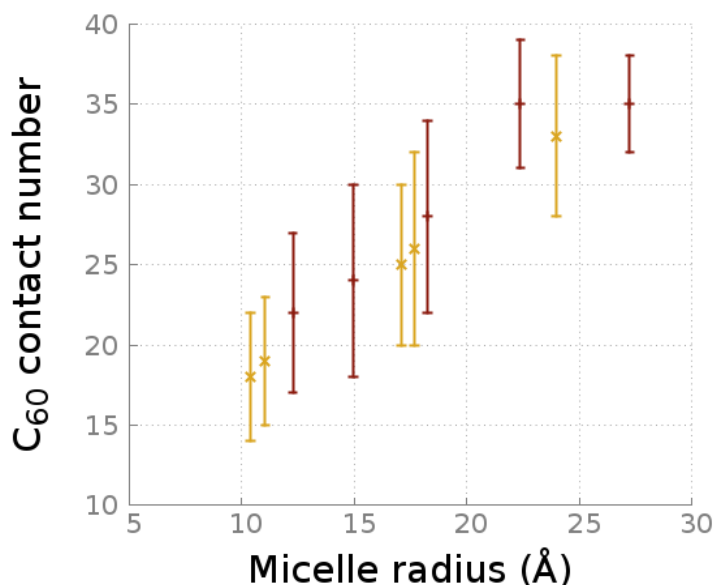
Figure 3.4 Number of contacts between C_{60} and the surfactant tail beads. Thebars represent standard deviations. Red: neutral surfactants; yellow: charged surfactants. Reproduced from [I].

We investigated the effect of the ratio of the number of surfactants and C_{60} molecules. The number of surfactant molecules was kept constant (240 surfactants in the simulation box), whereas the number of C_{60} molecules was gradually increased. In all cases, the results in Figure 3.5 show that increasing the number of C_{60} molecules leads to aggregation of the fullerenes.

The C_{60} aggregates are spherical, as experimentally determined for small nC_{60} nanoparticles. [60] Upon increasing the C_{60} concentration, the system morphology changes from a micelle entrapped C_{60} to a colloidal aggregate of C_{60} covered by a surfactant monolayer. Morphological transitions of amphiphilic molecules, induced by nanoparticles clustering at various nanoparticle volume fractions, have been observed experimentally by Park and co-workers. [61] The polymer depletion mechanism (owing to increasing surfactant-tail entropy) and the enthalpic van der Waals attraction potential between fullerenes led to clustering of nanoparticles [61] in the core of the micelle. Although both C_{60} and the alkyl chains of the surfactants are hydrophobic, they are geometrically and chemically different. Fullerenes

prefer to interact with other fullerenes and segregate in the micelle core.

The diffusion behavior of C_{60} and surfactants can be used to monitor the effect of increasing concentration (Figure 3.6). With up to 32 fullerenes in the unit box, we observe fullerenes entrapped inside the micelle. The diffusion coefficient of fullerenes is lower than that of the micelle. with more than 64 fullerenes, the system moves as a single body. Surfactants and fullerenes have the same diffusion coefficient. The system is a colloidal nanoparticle of C_{60} with surfactants adsorbed on the surface. The diffusion of the center of mass of the aggregates shows a small variation with concentration. The movement of the aggregate is insensitive to its size. An increase in the concentration of C_{60} results in an increase of diffusion of the system.

Rheological measurements revealed that, micellar systems tended to be more fluid after fullerenes were incorporated into the hydrophobic domains.[62] Enhanced mobility of fullerene nanoparticles has also been observed in the presence of stabilizing agents.[63] Dynamic light scattering experiments showed that an increase in C_{60} concentration resulted in an increase in the value of the diffusion coefficient for fullerene aggregates, [64] in accordance with the present simulations.
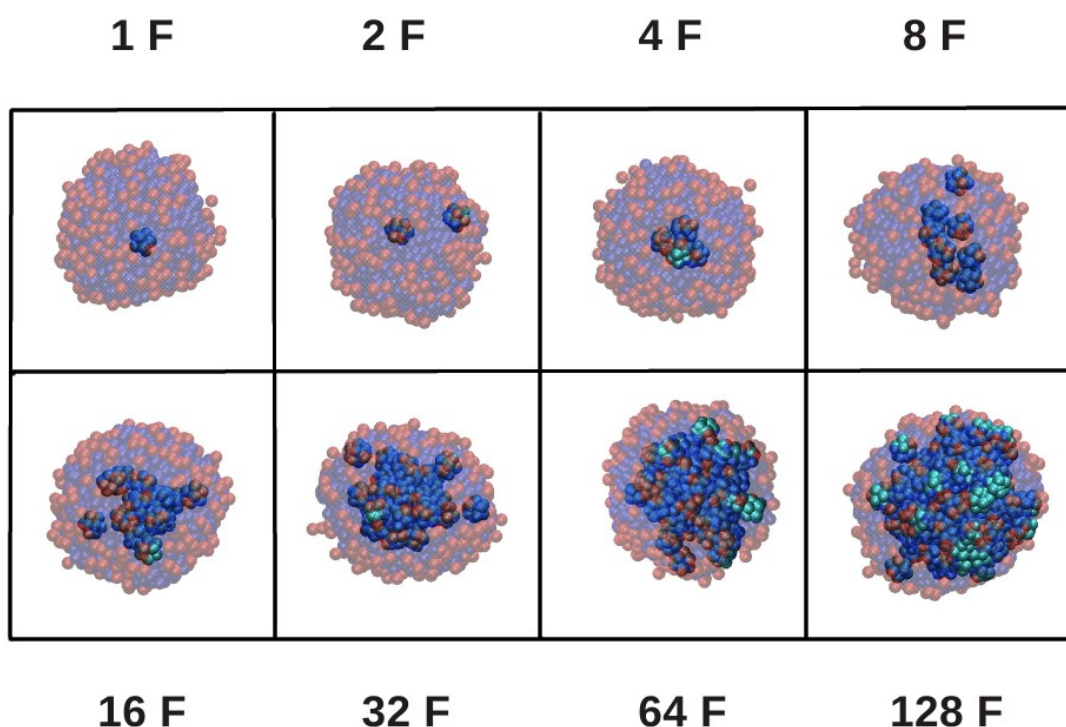
Figure 3.5 Representative snapshots of the simulation box for increasing fullerene concentrations. The 240 nonionic surfactants always form a single micelle. The fullerenes are

encapsulated in the micelle hydrophobic core and undergo aggregation. Reproduced from [I].
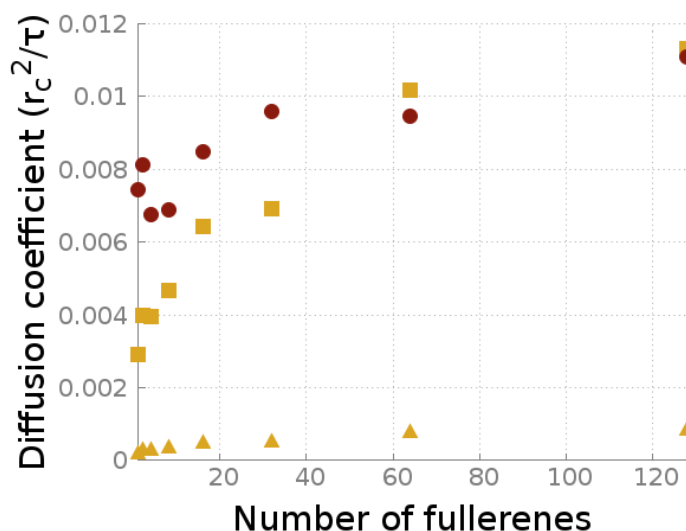

Figure 3.6 Diffusion coefficient (in DPD dimensionless units) of fullerene (yellow square), fullerene aggregates (yellow triangle), and surfactants (red circle) versus fullerene concentration. Reproduced from [I].

Figure 3.7 illustrates how surfactant concentration, chain length, and charge affect the encapsulation of multiple fullerenes in the micellar solutions. Micellization occurs in all simulations. The only exception is for the lowest concentrations of short amphiphilic molecules in which the surfactants simply adsorb on the cages, which screens them from water. Experimentally, when concentrations are below the critical micelle concentration (cmc), the presence of surfactants can still improve the dispersion of C_{60}.[65] Figure 3.7, top, shows that neutral surfactants preferentially form a single spherical micelle encapsulating the fullerenes. The formation of nC_{60} aggregates is observed in the majority of the calculations. Fullerenes self-aggregate inside the micelle and it is extremely difficult to obtain fullerenes dispersed monomolecularly. [51]

Figure 3.7, bottom, depicts the effect of charged surfactants on C_{60} dispersion. Charged stabilizers tend to form multiple micelles, because of the presence of electrostatic repulsion between the charged heads. In the case of longer surfactants, 7T and 9T, the presence of multiple micelles improves the dispersion of C_{60}, although the formation of fullerene aggregates is still observed. Shorter surfactants, 5T and 3T, are more effective in suppressing aggregate formation. For example, 3T, with 120 or 240 surfactants in the box, disperses C_{60}

molecularly. The formation of multiple small micelles hinders aggregate formation. If C_{60} fits the hydrophobic cavity of the micelle and there is no room for another guest, then it is possible to obtain monomeric fullerene dispersion. This encapsulation is similar to that observed in macrocyclic receptors, which are able to disperse pristine C_{60} in water in monomolecular form [48] or in capsule/clamshell structures with a designed nanoscale cavity for the recognition of fullerenes. [66] This principle can be used for the construction of highly ordered fullerene assemblies characterized by a well-defined tridimensional topology or fullerene sorting. [67]

The calculations are consistent with experimental observations. [54] It has been reported that nonionic surfactants disperse a higher amount of C_{60} in comparison to ionic surfactants, [54] because of the higher hydrophobic volume available. Nevertheless, the formation of aggregates is observed, because the absorption spectrum displays the characteristic absorption of nC_{60}. [54] The 1T amphiphilic molecules are unique in their solvating power, among the stabilizing agents, because they avoid the formation of aggregates inside the micelle. It is known that pyridine and other nitrogen-containing solvents with aromatic rings are able to reduce the extent of aggregation. [39,67] In calculations with 1^T amphiphilic molecules, little or no aggregation of C_{60} is observed. Experimentally, fullerenes, when dissolved in binary solvent mixtures of water/pyridine, exhibit strong solvatochromism and an unusual chemical inertness. [68] This behavior has been associated with the formation of chemically inert, water-soluble C_{60}/pyridine nanocapsules, in which pyridine appears to act as a surfactant around the fullerene molecules to protect them from chemical reagents; [68] this is actually observed in the present simulations. The driving force for self-assembly is provided by hydrophobic interactions between C_{60} and water. [68] As surfactant behavior in aqueous solutions depends on temperature and/or ionic strength, it is, in principle, possible to control the aggregation of nanoparticles by changing these easily tunable parameters.
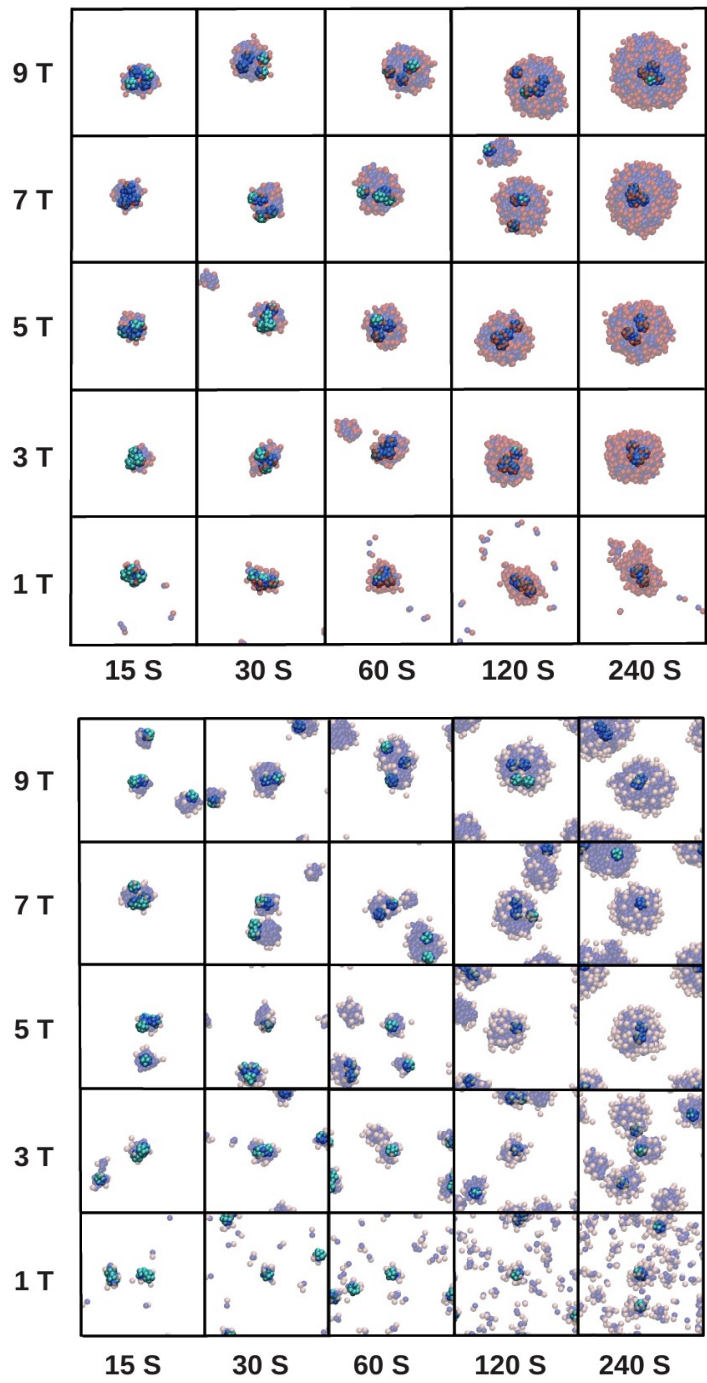
Figure 3.7. Snapshots of equilibrium morphologies of surfactant assemblies around C$_{60}$. Left to right 15, 30, 60, 120, and 240 surfactants in the simulation box. Top: neutral surfactants. Bottom: charged surfactants. Length of the surfactant in shorthand notation 1T, 3T, 5T, 7T, 9T. Red: hydrophilic neutral beads, blue: hydrophobic neutral beads, sea green: fullerene beads, pink: hydrophilic charged beads. Water molecules and counter ions removed for clarity. Reproduced from [I].

3.3 Computational details

All calculations were performed by using the Culgi 4.0.1 suite of programs.[69] The system consisted of water, surfactants, and one or more fullerenes. Surfactants were described by single chains of soft spheres. In the simulations, the bead density was set at $\rho=3$ in DPD units. A cubic simulation box of dimension 20x20x20 r_c was used and periodic boundary conditions were applied. The total number of beads was 24000. The calculation was run for 100000 steps by using a time step of 0.05 τ.

To transform the dimensionless or DPD units used in the simulations into physical lengths and timescales, it was necessary to link simulations and experimental data. The model system used for the conversions had a tail of nine beads: it represented a SDS molecule. The bead interaction range, r_c, was the unit of length of the system and was defined as the side of a cube containing an average number of ρ beads, according to Groot and Warren.[11] The volume of the $C_{12}H_{15}$ tail was 350 $Å^3$; [70] hence, each bead was about 39 $Å^3$. Because the bead density was 3, a cube of r_c^3 contained 3 beads and therefore, corresponded to a volume of 117 $Å^3$. The physical size of the interaction radius r_c was equl to 4.9 Å. As proposed by Groot and Rabone, [71] to obtain the physical timescale we compared the calculated diffusion coefficient of water beads with the experimentally measured values ($D_{exp}=2.43x10^{-5}$ cm^2s^{-1}). [40] The resulting unit time was 35.4 ps. This meant that the 20x20x20 r_c box represented a cube of linear dimension of 9.8 nm and that the fullerene had a radius of 4.9 Å. The typical simulation run of 100000 steps, with a time step of 0.05, corresponded to a total time of 0.18s.

3.4 Conclusion

DPD simulations provided a theoretical framework that described the encapsulation of fullerene in micellar solutions. The long-discussed problem of the location of fullerene in micelles was addressed and fullerenes were found to locate themselves in the hydrocarbon-chain region of micelles. When the available hydrophobic space increased, C_{60} localized in the inner part of the micellar core for enthalpic reasons.

A systematic study of the effect of the stabilizer chain length, charge, and concentration on fullerene aggregation was presented. Nonionic surfactants formed larger micelles than charged surfactants. The greater hydrophobic volume available in neutral surfactants micelles explained their greater efficiency in solvating C_{60}. Short, charged amphiphilic stabilizers were more efficient at dispersing fullerenes monomolecularly. The mechanism of the dispersion of

fullerenes was concentration dependent; aggregation of C_{60} molecules was observed inside the micelles as the concentration increased. Two different phases appeared upon varying the C_{60}/surfactant ratio. In the first, aggregates of fullerenes were entrapped inside the micelles; in the second, colloidal nanoC_{60} was formed with surfactants adsorbed on the surface. Only small micelles with the appropriate hydrophobic cavity entrapped a single C_{60} particle and led to monomolecular dispersion of fullerenes, without aggregate formation. By tuning the chain length and the charge of the amphiphilic molecules, it was possible to achieve quasi-monomeric fullerene dispersion. Among the stabilizers considered, small amphiphilic molecules, as in the well-known case of nitrogen-containing co-solvents, displayed a unique solvating power.

4. Graphene nanosheets at the membrane interface

Adapted from Dallavalle, M., Calvaresi, M., Bottoni, A., Melle-Franco, M., and F. Zerbetto "Graphene can wreak havoc with cell membranes" *ACS Applied Materials & Interfaces,* 7 (2015): 4406

4.1 Introduction

With the development of various forms of nanotechnology, there is a need to understand their hazardous effects. Graphene and its derivatives, in particular, have potential for a wide variety of biomedical applications. [72] Possible short- and longterm adverse health impacts must be considered in the design of graphenes for drug delivery, tissue engineering, and sensing devices. [73−76] The relatively limited data available suggest that graphene materials can be either benign [77−79] or toxic to cells. [80−100] A recently proposed set of rules for the use of graphenes entailed the following: [101] (1) use of small, individual graphene sheets that macrophages in the body can efficiently internalize and remove from the site of deposition; (2) use of hydrophilic, stable, colloidal dispersions of graphene sheets to minimize aggregation in vivo; (3) use of excretable graphene material or chemically modified graphene that can be degraded effectively. It has been suggested that the biological response depends on the number of layers, lateral size, stiffness, hydrophobicity, surface functionalization, and, perhaps obviously, dose. [74,81−102] The hydrophobic surface area of graphene may produce significant interactions with membrane phospholipids either causing direct physical toxicity or causing indirect toxicity. [80−106] Despite the common carbon composition, graphene differs

remarkably from another allotrope of carbon, namely carbon nanotubes. Graphene sheets have a lower aspect ratio, larger surface area, and better dispersibility in most solvents than nanotubes. Importantly, graphenes are not fiber-shaped. Most of these features of graphene appear advantageous in terms of safety over inhomogeneous dispersions of fiber-shaped carbon nanotubes.[101] The issue arises of how and why cellular uptake of graphene nanosheets depends on size, shape, elasticity, and surface structure.

Simulations can provide important information on the interaction between graphene sheets and lipid membranes. [91,92,103−106] Molecular dynamics simulations showed that the graphene sheets can be hosted in the hydrophobic interior of biological membranes formed by

amphiphilic phospholipid molecules. [103] MD and coarse grain simulations revealed the uptake process of graphene in cellular membranes. The entry was initiated at corners or asperities that were abundant along the irregular edges of graphene materials. Local piercing by these sharp protrusions initiated propagation along the extended graphene edge to achieve full penetration. [91] Dissipative particle dynamics simulations showed the role of size and edges in the translocation of graphene nanosheets across a lipid bilayer membrane. The permeation of small sheets was driven by trans-bilayer lateral pressure. For larger nanosheets, the translocation underwent a vesiculation process. Circular sheets with smooth edges showed faster translocation than square ones. [104] Another study demonstrated the effects of graphene thicknesses (single/multilayered graphene), oxidation, and lipid coating on the graphene entry. Pristine and fewlayered graphene nanosheets could spontaneously insert into the bilayer and reach the center of the bilayer. [105] Alternatively, edge oxidized graphene nanosheets could pierce the bilayer to reach a final state that was located at the center of the bilayer or stood upward across the bilayer, depending on the degree of oxidation. [105]

In this chapter, we focus on the unexplored effects of a graphene sheet of increasing size on the structure of the phospholipid double layer. Small hydrophobic graphene sheets easily pierce through the phospholipid membrane; intermediate size sheets pierce the membrane only if a suitable geometric orientation is met, while larger sheets adsorb on the top of the bilayer where they modify the membrane and create a patch of upturned phospholipids. Both a static description and a dynamic description of the system are provided. The final equilibrium configuration in the bilayer is expressed in terms of normalized free energy and by means of the phospholipid order parameter. The perturbation caused by the presence of the graphene sheet is quantified in terms of phospholipid translocation (flip-flop).

4.2 Results and Discussion

DPD calculations were carried out using a system composed of water, phospholipids, and graphene nanosheets, GS, of different sizes. DPD runs were repeated five times to acquire sufficient statistics. A self-assembled and equilibrated bilayer was present in the simulation box with every GS positioned randomly at five different starting positions. Figure 4.1 provides snapshots of the GS/phospholipid bilayer interaction at the end of the simulations. The particle size of the GS determined its final configuration in the bilayer. The five smaller sheets pierced through the membrane. The four larger sheets adhered to the membrane, a deed

that is not done by the two smaller sheets. Sheets smaller than 5.2 nm were also able to navigate the membrane (vide infra). Increasing their size and up to 11.2 nm, they crossed the bilayer only if a suitable geometric orientation was met and, correspondingly, two minima were found in the free energy surface (Figure 4.2). In the first minimum, the GS pierced through; in the second one it adsorbed on the membrane. If larger than 11.2 nm, the sheets were unable to cross the membrane. Assumptions are necessary when comparing experimental and MD results. The small size GS used in most experiments are larger than or similar to the largest sheets of the current MD study. We present an idealized system with a single graphene sheet where the formation of aggregates is neglected. Experiments are usually carried out with suspension of graphene derivatives. However, these results are in line with the size dependency on the GS cellular internalization process. [88,89,99,100,102,106] The preferred orientation of the GS was also size dependent. In Figure 4.3 the x-axis shows the angle of the sheet with the phospholipid bilayer. A value of the angle close to 0° means that the sheet was parallel to the membrane; a value close to 90° means that it was perpendicular to it. The smaller the sheet, the more freely it diffused inside the membrane. Small sheets preferentially align with the phospholipid hydrophobic tails and maintained a perpendicular orientation. Sheets greater than the membrane thickness moved to smaller angles, arranging themselves across the membrane to be embedded as much as possible in the hydrophobic part of the bilayer. Even larger sheets only adhered to the external surface of the membrane.
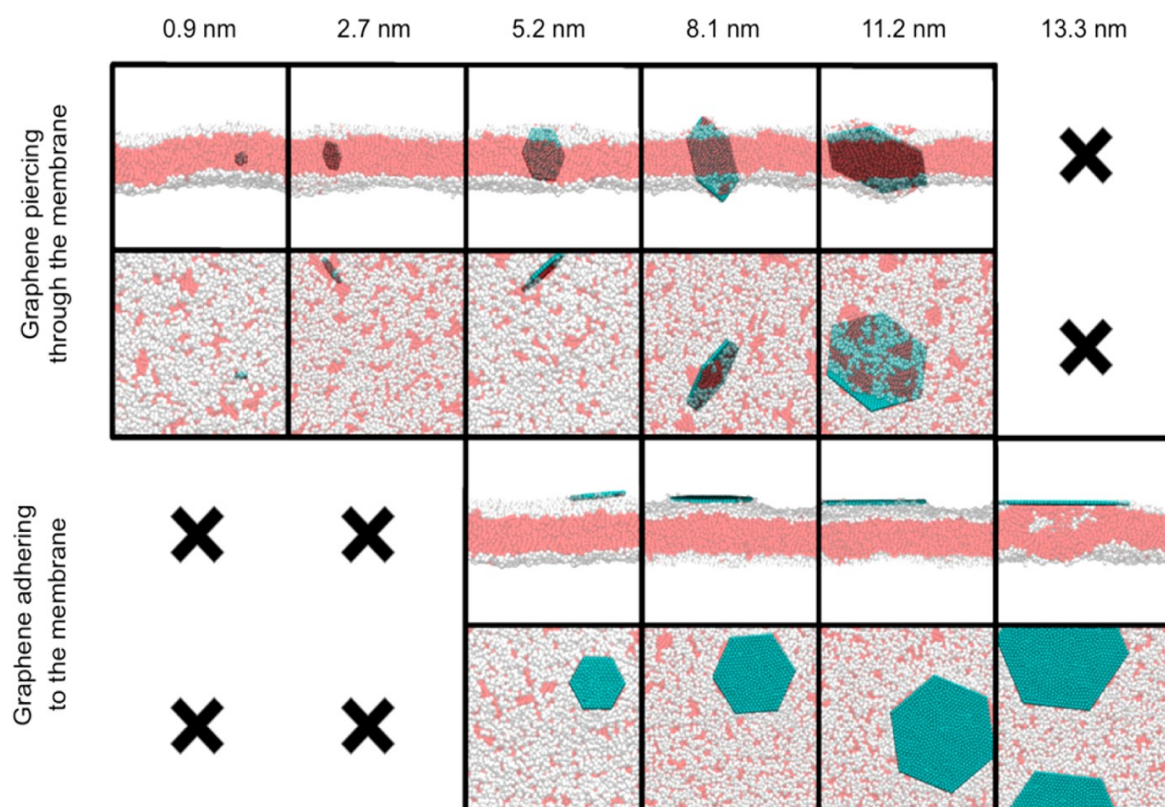
Figure 4.1 Illustrative snapshots, at the end of the simulations, of six graphene nanosheets of increasing size. From left to right, sizes of 0.9, 2.7, 5.2, 8.1, 11.2, and 13.3 nm. White: hydrophilic heads of the phospholipids; red: hydrophobic phospholipid tails; petroleum blue: graphenes. For clarity, water is not shown. The top two rows are different perspectives of the six sheets, as are the bottom two rows. Only the five smaller sheets pierce through the membrane. The four larger sheets adhere to the membrane. Situations not observed in the simulations are indicated by "×". Reproduced from [II].
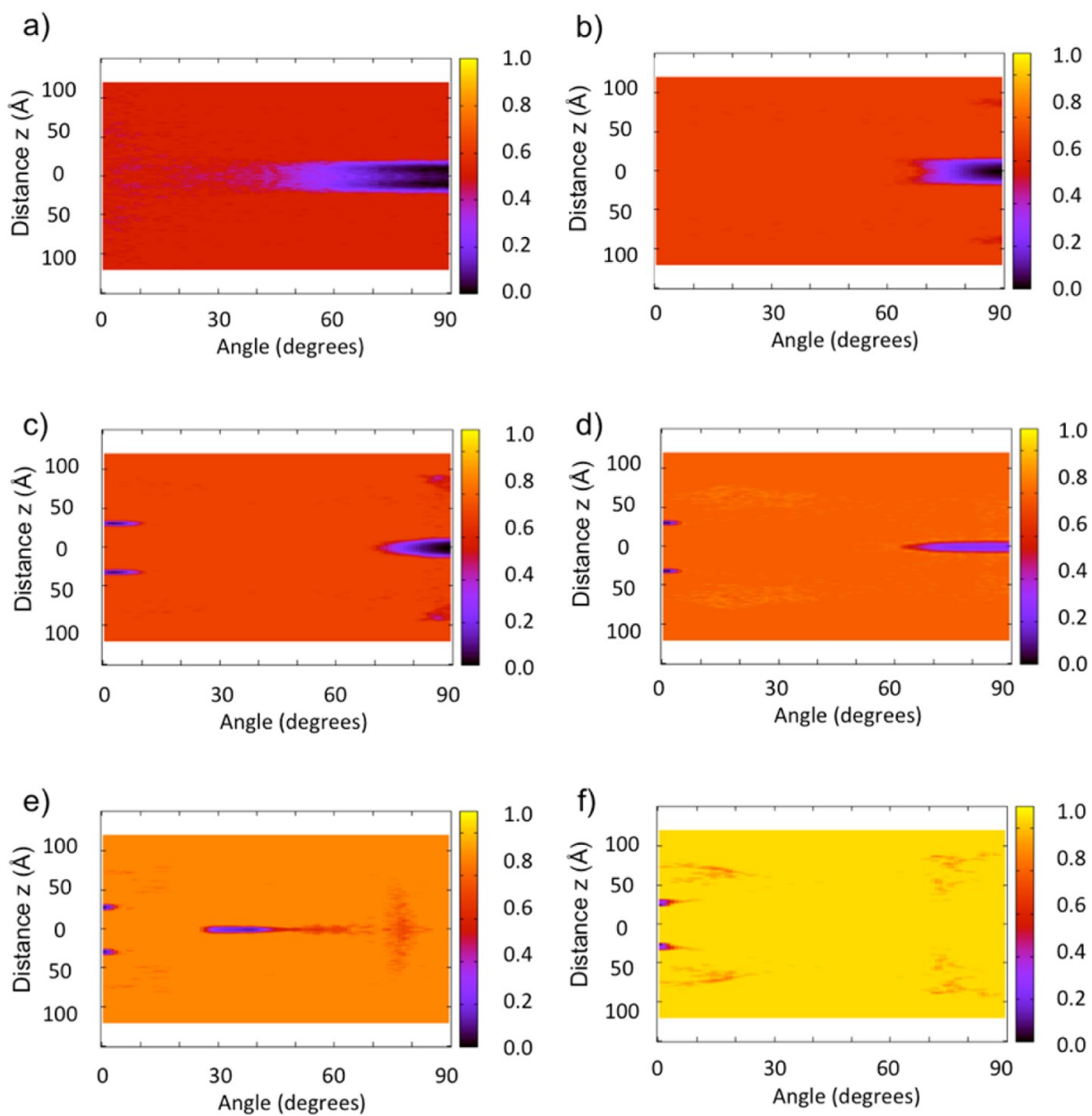
Figure 4.2 Normalized free energy of the systems as a function of the graphene penetration and orientation. Sheet sizes: (a) 0.9, (b) 2.7, (c) 5.2, (d) 8.1, (e) 11.2, and (f) 13.3 nm. Reproduced from [II].
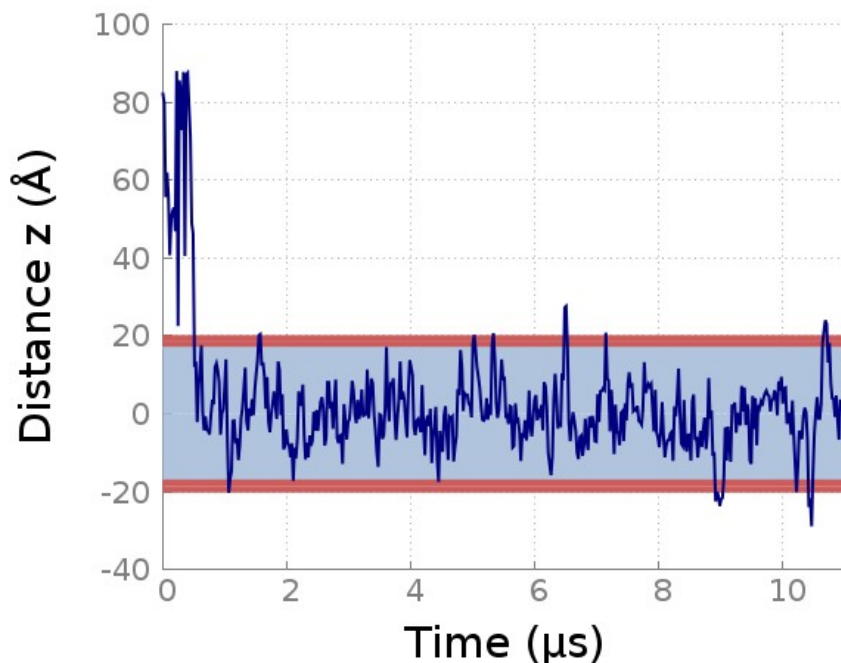
Figure 4.3 Evolution in time of the position of the center of mass of a graphene sheet (0.9 nm) with respect to the membrane.The smaller the GS, the more freely it diffuses inside the membrane.

The presence of the sheet affected the overall density distribution of the hydrophobic and hydrophilic moieties of the phospholipids. Figure 4.4 compares the densities for the unperturbed membrane (Figure 4.4 a) and for the perturbed bilayer when the graphene flake (size 11.2 nm) pierced through (Figure 4.4 b) or adhered to (Figure 4.4 c) the membrane. When graphene penetrated the membrane (Figure 4.4 b), some phospholipids stuck to the graphene and followed GS movements. The head beads were no longer excluded from the bilayer interior, and the two monolayers were no longer properly interdigitated. When GS adsorbed on the membrane, an asymmetry was induced in the membrane bilayer (Figure 4.4 c) because the hydrophobic tail beads tended to move toward the interface with the GS nanoparticle.
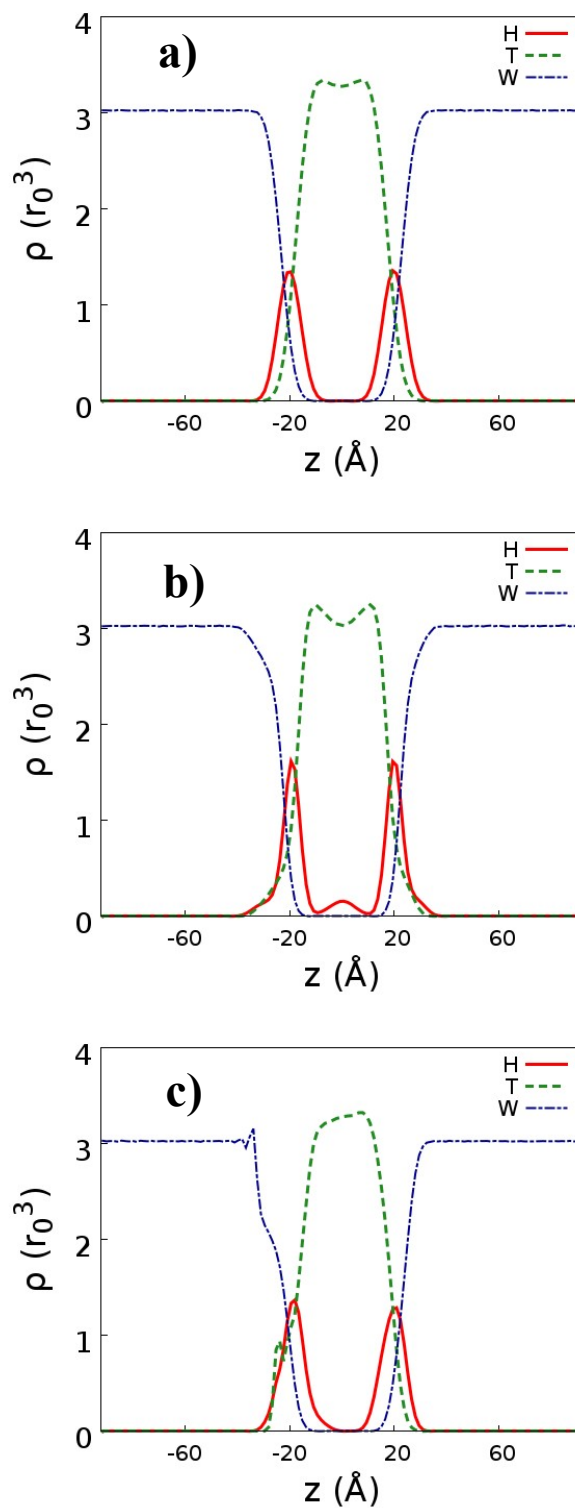
Figure 4.4 Density profiles of the phospholipid bilayers. Hydrophilic head beads, H; hydrophobic tail beads, T; bulk water, W. a) Unperturbed membrane; b) bilayer pierced by the graphene sheets; c) adhesion of the graphene to the membrane. The profiles were averaged over 1000 steps. Reproduced from [II].

The order parameter, $S = \langle (3/2) \cos^2 \theta - (1/2) \rangle$, allows a more quantitative evaluation of the orientational order (or disorder) induced by the sheets in the phospholipids of the membrane. The angle, θ, is formed by an axis perpendicular to the membrane and the long axis of each molecule. An unperturbed membrane is characterized by $S = 0.73$. Table 4.1 compares the global (all the phospholipids were considered) and the local (only the phospholipids within the range of 1.5 r_c, roughly 8.6 Å, from the GS were considered) order parameters of the phospholipids, averaged over 100 steps of the equilibrated systems. Small GS piercing the membrane did not perturb, both globally and locally, the order of the membrane and could easily enter the cell. The higher cellular uptake for ultrasmall GS can be explored to make them ideal nanocarriers for drug delivery systems. Increasing the size of the GS (> 5.2 nm), strong local perturbations of the membrane were observed. The global order of the membrane was more or less maintained for piercing GS. On the contrary, an adhering sheet induced a substantial disorder. Larger sheets induced local antialignment (S is negative for antialignment). We propose an alternative presentation of the data in Figure 4.5. The question arises of whether the antialignment is related to the presence, in itself puzzling, of a hydrophobic GS that adheres to the top of a membrane, which is hydrophilic. Peeling off the nanosheet revealed that the phospholipids of the layer directly under the sheet capsized and interacted with the sheet with the hydrophobic tail (Figure 4.6). The antialignment was therefore truly related to the hydrophobic−hydrophobic interaction that allowed the sheet to adhere to the membrane. Importantly, the overturned phospholipids could impair cell functioning and disrupt the functioning of the membrane proteins. They may explain the cytotoxic activity of adhering GS, the so-called masking effect. [89,90,99] Experimental availability of the basal planes of graphene determines whether it is cytotoxic. [98] Notice that size-dependent GS toxicity and changes in the toxicity mechanisms are well-known experimentally [88−91,99,100] and computationally. [91,104,106]

Table 4.1 Global vs local (dis-)order induced by graphene sheets piercing through or adhering to the membrane.

Nanosheet size	GS piercing through		GS adhering	
	S_{local}	S_{global}	S_{local}	S_{global}
0.9 nm	0.72	0.69	-	-
2.7 nm	0.72	0.69	-	-
5.2 nm	0.77	0.68	0.03	0.66
8.1 nm	0.34	0.65	-0.16	0.59
11.2 nm	0.10	0.57	-0.16	0.52
13.3 nm	-	-	-0.13	0.45

Nanosheet size	GS piercing through	GS adhering
0.9 nm		
2.7 nm		
5.2 nm		

8.1 nm	$S_l = 0.34$ $S_g = 0.65$	$S_l = -0.16$ $S_g = 0.59$
11.2 nm	$S_l = 0.10$ $S_g = 0.57$	$S_l = -0.16$ $S_g = 0.52$
13.3 nm		$S_l = -0.13$ $S_g = 0.45$
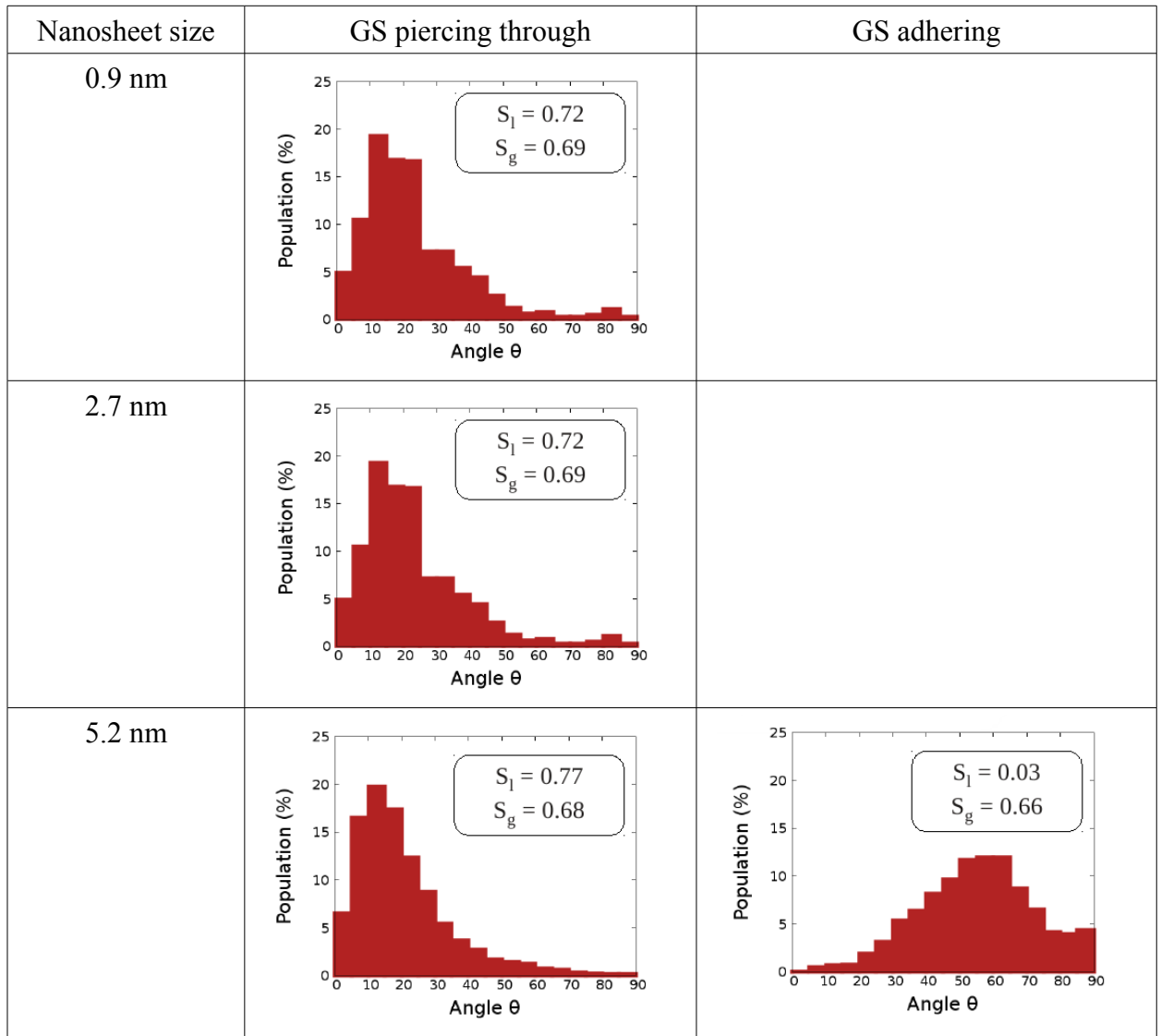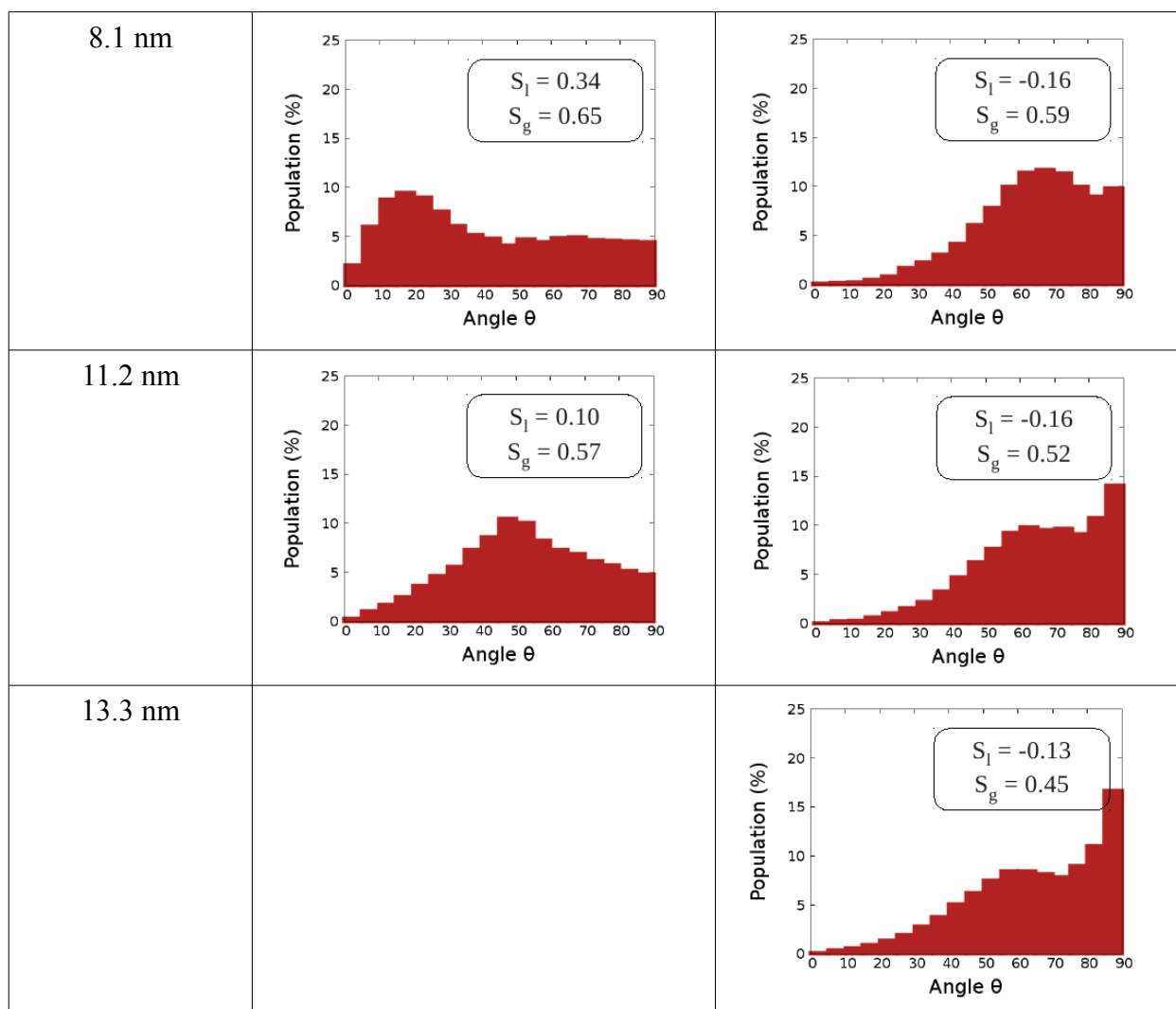
Figure 4.5 Phospholipids angle distribution
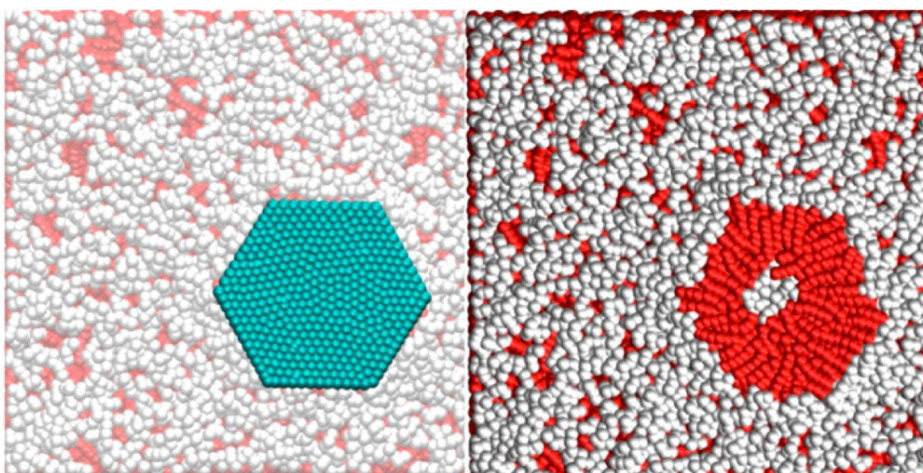
Figure 4.6 (left) Sheet adhering to the phospholipid membrane. (right) Peeling off the sheet shows that the hydrophobic tails directly interact with hydrophobic graphene. Reproduced from [II].

The adsorption of the graphene flake triggered the translocation from one layer to the other of multiple phospholipids (Table 4.2). Liu et al. [107] demonstrated that the migration of lipids in living cells could be facile under physiological conditions, also in the absence of a protein mediated process, on the second time scale. In the presence of GS, the majority of translocation events occurred as soon as the graphene sheet settled on the top of the layer (Figure 4.7), in less than 1 μs. During the rest of the dynamics the number of flipflops remained constant, within statistical fluctuations. The spontaneous translocation of a phospholipid in the membrane usually involves three steps (Figure 4.8 a). In the first the phospholipid desorbs from a layer, in the second it reorients itself, and in the third it accommodates itself in the opposite layer. The largest GS is taken as a representative case. Only in 34.8% of the cases (80 out of $46 \cdot 5 = 230$), the phospholipid reoriented in the starting layer and subsequently diffused to the opposite layer (Figure 4.8 b). This mechanism was mostly observed when the translocating phospholipid was located at the interface with graphene. In 65.2% of the cases (150 out of 230), a new mechanism was observed. The phospholipid did not somersault and reached the opposite layer without reorienting. In more detail, the translocations observed during the dynamics belonged to three types. The first type was the detachment of a phospholipid from the layer further from the graphene sheet. The phospholipid subsequently accommodated itself in the other layer at the interface with the GS. The path started from the unperturbed region and reached the perturbed area. The second type followed the opposite path. There was a detachment of a phospholipid from the layer perturbed by the graphene sheet with its subsequent accommodation in the opposite layer. The third type of translocation was the reversible accommodation of a phospholipid at the graphene interface. The phospholipid desorbed from the unperturbed layer, traveled to the opposite one, and then drifted back to the initial membrane. The percentage of events of the first type was 74.3% (171 out of 230), of the second type was 11.3% (26 out of 230), and of the third type was 14.3% (33 out of 230). The global motion of the phospholipids, induced by the GS, generated an asymmetric density distribution (Figure 4.4 c). The layer closer to the graphene sheet was enriched by the translocations, while the layer further away was impoverished. Biologically, translocation of phospholipids to the external side of the membrane triggers a number of membrane associated events, including recognition and elimination of apoptotic or aged cells. [108] Apoptosis in macrophages can be triggered by pristine graphene. [109] The translocation mechanism discussed here can also modify the

polarization of the cellular membrane and induce cytotoxicity.
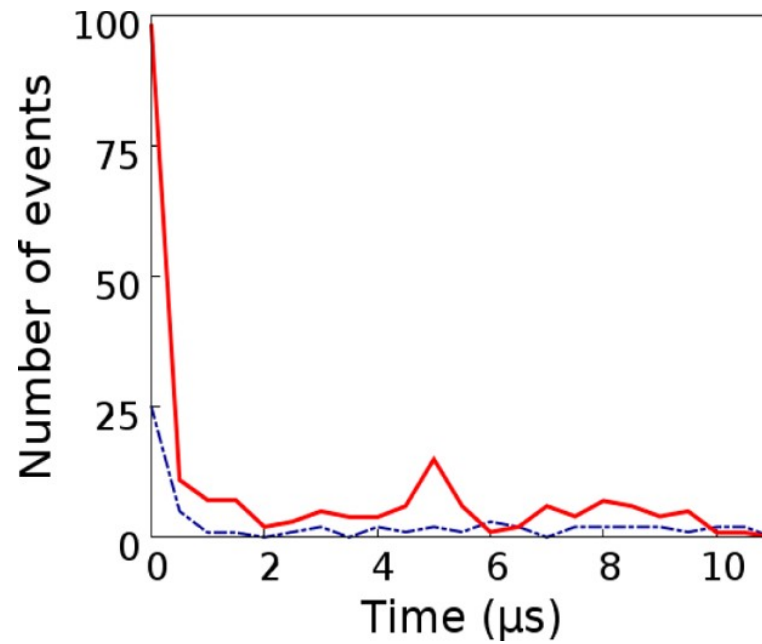

Figure 4.7 Phospholipid translocation for the largest GS. Solid red line, the phospholipid drifts from the unperturbed leaflet to the grapheneinterface; dashed dotted blue line, the phospholipid wanders from the perturbed leaflet to the opposite layer. Reproduced from [II].
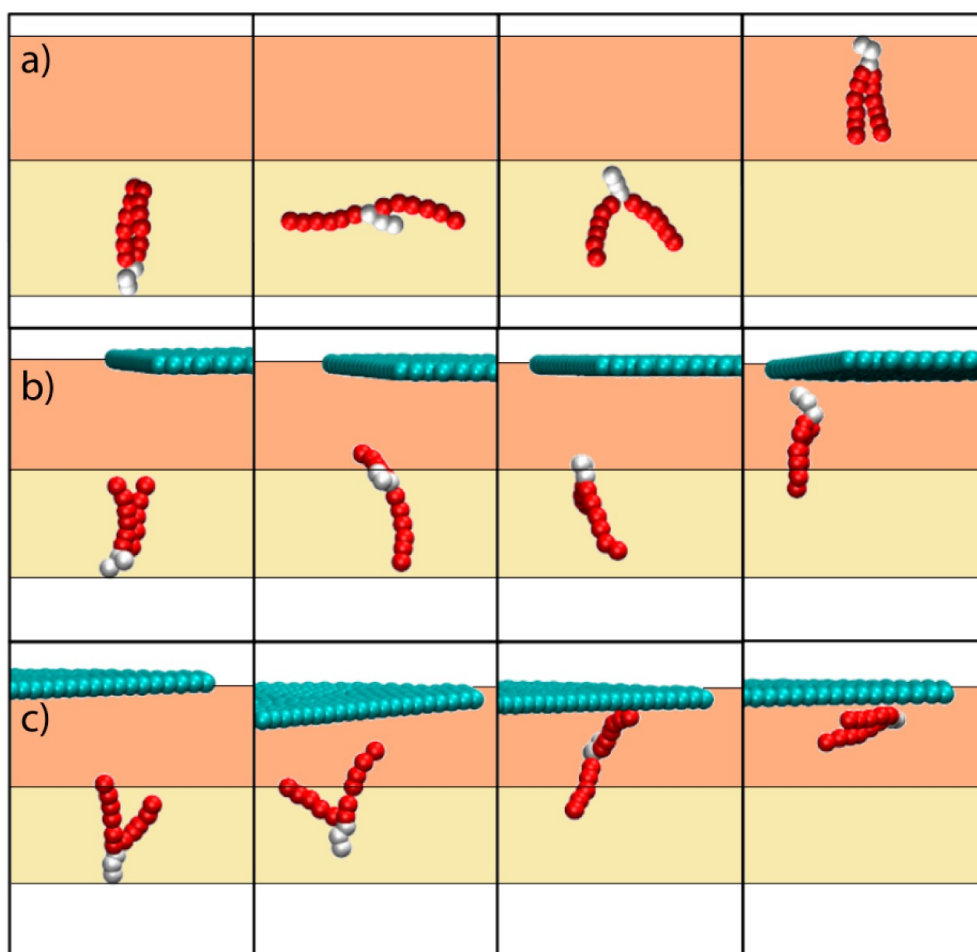
Figure 4.8 Spontaneous translocation of a phospholipid in the membrane. For sake of clarity, only the flip-flopping phospholipid and the graphene flake are shown. The two layers of the membrane are represented as continuous fields. (a) Spontaneous translocation of a phospholipid in a membrane; (b) translocation with reorientation in the presence of a GS; (c) translocation without reorientation in the presence of a GS. Reproduced from [II].

Table 4.2 Average number, over five dynamics, of flip-flops during 11 µs of dynamics.

Nanosheet size	n of translocation events
0.9 nm	3
2.7 nm	4
5.2 nm	8
8.1 nm	17
11.2 nm	41
13.3 nm	46

4.3 Computational details

In the simulations, the bead density was set at $\rho = 3$. A cubic simulation box of dimension $32r_c \times 32r_c \times 32r_c$ was used and periodic boundary conditions were applied. The total number of beads was 98 304. Each of the calculations was run for 2 500 000 steps using a time step of 0.05τ. For transformation of dimensionless DPD units into physical length and time scales, it is necessary to link simulations with experimental data. The center-to-center distance between polar headgroup (PH) layers in cellular membranes is typically in the range of 40 Å (30 Å hydrophobic core (HC) domain, plus 5 + 5 Å for each half of the PH domain). In DPD simulations this value corresponds to

6.955 r_c, where rc is the unit length in the DPD system. From the above equivalence we determine $r_c = 5.75$ Å. The typical DPD simulation length is 2 500 000 steps, with a time step of 0.05τ that corresponds to a physical time of 11 μs.

4.4 Conclusion

Some of the properties of carbon nanoparticles and graphene in particular bear on biomolecular [110-119] and cellular interactions. [82−102] We have shown how different graphene sheets

navigate different regions of the phospholipid bilayer and its surroundings, and we have quantitatively investigated the reorganization of the bilayer induced by the presence of larger sheets. Small sheets entered the membrane without affecting the order of the phospholipids. Larger sheets adsorbed on its top, strongly affecting the order and to a lesser, but noteworthy extent, the density and the distribution of the phospholipids. The most common type of events induced by a GS was the translocation of phospholipids that occurred from the unperturbed layer to the perturbed one without inversion of polarity. The insertion of new phospholipids formed a patch of upturned molecules with their hydrophobic tails interacting directly with the hydrophobic graphene sheet. These events could induce cytotoxicity by modifying the membrane polarization and trigger apoptosis by externalization of phospholipids.

5. Frictional behaviour of molybdenum disulphide

Adapted from Dallavalle, M., Sändig, N., and F. Zerbetto "Stability, dynamics, and lubrication of MoS$_2$ platelets and nanotubes." *Langmuir*, 28 (2012): 7393

5.1 Introduction

Friction is a hundreds-of-billions-of-dollars problem. [120] It produces loss of materials and mechanical energy, unwanted release of heat, and noise pollution, to name a few related phenomena. The German tribology society claimed that yearly about 5% of the gross domestic product of any industrialized country is lost to friction, wear, and lack of knowledge on the subject. [121] To reduce unwanted friction, lubricants can be employed. Dry lubricants find a role of their own in several applications. Graphite, MoS$_2$, and WS$_2$ are effective solid lubricants. Despite being in the solid phase, they lubricate, reducing friction, just as well as liquid lubricants. They can also overcome certain limitations of liquid lubricants, such as their facility of expulsion from the gaps between moving parts of a device, and the similar facility of damage, or even impossibility of use, under high radiation conditions, in a vacuum, or in extreme-temperature applications. The lubrication properties of most dry lubricants originate from their chemical structure. As far as MoS$_2$ is concerned, the presence of three chemical features govern its tribological behavior: (1) a layered or onion-like structure, (2) weak van der Waals interlayer interactions, and (3) structural anisotropy. Crucially for practical applications, extensive research on health and safety aspects of lubricants based on fullerene-type MoS$_2$ nanoparticles proved their nontoxic and environmentally friendly performance. [122,123] The crystals of MoS$_2$ have a lamellar structure with weak binding between the sheets, just as graphite. Each sheet is composed of a plane of molybdenum atoms embedded between two layers of sulfur atoms. The van der Waals interactions between the neighboring layers are small compared to the strength of the Mo−S binding within the layer, and therefore sliding of the planes is allowed. High-resolution transmission electron microscopy (HRTEM) along with theoretical investigations have shown misfit angles between MoS$_2$ nanocrystals, [124,125] which lead to the possibility of a superlubrication regime (friction coefficient, μ < 0.01). Gradually exfoliated layers may cover the surfaces of a device to form a nanocoated structure that has been indicated as responsible for the nearly vanishing friction observed. [126,127] Furthermore, MoS$_2$ fullerenes and nanotubes (NTs) may also act like rolling tree

trunks, where the rolling can contribute to decrease the friction. It is fair to say that to date, the discussion of the friction mechanism of MoS$_2$ is still ongoing.

5.2 Computational details

The model to describe MoS$_2$ was devised with the (future) prospective of carrying out relatively long molecular dynamics runs for large systems that present a variety of morphological situations that could include broken bonds, vacancies, and in general defects. In practice, it was decided to use a simplified model that contains two terms. The first is the Coulomb interaction between the substantial charges on Mo and S atoms. These charges are not frozen but are calculated on-the-fly with the charge equilibration model, Qeq, of Rappe and Goddard. [128] The starting point of QEq is the expansion of the energy of a system of atoms as a function of the atomic charges, the ionization potentials, the electron affinities, and the Coulomb interactions, which are then calculated as a function of the interatomic distances. The charge distribution equalizes the atomic electronegativity of all atoms and is obtained by solving a set of linear equations. The treatment of the charges is therefore beyond standard static, i.e., nonpolarizable, pairwise approaches. The variation of the partial atomic charges as a function of the distance introduces polarization components typical of covalent bonds and allows the straightforward introduction of defects, for instance vacancies, in the structure. The Coulomb interatomic interactions were supplemented by an effective two-body term in the form of the Lennard-Jones potential. The Qeq model and the Lennard-Jones equation were integrated in the open source TINKER package. [129-132] The model was developed to investigate gold/molecule systems where it was shown to achieve an accuracy of 1 kcal mol^{-1}. [133,134]

5.3 Results and Discussion

There exists at least one set of Lennard-Jones parameters for MoS$_2$ systems,31 which could not be used since it was not developed in conjunction with the QEq charges. In order to parametrize the model, DFT calculations were run with the M06 functional [135] combined with the lanl2dz basis set. [136-138] The intralayer of the potential energy curve for the binding of Mo to S was almost flat, which suggested the use of a different approach. The Lennard-Jones parameters were selected on the basis of their ability to reproduce the experimental interlayer and intralayer interatomic distances. The set of parameters reported in Table 5.1 reproduce well the hexagonal 2H-MoS$_2$ polymorph (space group P63/mmc, a = 3.16

Å, c = 12.30 Å), the most stable crystal configuration. When multiple sheets are simulated they stack together correctly, and the Mo−Mo distance is 6.15 Å.17 The parameters listed in Table 1 were used to describe intraand interlayers interactions of both layered and concentric nanotube systems (Figure 5.1).

Table 5.1 Lennard-Jones parameters for the interatomic van der Waals interactions

	r_{min} (Å)	ε (kcal mol^{-1})
Mo-Mo	3.00	31.82
S-S	3.47	8.97
Mo-S	2.43	35.86
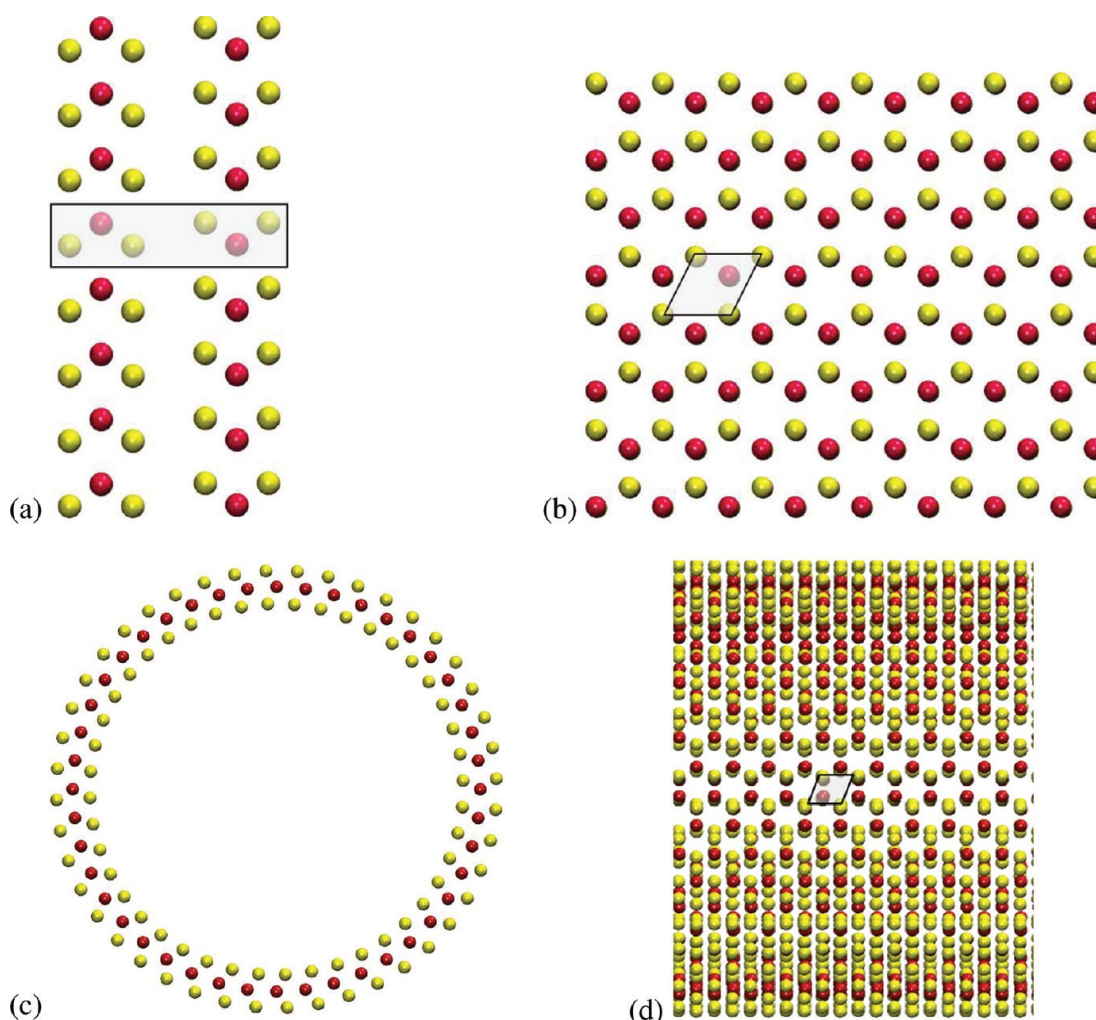
Figure 5.1 Allotropes of MoS$_2$; 2H polytype (a) front and (b) from above. An example of a single wall nanotube from (c) the front and (d) the side. Red: molybdenum atoms. Yellow: sulfur atoms. Reproduced from [III].

The charges of layers and nanotubes were obtained by the QEq model. There is good agreement between the QEq charges and those of previous investigations, Table 5.2. On the basis of these charges the interlayer energies were calculated. Experimental data are not available. Density functional tight binding, DFTB, calculations yielded a surface energy of 0.15 eV/atom [139] and an interlayer energy of −0.2 eV/atom was estimated. In the present calculations, the interlayer energy is −0.19 eV/atom. The Lennard-Jones contribution is −0.15 eV/atom and the total Coulomb term is −0.04 eV/atom, where −0.03 eV/atom are due to the Ewald summation component. Table 5.3 presents the charges at the equilibrium for (n,n) and (n,0) tubes.

Table 5.2 Charges of MoS_2 layer calculated in the present work and in previous work.

	Mo (e-)	S (e-)
present work	0.74	-0.37
Miyamoto [140]	0.76	-0.38
Varshney [141]	0.76	-0.38
Becker [142]	0.70[a]	-0.35[a]

[a]These values are affected by the nearby presence of Ag atoms.

Table 5.3 Atomic charges in the layers and NTs calculated by QEq.

	Mo (e-)	S (e-)
layers	0.74	-0.37
nanotubes	0.72	-0.36
Seifert [143]	0.9	-0.44

The study of MoS_2 nanotubes was more intensive compared to that of layers because of the variety of different geometries (armchair or zigzag), and their ability to combine single-wall NTs into multi-wall NTs. Single-Wall Nanotube Energetics. In a systematic investigation of the stability of nanotubes as a function of the diameter (d), the calculated energy was expressed as

$$E = \frac{E_{tot} - nE_{MoS2}}{n} \quad (53)$$

where E_{tot} is the energy of the nanotube, E_{MoS2} is the energy of a single MoS_2 unit, and n is the number of units in the tube. As the size of the tube increases the energies decrease. In agreement with DFTB calculations [143] and in analogy to carbon tubes, the energies follow a

$1/d^2$ law of the type.

$$f(x) = \frac{a}{d^2} + b \quad (54)$$

Armchair (n,n) nanotubes are more stable than zigzag (n,0) tubes (Figure 5.2). Previous DFTB calculations were limited to a few dozen angstroms. [143] The present simulations cover systems with lengths up to 25 nm. The increase of the size is obtained by a substantial reduction in the complexity of the computational model. A series of simulations were carried out to observe the average shape of the NTs at 298 K on 24 different nanotubes. They were performed on armchair and zigzag nanotubes with a diameter up to 17.5 nm. The armchair nanotubes with indices (22,22), (29,29), (36,36), (43,43), and (50,50) kept a regular shape during the simulation, while the curvature of the (57,57), (64,64), and (71,71) nanotubes became irregular. The cylindrical nanotube shape was almost lost for the larger tubes with (78,78), (85,85), (92,92), and (99,99) chiral vectors, and even concave curvature was observed at times (Figure 5.3). The zigzag nanotubes showed a similar behavior. Above 13.8 nm, (134,0), (146,0), and (156,0) forfeit the circular symmetry.
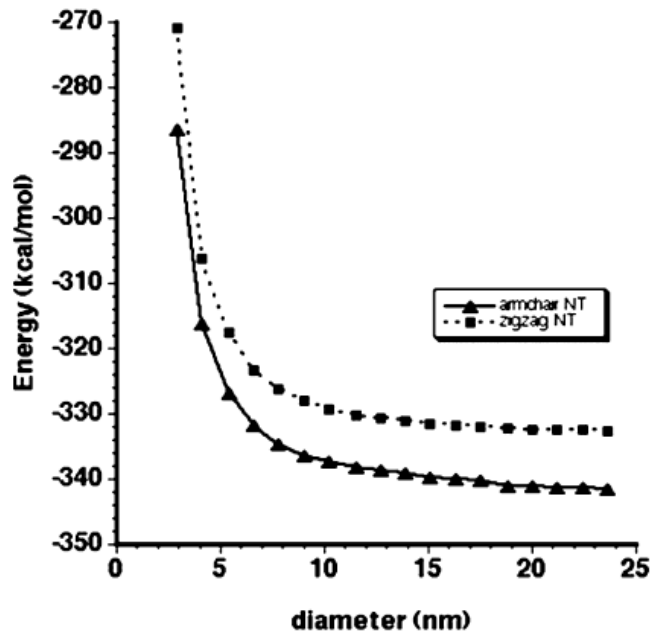
Figure 5.2 MoS_2 armchair and zigzag nanotube energy trends. Reproduced from [III].
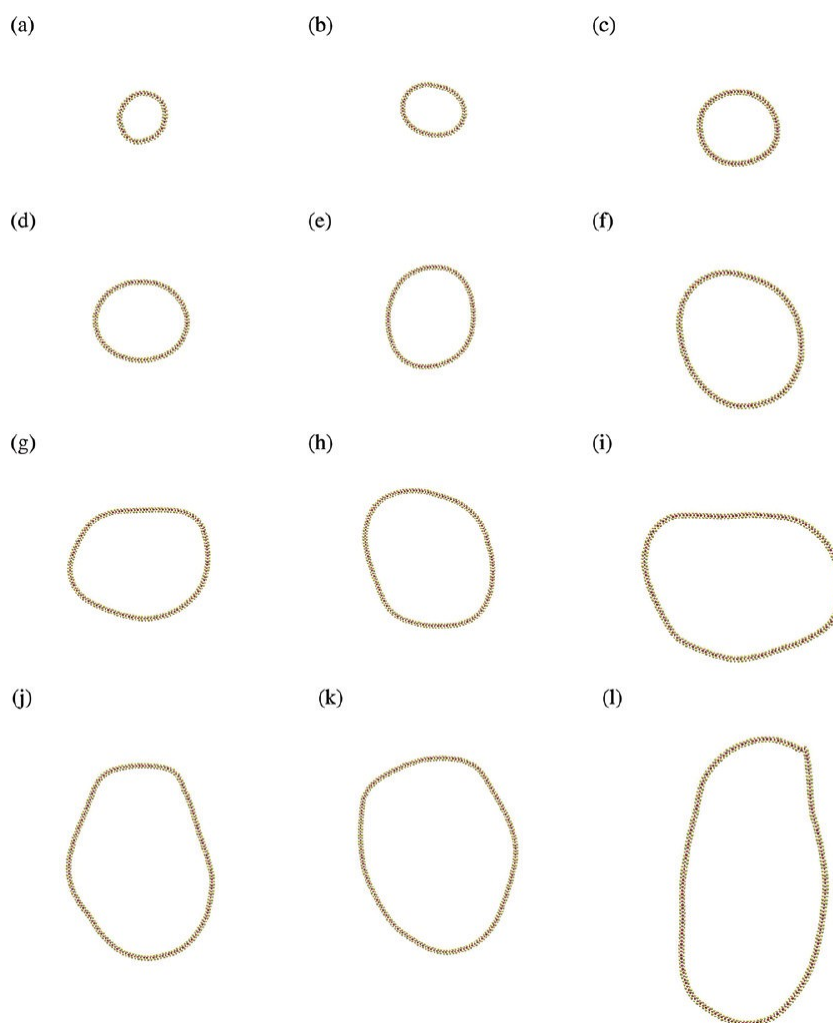
Figure 5.3 Front view of armchair nanotubes of increasing size. The chiral vectors are (a) (22,22), (b) (29,29), (c) (36,36), (d) (43,43), (e) (50,50), (f) (57,57), (g) (64,64), (h) (71,71), (i) (78,78), (j) (85,85), (k) (92,92), and (l) (99,99). Reproduced from [III].

Isolated single-wall MoS_2 nanotubes have never been detected experimentally. The minimum number of shells in the multi-wall nanotubes, MWNT, is four. [143] The interlayer van der Waals interaction plays a key role in stabilizing the MWNT. A comparison of the energies of single-, double-, triple-, quadruple-, quintuple-, and sextuple-wall NTs is instructive. Figure 5.4 compares the energy gain for the formation of concentric multi-wall NTs. The stabilization increases with the number of concentric shells and to a lesser extent with the number of atoms. The first embedding to form a double-wall NT stabilizes the structure by almost 6 kcal mol^{-1} per atom. The second embedding to form a triple-wall NT adds 2 kcal mol^{-1} more per atom. Further embedding reduces the energy gain and a plateau is reached for

sextuple-wall NTs. Thermodynamically, there appears to be a substantial stabilization, per atom, for the formation of multiwall NTs with at least four layers.
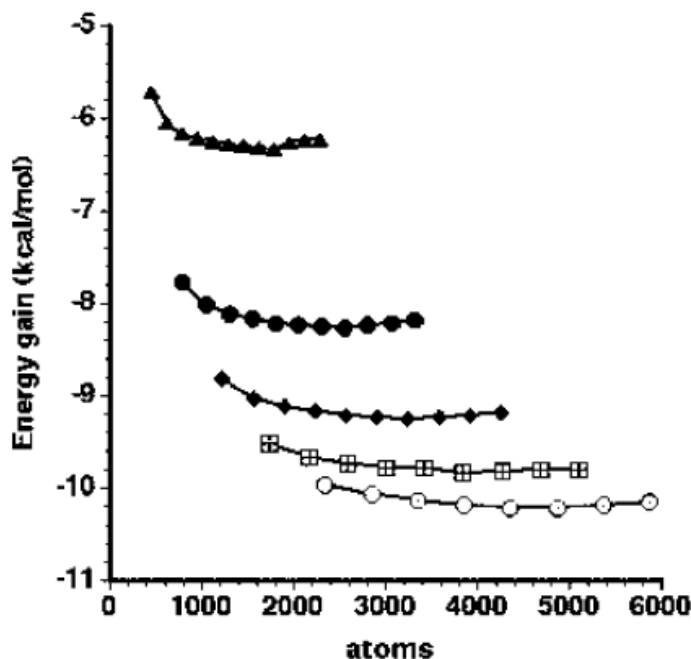
Figure 5.4 Energy stabilization per atom for concentric NTs of MoS_2; from top to bottom double-, triple-, quadruple-, quintuple-, and sextuple-wall NTs. Reproduced from [III].

In the molecular dynamics runs, sliding of the (top) layers was obtained according the protocol of Miyamoto et al.5 The velocities of the top sulfur atoms were kept constant in the adirection, while in the b- and c-directions no restrictions were imposed (Figure 5.5). During the entire simulation no change in the sliding direction was performed, which effectively removed one of the major problems of experimental data analysis. A normal load was applied on the top surface. Sliding of nanotubes was restricted to armchair double-wall, DWNT, (n,n) nanotubes, such as (29,29)@(36,36). The inner tube was anchored by keeping inactive the innermost sulfur atoms. Rigid motion along the a-axis was imposed to the external tube generating a telescopic movement (Figure 5.6). A normal load was applied in the c-direction. The algorithm to integrate the equation of motion [10] was complemented by periodic boundary conditions (PBC) and the use of Ewald summation [144] for computing the electrostatic energies. Calculations were performed in the NVT ensemble at 298 K with a 1 fs time step. The normal load applied was 0.5 GPa. The sliding velocity was 100 m/s, consistent with experimental analysis and Miyamoto et al. calculations. [124,140] Statistical averaging

was carried out on more than 10 dynamics that were run for at least 1 ns. These conditions were applied to both layers and nanotubes.

Friction of MoS_2 nanocrystals is anisotropic. Friction was therefore investigated for both a and b-directions. [124,141] Sliding in the a-Direction: during the molecular dynamics it was possible to notice that the top layer slides along a sinusoidal, zigzag route (Figure 5.7). The sulfur atoms avoid each other and try to stay close to molybdenum atoms. The amplitude of the oscillation in the b-direction is ~1 Å. This result is consistent with previously predicted sliding pathways. [124,145] A minor oscillation of nearly 0.3 Å in the c-direction was also noticed. Sliding in the b-Direction: the movement of the top layer is not sinusoidal but rather random. Occasionally, the layer can move by a large amount diagonally. Nanotubes Dynamics: concentric nanotubes were investigated with the same tools adopted for MoS_2 layers. In analogy with the case of layered MoS_2, zigzag motion of the sliding external tube was observed, although the displacement reduced to about one-third. Molecular dynamics, MD, is suited to describe nonequilibrium processes and has already been successfully applied in tribology. [124,145-149] The tribological behavior of our material was obtained from the autocorrelation function, ACF, of the forces using the Green−Kubo equation

$$K = c \int_{0}^{\infty} \langle A(t) d(t) \rangle \quad (55)$$

where K is the friction coefficient and A are the forces experienced by the system in the friction process. Alternatively, the frictional trend was obtained by classical physics Amontons' laws

$$\mu = \frac{F}{L} \quad (56)$$

or

$$\mu' = \frac{dF}{dL} \quad (57)$$

where F is the lateral friction force and L is the normal, externally applied load. In eq 56 the friction force is zero at zero load; in eq 57, the friction force is allowed to be finite at zero load. The frictional coefficient is averaged over the forces of the sulfur atoms, after equilibration of the system.
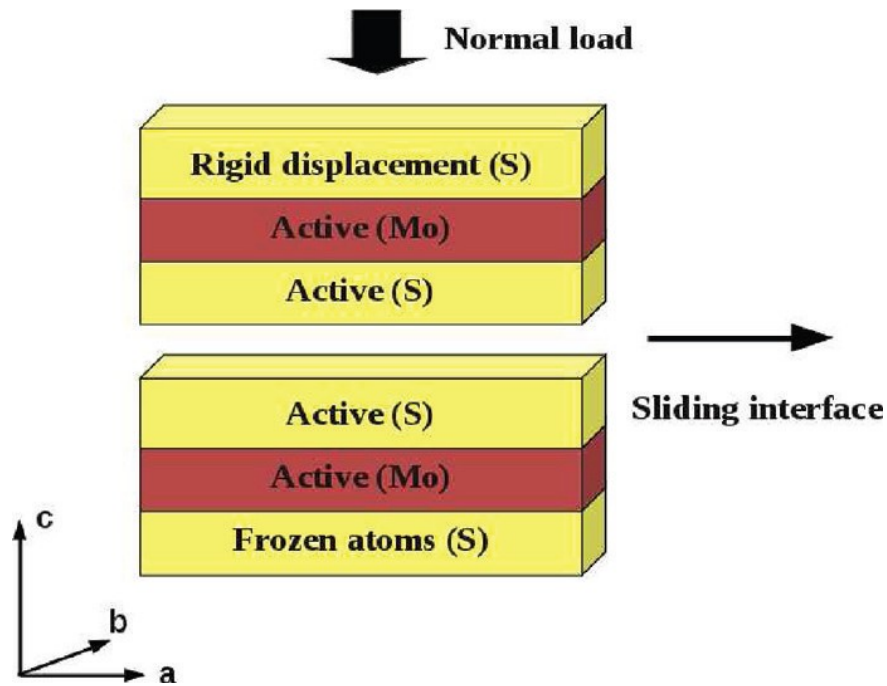
Figure 5.5 Schematic view of the sliding simulation of the layers. A rigid motion along the a-axis was imposed to the top layer, while a normal load was applied in the c-direction. Reproduced from [III].
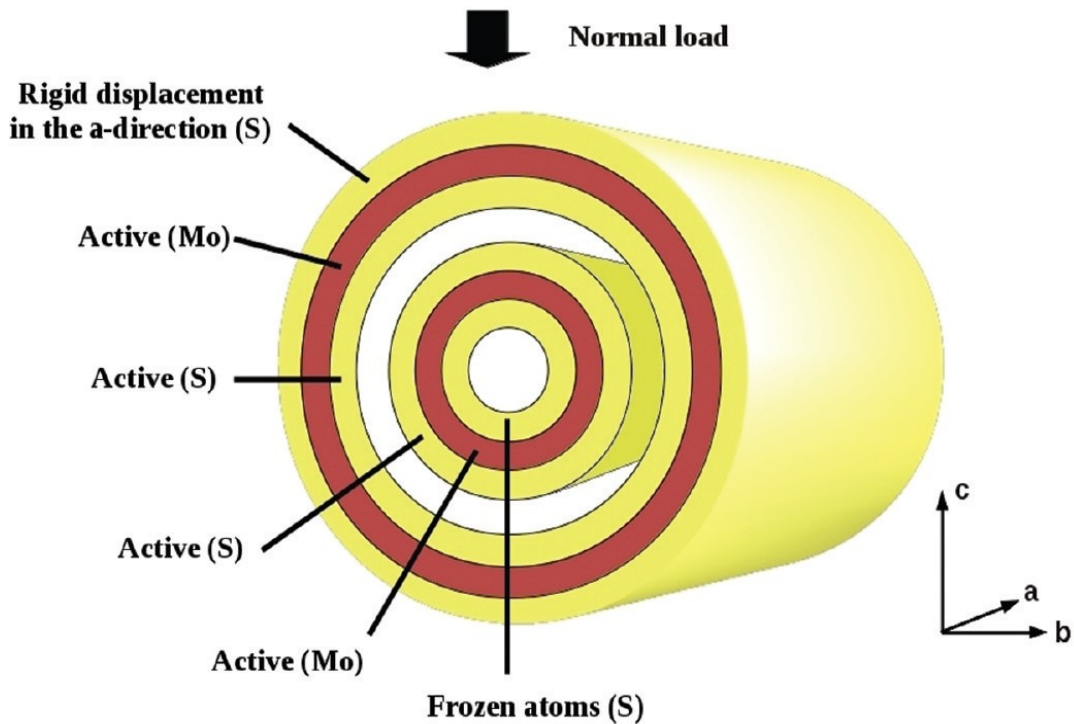

Figure 5.6 Schematic view of the sliding simulation of DWNT. A rigid motion along the a-axis was imposed to the external tube, while a normal load was applied in the c-direction. Reproduced from [III].

Frictional Behavior of the Layers. The ACF of the forces shows a damped oscillating trend (Figure 5.8). The friction coefficients of the a-direction of sliding calculated via Amontons' law and the Green−Kubo equation differ by 2 orders of magnitude and are 6.54×10^{-6} and 4.65×10^{-4}. Calculating the same coefficient for the b-direction sliding we obtained values that are smaller by ~20% and are 5.36×10^{-6} and 3.72×10^{-4}. Friction differs from that associated to the a-direction of sliding because of the smaller oscillations observed during the dynamics and because of the sudden diagonal displacement of the MoS_2 layer. Experimentally, the frictional performance of MoS_2 was reported to be in the range of 10^{-3} in ultrahigh vacuum (superlubrication regime). At environmental conditions, ultralow friction has been measured $(0.01 < \mu < 0.1)$. [123] The present idealized system does not consider defects, junctions, vacancies, asperities and impurities that increase friction. Moreover, during friction, real systems do not have a uniform distribution of temperatures because of self-heating that is not taken into account in the simulations since the thermostat dissipates the extra heat. In general, higher temperatures cause larger vibrations of the atoms, which, in turn, produce stronger friction. With all these caveats, the microscopic model based on the Green−Kubo equation appears to convey a satisfactory result that hints to a possible even higher lubrication performance of MoS_2 in optimal conditions.
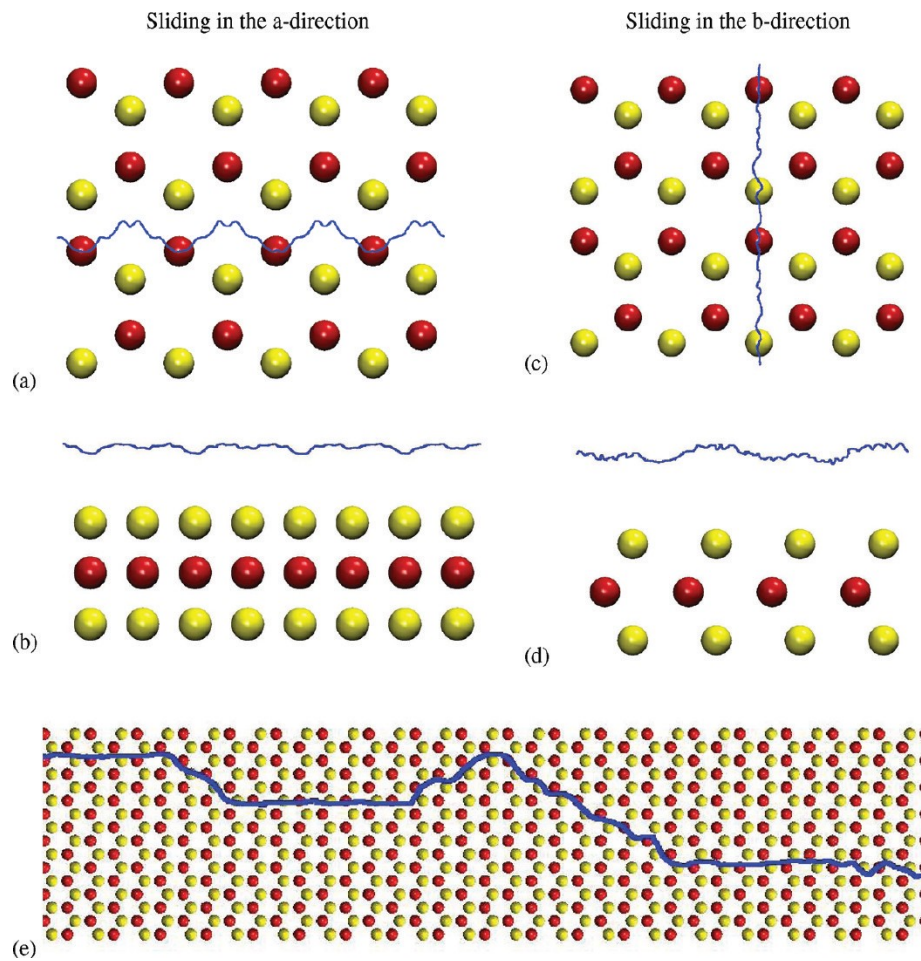
Figure 5.7 Motion of a sulfur atom for sliding in the a-direction: (a) (001) view, (b) (010) view; motion of a sulfur atom for sliding in the b-direction: (c) (001) view, (d) (010) view; and (e) zoom out of the motion for sliding in the b-direction (color code: red for molybdenum atoms, yellow for sulfur atoms, blue for pathway). Reproduced from [III].
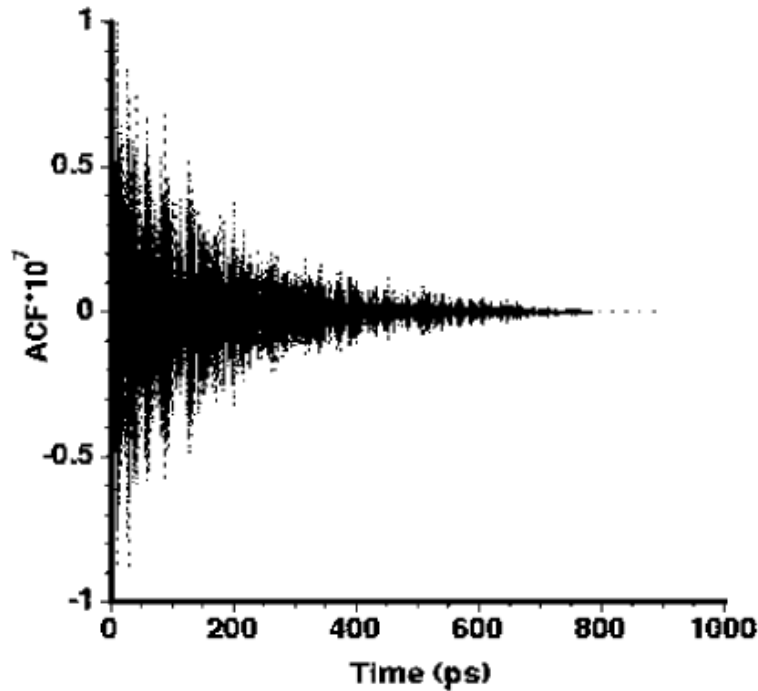
Figure 5.8 Detail of the ACF used in eq 55, which emphasizes the damped behavior. Reproduced from [III].

To improve the agreement with the experimental data, a series of simulations at different loads were run (Figure 5.9). The load-dependent friction indicates a deviation from Amontons' law. The friction coefficient varied inversely with the load since the force was nearly constant. Similar behavior is known to occur for materials such as diamond and ceramics (SiC), and has already been noticed for MoS_2. [150] From an atomistic and computational perspective, the repulsive contribution of the Lennard-Jones potential increases at higher loads, thus providing the "ground" for better sliding and a lower friction coefficient. The trend resembles that observed experimentally in the measurement of friction coefficients for bearing materials slid on MoS_2 substrates. The coefficients decreased as load increased in agreement with the Hertzian contact model. [151] Experimentally, the friction coefficient of MoS_2 has been proved to be rather insensitive to changes in the coating thickness, and no dependence of the friction coefficient on temperature has been observed, [152] while the friction coefficient is known to be related to the normal load and the sliding velocity variations. [150] These experiments were confirmed by dynamics at temperatures between 198 and 398 K ($\Delta T = 10$ K). The order of magnitude of the friction coefficient does not change. Frictional Behavior of the Nanotubes. The Amontons' law and the Green−Kubo

equation were used to calculate friction that resulted 1 order of magnitude lower than for the layered system, namely 1.84×10^{-6} and 2.94×10^{-5}. In the multi-wall nanotubes, the distances between the locations of the sulfur atoms of the different tubes are not commensurate. In the dynamics, the lack of commensurability reduces the size of the oscillating movement with respect to that observed for the layers and ultimately bears on the friction coefficient that decreases. Additional simulations were carried out with the intent of assessing the dependence of the results on the empirical parameters of the model. The van der Waals S−S interaction was modified under the constraint of conserving the crystal structure while halving the interlayer energy. The dynamics were repeated for all systems. The order of magnitude of the friction coefficient remained the same, which shows that friction is dominated by the Coulomb forces.
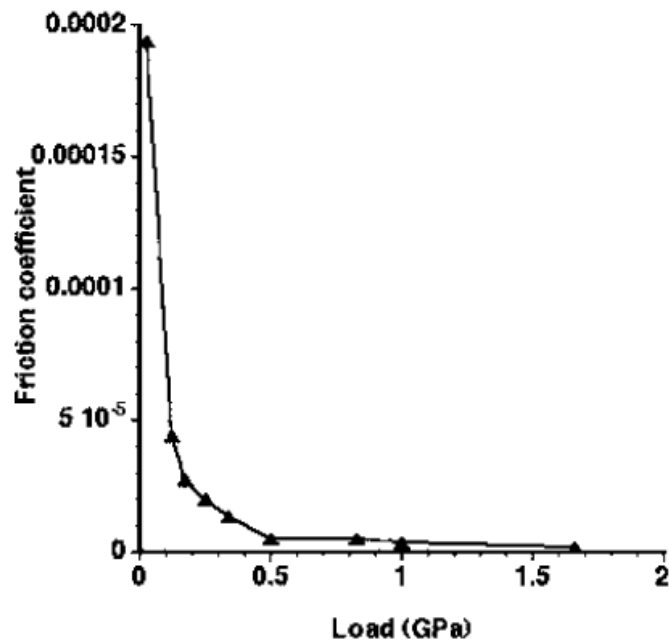

Figure 5.9 Calculated frictional performance of MoS_2 layers, load (GPa) vs dimensionless friction coefficient calculated by using Amontons' law. Reproduced from [III].

5.4 Conclusion

Computational chemistry methods can be expected to shed light on experimental observations (and vice versa). In this work, we have developed a simple model to describe MoS_2 systems, either as layers or as concentric multi-wall nanotubes. We have also tried to connect microscopic and macroscopic approaches to calculate a classic physical property such as friction. The results confirm that the excellent tribological properties of MoS_2 are amenable to improvement with the use of defective-free materials. The simulations also show that the microscopic approach is more accurate. They also supply additional structural and tribological information: (1) singlewall structures are less stable than multi-wall structures, (2) the friction coefficient can be potentially lowered for perfect materials, (3) the friction is lower for multi-wall NT than for layered systems, and (4) the friction coefficient depends on the Coulomb forces. With the advent of surface force apparatus the tribological predictions of this work can be verified experimentally.

6. Towards a cell adhesion model

Adapted from Dallavalle, M., Lugli, F., Rapino, S. and F. Zerbetto "Morphology and dynamics of cells on materials surfaces" in preparation, (2015)

6.1 Introduction

Modeling of cells, in technologically-relevant environments, could make possible to determine the chemical forces that drive their dynamics, gain fundamental knowledge on the type of environment (modifiable chemically or by drugs) that retards or accelerates diseases and degeneration, and eventually find applications in a variety of fields that range from fabrication of scaffolding for regenerative medicine, to antifouling surfaces, to the design of materials to guide stem cell differentiation, to name a few possible applications.

The cell model(s) must address morphology, motility, and organization of cells, which actually vary from cell line to cell line. In terms of morphology, cells are elastic and can assume complicated shapes. This adaptability arises also from the inner mechanics of a filamentous network. In stem cells, the tunable morphology triggered by the interaction with patterned surfaces determines cell type and tissue shape. [153,154,155] In terms of motility, cells can move on surfaces and in soft materials. Cells have developed complicated propulsion systems. For instance, the migration of a cancer cell is governed by the scaffolding protein p130CAS, which determines the growth of cell protrusions, and by the mechano-sensing protein zyxin, which represses the protrusions. Deregulation of these two competing mechanisms causes a highly persistent and directional migration of cells in cancer. [156]

In terms of collective behavior, cells seeded onto material surfaces can come together to form clusters.

The description of the cells (and also of the material) is here proposed in terms of beads. The coarse graining of the cells reduces the number of degrees of freedom to that usual in molecular dynamics simulations, MD, (i.e., a few thousand or up to a hundred thousand particles). It enormously increases the time length of the simulations from the maximum of the few microseconds that are possible in atomistic MD simulations. The explicit dynamics of the bead-based cell(s) avoids the impositions of continuum level differential equations where dynamics is determined-to a certain extent-by the form of the equation(s).

In general, the size of the beads cannot be determined *a priori*. It must be calibrated to

reproduce experimental data and depends on the type of material and the type of cell. If a relatively small cell (let say with a radius of 10 μm) is represented by ~10,000 beads, each bead is ~0.4 μ^3, for a bead-radius of ~460 nm; alternatively, if the number of beads is 100,000, each bead will be ~0.04 μ^3. The number of atoms implicitly present in a single bead is -by atomistic standards- enormous and the penalty to pay for this approach is to renounce all (or much) of the molecular level complexity of biological systems, including proteins, DNA, RNA, and lipids to name a few types of bio-molecules. The complicated inner chemical functioning of cells is also forfeited. Protein expression and/or local atomic, or truly nanometric, domains that must be present in a bead can still be modeled. The simplest strategy is to modify the description of the interactions between two beads, one of which contains the active molecule(s) of interest by modifying the potentials associated to a bead. The beads are represented by their coordinates and by potential energy functions that quantify the bead-bead interaction. The potential energy functions that describe the bead interactions are simple and soft. Simple implies the presence of a small number of parameters. Soft, actually penetrable, potentials that will be used can be traced to Hildebrand's theory of regular solutions [157] and Flory-Huggins' theory of polymers. [158] The major difference is the number of atoms of each bead that is several orders of magnitude greater than in the case of the two previously mentioned models. A "rigorous" approach to coarse graining is out of the question. Boltzmann inversion and other methods have been used to develop coarse-grain models from higher-level calculations. [159-163]

6.2 Results and discussion

Here we present a proof of concept that some features and properties of cells on materials can be simulated by a bead-based model.

Morphology is typical of the cell line. It is also related to the health status of the cell. Diseases, senescence, and the presence of toxic compounds cause morphological changes (including detachment of the cells from the tissue/substrate). Mechanical forces involved in the interaction with the microenvironment, cell adhesiveness, its stiffness and cell motility influence morphology. Variations of morphology and motility are present in cancer cells and are involved in metastasis. The counterparts of cell morphology are elasticity and adhesiveness. Cells adhesion to solid substrates is a multistep and complex process. It involves surface receptors, signalling elements and cytoskeleton. When a cell attaches to a

solid substrate, it spreads over the surface. The degree of adhesion can be expressed in terms of contact angle and shape parameters. Cells sense the stiffness and the spatial patterning of their microenvironment and modulate their shape. Mathematical models, based on minimization of the free energy have been developed. [164,165] Cell shape has a strong influence on the differentiation of human stem cell. [154] Computer simulations based on tension-elasticity model explain the cell shape that resembles a sequence of inward-curved circular arcs.(153, 166) A soft matter cell model has been proposed to study the adhesiveness between cells and their extracellular substrates. The simulations showed that the cells sense substrate elasticity by responding in different manners that range from cell spreading motion to cell contact configurations. [167]

Figure 6.1 shows cells on different surfaces. Only three parameters are required. They are: a_{CM}, a_{CS}, a_{MS}, and that are the parameters of the conservative force in the DPD model for the Cell-Medium, Cell-Surface and Medium-Surface interactions, respectively. The parameters used for these simulations are listed in Table 6.1. The result can be generalized. Surfaces 1, 2 and 3 can be considered "bio-inert", surface 4 displays intermediate adhesive properties, surfaces 5, 6, and 7 are highly adhesive. A quantitative description of cell spreading is given through the contact angle of the cell θ_C. The cell/surface contact angle is determined by fitting a spherical segment to the simulated shape, as proposed by [168]. For a sphere, the number of particles per unit of height is equal to

$$f(z) = \pi\rho\left[\left(R^2 - z_0^2\right) + 2zz_0 - z^2\right] \quad (58)$$

where R is the radius of the sphere, z0 is the distance of the centre of the sphere from the surface, and ρ is the density. The contact angle is equal to $\theta_C = 90 + \sin^{-1}\left(z_0/R\right)$ (59) in degrees. The average number of particles in a cross section of a cell as a function of the height z is presented in Figure 6.2.
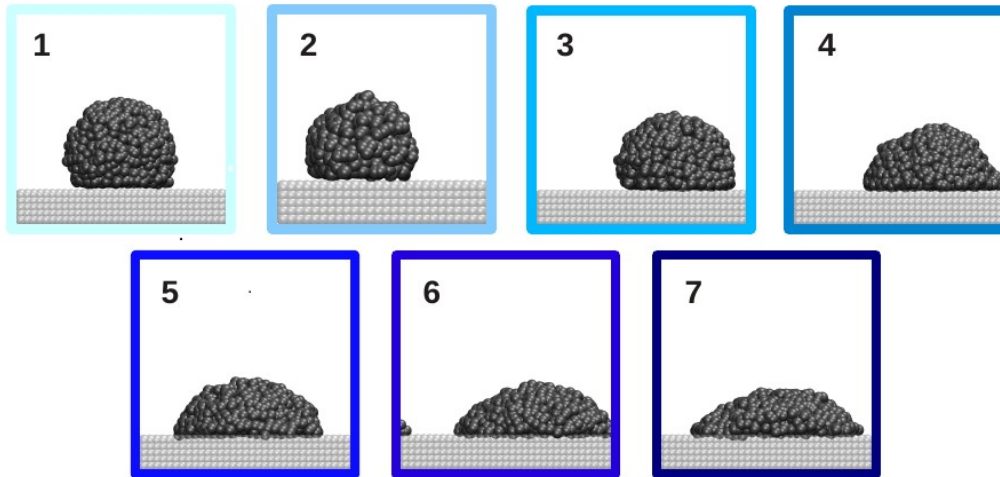
Figure 6.1 Soft Penetrable Potential of bead-based cells can reproduce the morphology of cells on different materials. Three parameters, a_{ij}, suffice to reproduce much of the behavior.

Table 6.1 Parameters used for simulating the seven surfaces displayed in Figure 6.1 a_{CS} and a_{MS} are the parameters of the Cell-Surface and Medium-Surface interactions. The Cell-Medium parameter is kept constant ($a_{CM}=80$). θ_C is the contact angle of the cell.

Surface	a_{CS} (k_BT)	a_{MS} (k_BT)	θ_C (degree)
1	100	20	127.4
2	80	20	123.2
3	60	20	117.8
4	40	40	90.0
5	20	60	65.3
6	20	80	60.2
7	20	100	56.5
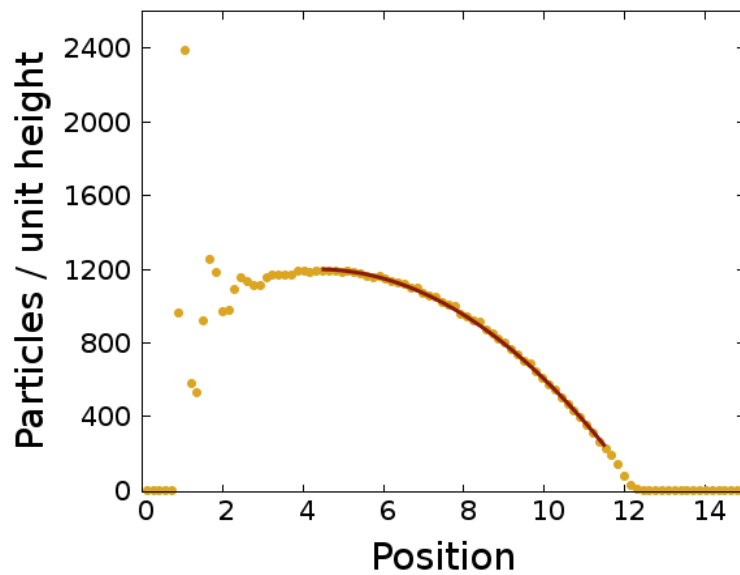
Figure 6.2 Number of particles as a function of height for a cell on the surface. The yellow dotted line is the simulation data, the red solid line is the fit. Parameter values: a_{CS} 80, a_{MS} 20.

The generic cases of Figure 6.1 can be made more specific. Figure 6.3 shows calculations with a bead-based-cell with a diameter of 15 μm deposited on an adhesive surface. The cell modifies its shape to "embrace" the ring.
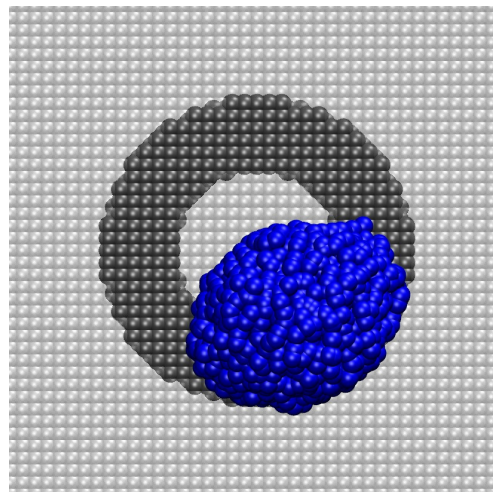

Figure 6.3 A cell on an adhesive spot of 20 μm of diameter. The topography of the substrate affects the cell behaviour.

Cells release molecules that modify their adhesion: Cells express proteins to adjust to the extracellular environment. [169] Transmembrane proteins such as integrins rearrange on the cell membrane (avidity) and undergo conformational changes (affinity) in order to adjust to the extracellular environment. The bead-based model can reproduce the main feature of this complicated process by changing the cell-substrate interaction in time. Figure 6.4 shows how the centre of mass of the cell lowers and the cell spreads when the change of the parameters is linear in time. In practice, integrin expression can be written as

$$a_{CS}(t) = a_{CS}^0 - \alpha t \quad (60)$$

$$a_{MS}(t) = a_{MS}^0 + \alpha t \quad (61)$$

where is the mean adhesion rate of a cell. By properly adjusting the value of α, it is possible to describe adhesion dynamics of different cells/surfaces or in different physiological conditions.
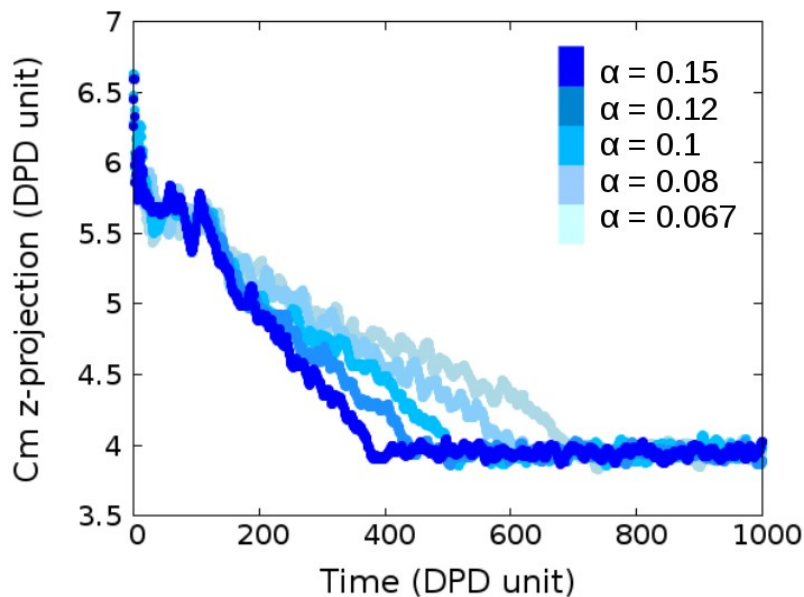

Figure 6.4 A linear change in time of the cell-surface interaction mimics the expression of adhesion proteins; together with the simulated variation of the cell shape due to protein "expression" that change the cell adhesion. Dark to light blue: decreasing α values.

Cells motion is involved in many phenomena from embryogenesis, to wound-healing, to immune response, development, and phagocytosis. Unregulated cell migration can cause progression of cancer and metastasis. Cell motility depends on cell type. Lower prokaryotic cells, such as some bacteria, swim with the aid of small appendages. Higher eukaryotic cells exhibit a (much) greater repertoire. The current concept of cell migration is based on the

haptokinetic migration. In fibroblasts, for instance, it involves at least three interdependent functional elements: the attachment of the leading edge, cell contraction, and detachment of the rear end.

Theoretical models have been developed to gain insight into basic aspects of cell motility, [170,171] many of them link the biochemistry of the cytoskeleton dynamics and/or the regulatory signalling to mechanical forces and material properties (e. g. viscoelasticity). Mathematical models are based on the solution of partial differential equation (PDE) which describe the cell as a continually deforming 2D, or 3D, object in the frame of the so called "free boundary problem". [170] A model for cell motion that uses phase-field approximation of moving boundaries for physical membrane properties has been developed. [172] It includes a reaction-diffusion model for the actin-myosin machinery and discrete adhesion sites, in a "gripping" or "slipping" mode, and integrates the adhesion dynamics with the dynamics of the actin filaments, modelled as a viscous network. A computational model that solves unsteady chemo-attractant transport equations while simultaneously executing biased random walks of individual cells has been proposed. [173] A cell migration model incorporating focal adhesion (FA) dynamics, cytoskeleton and nucleus remodeling, actin motor activity, and lamellipodia protrusion was developed for predicting cell spreading and migration behaviors. [174] Shape, size, and motility of a minimal model of an adherens biological cell have been investigated with Monte Carlo and lattice models. The cell was modeled as a two dimensional ring polymer on a square lattice enclosing continuously polymerizing and depolymerizing actin networks. [175]

The persistent motion of cells of many different types is compatible with stochastic reorientation models. [176] A bimodal correlated random walk type of motion has been proposed. [177] Classically, cell migration is characterized in terms of thermally driven Brownian motion. It is, however, an active biological process that causes an anomalous dynamics. [178] A study of T-cells demonstrated that a generalized Levy walk enables T-cells to find rare targets with an efficiency of more than an order of magnitude than in the case of Brownian random walkers. [179] Recently, the breaking of isotropy has been observed when cells move in the presence of asymmetric adhesive patterns, even on non-adhesive surface. [180] Amoeboid trajectories favor zigzag turns. It was proposed with a simple rule-based model cell, which incorporates the actual biochemistry and mechanics behind cell crawling, that zigzag motion enhances the long range directional persistence of the moving trajectories.

[181]

On the same system of Figure 6.3, individual cells were randomly placed on the surface and allowed to diffuse and explore the two-dimensional environment. Some cells eventually reach the adhesive region. The motion is a combination of purely Brownian walk with Levy components, Figure 6.5 Levy components in the cell motion have been observed experimentally. [179] In this simulation, the bead-based model hardly displays the components of cell motility that are proper of the cell, such as polarization, protrusion, adhesion, and retraction of the rear. The principal feature of the motion can, however, be captured. Future application will have to capture other behaviors such as collective U-turn, divergent migration, and unchecked migration against an obstacle [182]
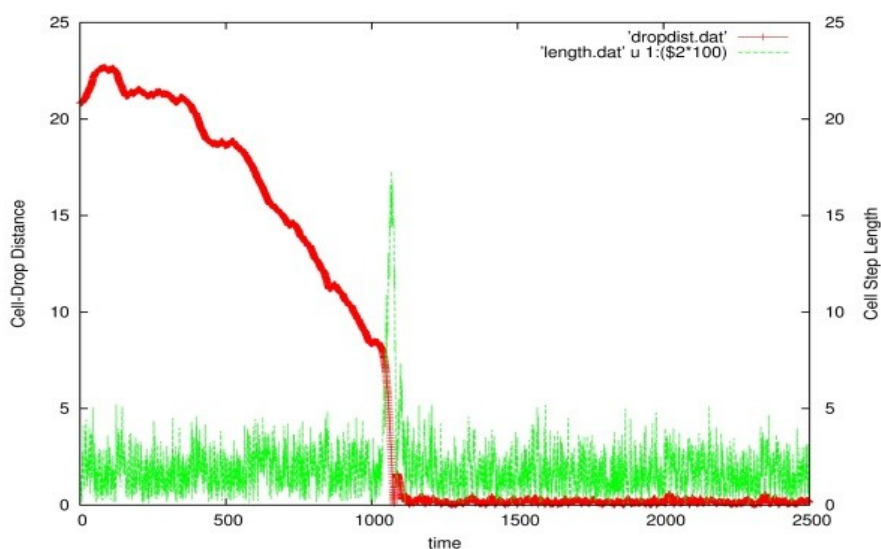
Figure 6.5 Green: length of the steps of the bead-based cell; Red: path walked by the cell in time. The presence of a Levy flight is apparent.

Cell clusters are characterized by a number of structural features. Their shape can be circular, rhizoid, irregular, filamentous or spindle. The margin can be entire, undulate, lobate, curled, rhizoid or filamentous. The elevation can be flat, raised, convex, pulvinate or umbonate. The size can be puntiform, small, moderate, or large. The texture can be smooth or rough. Cell–cell adhesion through cadherins, i.e. transmembrane proteins, is a specific characteristic of collective cell behaviour. Two types of collective behavior have been described in tumors: i) cellular sheets and strands come out from the primary site and are in contact with the primary tumor (collective invasion); ii) cell clusters detach and extend along the interstitial tissue. In chain migration cells move one after the other in strand-like fashion. The formation of such

"elastic" multi-cellular entity requires a cortical actin filament assembly along cell junctions. [183] Epithelial cancer cells can go from collective invasion to detached cell migration. Mutations in cadherins or catenins and the upregulation of proteases that cleave cadherins are often associated with the loss of cell functions [184]. Drasdo and others described the dynamics of tumor formation using an off-lattice framework [185,186]. Glazier et al. [187,188] used aggregation on lattices via cellular Potts models. Other investigations used cellular automata for a stochastic description of solid tumors, [189] continuous formulations, [190,191] reaction-diffusion type equations, [192] dissipative particle dynamics [193] and the use of methods inspired by molecular dynamics. [194] In the context of 2D motility, a number of analogous paradigms are used to describe the way cells move to close wounds or grow tissue. [195] A new model for migration of groups of cells in three dimensions, where the focus is on cell-cell and cell-ECM forces has been proposed by Frascoli et al. [196]

In terms of beads-based modeling, fluids merge when they collide. Cells retain their individuality. The size of the cluster depends also on the substrate. Figure 6.6 shows the result of the bead-based model. On a homogeneous surface all cells come together. On a patterned surface, smaller clusters are formed.
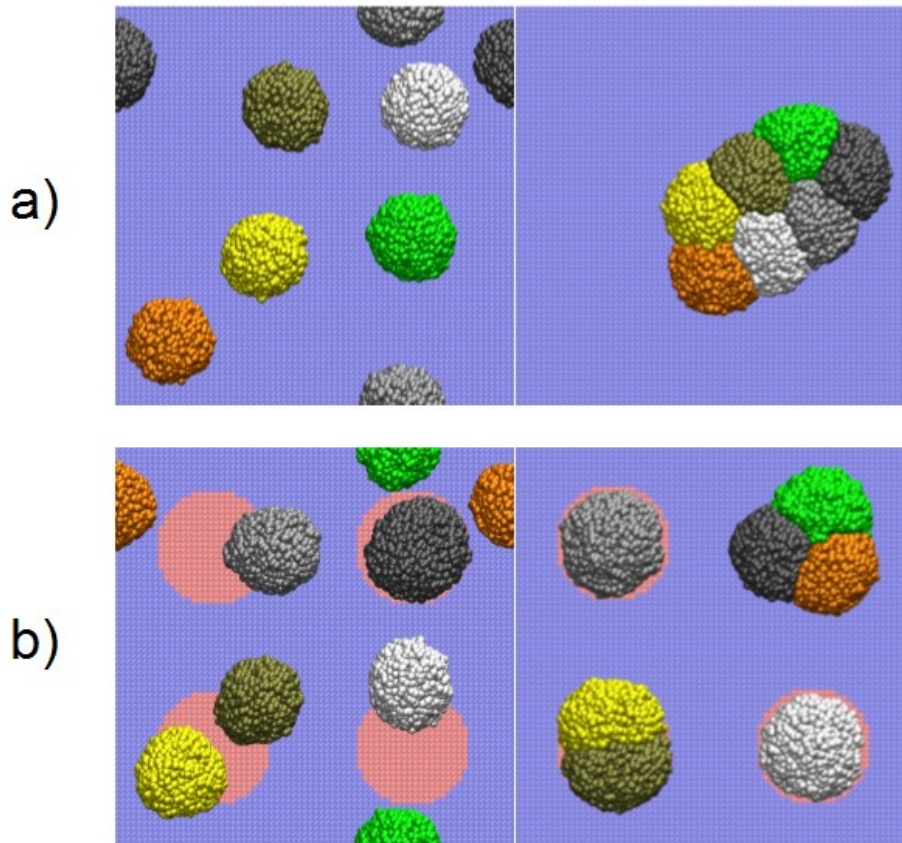
Figure 6.6 Bead-based model describes cells aggregation. From left to right: a) homogeneous surface, initially random distributed cells and final state of aggregation; b) surface patterned with adhesion points with initially randomly distributed cells and final state of aggregation. Cell colors only to assist the eye.

6.3 Experimental comparison

It has been demonstrated that patterning cell-adhesive molecules on material surfaces provides a powerful tool for controlling cell recruitment. Scriba nanotecnologie srl recently developed an experimental setup based on the laser assisted bioprinting (LAB) technique coupled with optical microscopy to pattern biomolecules on substrates with a resolution down to few micrometers and by designing complex geometry in order to generate gradients. It has been shown that the patterning of cell-adhesive protein lamin on biodegradable polymeric film made of poly(lactic-co-glycolic acid) (PLGA) may promote stem cell adhesion. In this framework we developed a computational model to estimate the probability of cell adhesion (P_A) onto a chemically patterned surface as a function of the pattern geometry.bIn the model, PLGA surface is created by freezing the motion of DPD particles. Laminin droplets of 20 ˏm

diameter, which are experimentally patterned on the surface by LAB technique, are created by modifying beads types on the surface (see Figure 6.7).
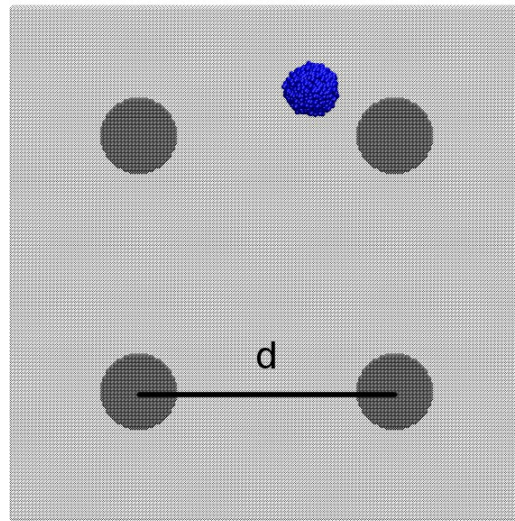

Figure 6.7 Model setup for DPD simulations of cell adhesion onto chemically patterned surfaces. The cell (blue) has a diameter of 15 μm, the laminin droplets diameter is 20 μm (dark grey). The distance between laminin droplets d is 40, 70, 100 μm.

The adhesion probability (P_A) of a cell has been studied as a function of the pattern size, d, expressed as the distance between the centres of laminin droplets. The probability of adhesion of a single cell was estimated by running N statistically independent simulations with the following procedure:

1) Initially the cell is randomly placed on the surface.

2) The cell diffuses, exploring the two-dimensional environment.

3) The cell senses the adhesive region and moves toward the laminin droplet.

4) During the adhesion process, the cell undergoes a morphological change.

If the cell eventually reaches a laminin droplets, which has a favourable interaction with cell beads, it spreads on it and it can be considered attached on the surface (P_A=1). If not, the cell does not adhere and eventually can die (P_A=0). The probility of adhesion is calculated as a function fo pattern geometry by averaging the results of the N simulations. Preliminary result are shown in Figure 6.8 and Table 6.2.
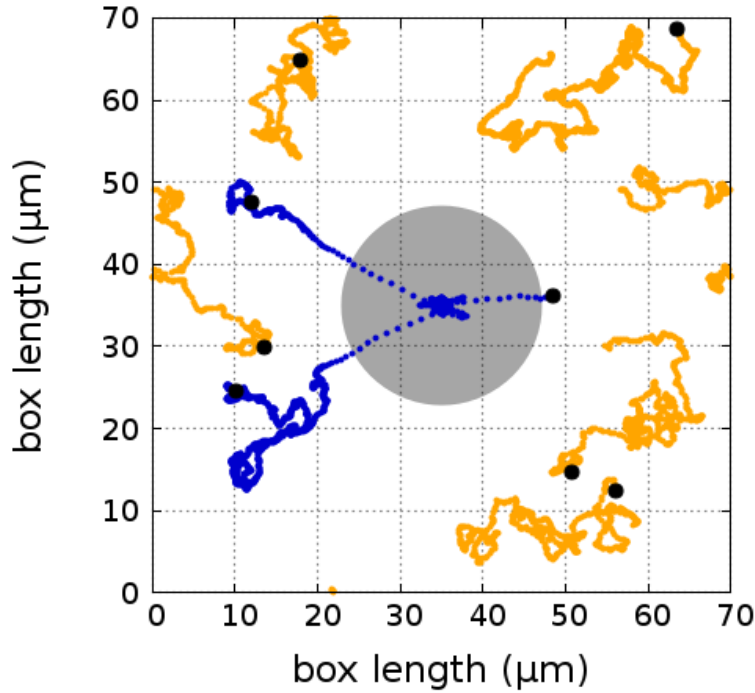
Figure 6.8 Trajectories of the cell centre of mass on patterned surface. Blue trajectories, the cell is able to reach the laminin droplet within t_{end}, yellow trajectories, the cell is unable in the given time to reach the droplet. black spot, position of the cell at t_0. 100 independent trajectories have been sampled for each system, but only 8 are depicted.

Table 6.2 Probability of adhesion (P_A) as a function of pattern geometry (d).

d (μm)	P_A
40	99%
70	46%
100	21%

6.4 Computational details

Cells are treated as soft matter aggregates described by a collection of DPD beads immersed in a liquid medium. A single cell is placed on a planar solid surface occupying the bottom section of the simulation box. The surface beads are arranged in a face-centred cubic structure kept frozen during the simulation. In a first attempt of cell modeling, the number of beads per cell is chosen close to 1,000. In a second group of simulation, the degree of coarse-graining is reduced. We opt for 10,000 beads per cell. Interactions between two bodies each made by a (large) number of atoms have long been described. Hildebrand's theory of regular solutions uses the exchange parameter, χ_{ij}, which weighs the interaction energies of the molecules in

their pure phases and their solution. Flory-Huggins' theory of polymers uses a similar parameter to obtain many thermodynamics properties. Such parameter quantifies the interactions between two bodies of many atoms. It can be thought as the energy cost of starting with the pure phases of i and j and transferring one i object into the j phase and one j object into the i phase. Dependence on the distance, necessary for molecular dynamics, is introduced in a simple way. We employ a soft repulsive description of the interactions as defined in equation 29, because of past experience with the potentials. The parameters are presented inTable 6.1. The temperature of the system is set at 0.53.

6.5 Conclusion

Emphasizing morphological changes due to the environment can be used for diagnosis. The characterisation and simulation of cell migration on different materials and in different microenvironments will allow to identify a material that can emphasize differences in the motility of malignant and normal cells in a very early stadium. Such a material can be used for the early diagnosis of malignancy in biopsies and for theragnostic applications. The characterisation and simulation of cell cluster dynamics on different materials and in different microenvironments will allow to determine materials that can emphasize differences in individual and collective motility. However, the bead-based model does not address the complexity of the living. Molecular-level response is not and cannot be considered. The investigation of a variety of cell responses to different materials can provide guidelines in order to make cells do what is required of them. Cells can be the factories of the future if only we learn how to make them do the work for us. [197] Cells can themselves be materials, for instance when they show auxetic behavior. [198,199] Technical care has to be exerted with the present approach. For instance, but this is only an example, the definition and size of the beads requires that they be as large as possible without becoming so large that their nature changes over to granular.

7. Mathematical modeling of polymer swelling and its application to PLGA

7.1 The model

When a dry polymer is placed in contact with a thermodynamically good solvent, the solvent enters the polymer and may induce major structural changes in its morphology. The polymer responds to the stimulus provided by the permeation of the solvent, with a mechanical action, this is, a volume change. Mathematical models of swellable polymers involve at least two aspects, the diffusion of the penetrant in the polymer and the volume changes due to penetrant adsorption. As far as the transport is concerned, diffusion in polymers is not always best described by Fick's law. In 1966 Alfrey, Gurnee, and Lloyd distinguished three types of diffusion according to the relative rates of diffusion and polymer relaxation [200]. They were (i) Case I or Fickian diffusion, (ii) Case II or diffusion and (iii) Case III or non-Fickian or anomalous diffusion. [200]

To distinguish between these regimes the Deborah number, De, is introduced

$$De = \frac{\lambda}{\theta} \quad (62)$$

where λ is the characteristic stress-relaxation time of the polymer-penetrant system and θ is the time for diffusion of the solvent in the polymer [201]. Depending on the magnitude of *De*, the process may be Fickian or Non-Fickian. For *De* >> 1 the Fickian regime dominates as the solvent diffuses through the unswollen polymer. For *De* << 1 Case II transport occurs, the solvent penetrates mainly through the swollen polymer. If the rates of the solvent diffusion and polymer relaxation are comparable, *De* ~ 1, the transport mechanism is often called anomalous or Non-Fickian. From a microscopic point of view, diffusion is influenced by the polymer uncoiling which occurs at about the same rate of the penetrant transport. The relaxation of the macromolecules is strongly coupled to the diffusion of the solvent. Among the anomalous behaviors observed, oscillation-with-decay and overshoot sorption have been reported. [202,203] .

In order to model closely experimental and practical situations we chose a numerical approach. The backbone of the model is based on Peppas et al.'s work. [204] The model explicity describes swelling. It is able to portray a range of diffusional behaviours, from Fickian to Case II. Non-ideal concentration effects on the diffusion coefficient can be included. The model is solved numerically using finite element methodology. [205]

At the basis of the model is Fick's law

$$\frac{\delta C}{\delta \tau} = \frac{\delta}{\delta \xi}\left(D \frac{\delta C}{\delta \xi}\right) \quad (63)$$

where

$$C = \frac{C_w}{C_{w,e}} \quad (64)$$

with Cw,e the equilibrium concentration of the solvent, C becomes a normalized concentration. The spatial coordinate is normalized with respect to the polymer dry thickness (65) and the penetrant diffusion coefficient normalizes the time scale (66)

$$\xi = \frac{x}{L_0} \quad (65) \quad \tau = \frac{Dt}{L_0^2} \quad (66)$$

Boundary and initial conditions of the system are expressed by equations (67) and (68). The concentration at the two interfaces is set at 1 to mimic a polymer film placed in an infinite bath of penetrant. Initially, the concentration of the solvent inside the polymer is set to zero.

$$C(0, \tau) = C(\xi, \tau) = 1 \quad (67)$$
$$C(\xi, 0) = 0 \quad (68)$$

Diffusion coefficients in polymer systems are often concentration dependent. The normalized diffusivity is taken as an exponential function of the concentration according to the free-volume theory. [206] The diffusion coefficient is described by a Fujita-type exponential

$$D = e^{-\beta(1-C)} \quad (69)$$

where β is a parameter defining concentration dependence of D. Figure 7.1 illustrates the relationship between the diffusion coefficient D and the normalized concentration C with varying β. An increase of β decreases the diffusion coefficient.

The polymer response to the diffusant is explicity modeled. The space has been divided into 20 layers each of width 0.05 (in dimensionless units). The layers are further subdivided by

multiple meshes. Each layer is allowed to expand according to the amount of diffusant it contains. A high solvent concentration results in more swelling. The material response is controlled by

$$\Delta\xi_{1,i} = \frac{\Delta\xi_0}{\left(1 - v_e C_i\right)} \quad (70)$$

$$\Delta\xi_{3,i} = \left[\frac{\Delta\xi_0^3}{\left(1 - v_e C_i\right)}\right]^{1/3} \quad (71)$$

Initially the polymer slab is glassy in nature, which prevents isotropic diffusion. The diffusion of the solvent molecules is restricted to one-dimension with the elongation of the polymer layer governed by (70). As a solvent concentration sufficient to plasticize the polymer is reached, the mechanism of transport changes. The movement of the solvent molecules is less hindered by the material. The process of diffusion becomes three-dimensional and the polymer swells following eq. (71). Both the one and three-dimensional processes are governed by the material constant v_e, but the one-dimensional process elongates the system to a greater extent than the isotropic process.

In Peppas' model the polymer relaxation process is not directly portrayed. Relaxation is assumed to be faster than the sorption process and virtually instantaneous. It can be thought as a vertical drop in volume, as the system moves from the 1D to the 3D regime. Experimentally the structural changes in the polymer are slow and the relaxation time is not zero. A better description of the relaxation is provided by Ishida et al. [207] A time-dependent formulation of the polymer relaxation is given as

$$\Delta\xi_R = c\tau^B \quad (72)$$

where c and B are parameters linked to the polymer relaxation time.

7.2 Results and Discussion

In this section we address three simplified cases before applying the model to PLGA. Initially, we consider Fickian diffusion. The coefficient D is assumed independent of the concentration, i.e. β equal 0. The swelling is considered negligible and v is set to 0. The concentration profile in Figure 7.2 shows a progressive smooth penetration of the solvent into the material from the external interfaces. The profile is half of a Gaussian function whose width increases with time. The response is symmetric with respect to $L_0/2$. Similar results can be obtained analytically. [208]

Then, we take into account a diffusion coefficient that depends on the concentration of the penetrant. The concentration profile in Figure 7.3 shows sharp advancing concentration fronts that meet at the centre of the sample. The solvent uptake is slow in the unsolvated polymer domain, while it becomes faster in the region where the polymer has already been solvated. The solvation of the macromolecules favors chain rearrangement, which leads to an increment of the free volume. The solvent diffusion path is less hindered. The model is responsive to changes in β. An increase in β results in sharper profiles and reduced front velocity, up to the point where the solvated region and the dry portion of the polymer are sharp-cut separated. This numerical solution can be seen as a Case II diffusion. The most characteristic feature for Case II diffusion is an advancing concentration front moving at a constant velocity. It can be modeled by adjusting the grid size and increasing β to 9. [204]

In the third system, we introduce the swelling factor (Figure 7.4). The swelling process is assumed monodimensional and the material constant v is set to 0.5. The parameter β is set to 2. Both swelling and diffusion coefficient depend on the concentration. As expected the concentration profile is modified and the system expands to the right and to the left.
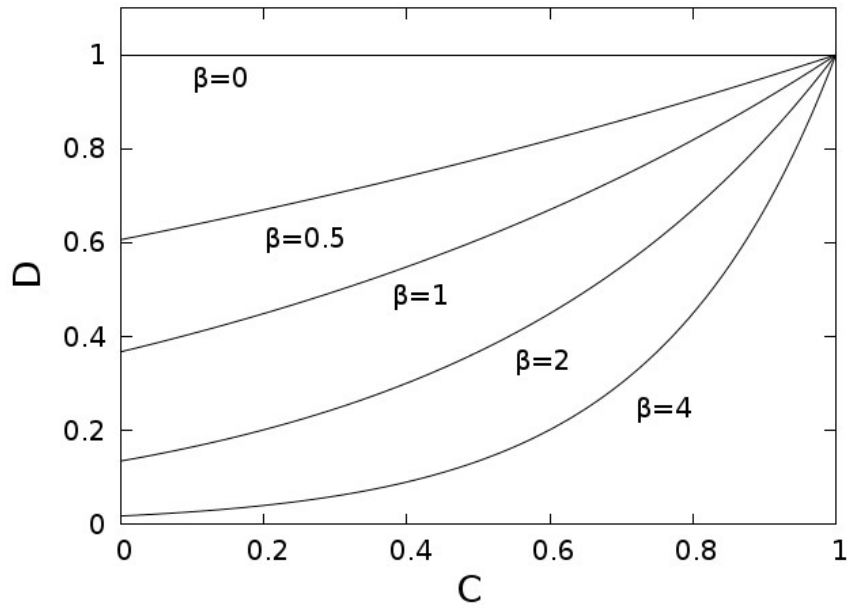
Figure 7.1 Diffusion coefficient-concentration relationships. The dependence of the diffusion coefficient on the concentration is controlled by equation 69 through β. Reproduced by permission of The Royal Society of Chemistry, adapted from [V].
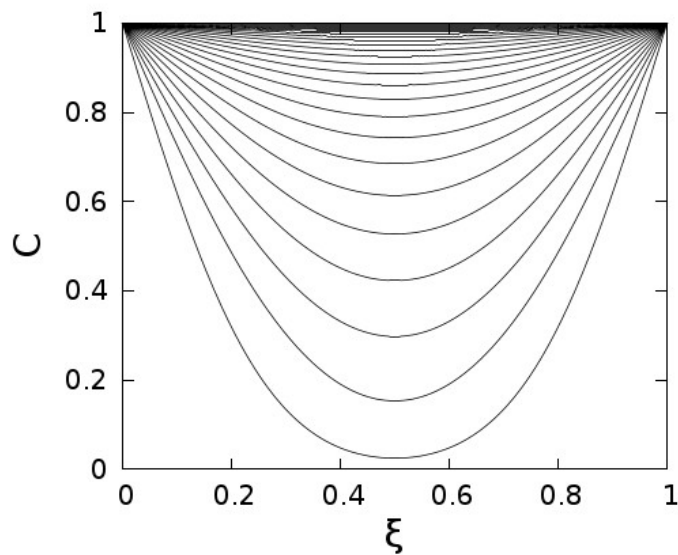

Figure 7.2 Time evolution of concentration profile with constant diffusion coefficient ($\beta=0$) and no swelling ($v=0$). Lines refer to dimensionless time increments $\Delta\tau=0.02$. Reproduced by permission of The Royal Society of Chemistry, adapted from [V].
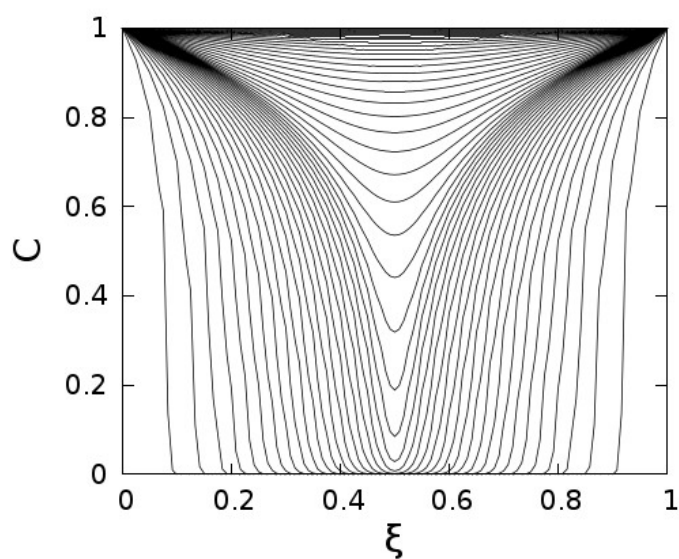
**Figure 7.3** Time evolution of concentration profile with concentration-dependent diffusion coefficient ($\beta=5$) and no swelling ($\nu=0$). Lines refr to dimensionless time increments $\Delta\tau=0.02$. Reproduced by permission of The Royal Society of Chemistry, adapted from [V].
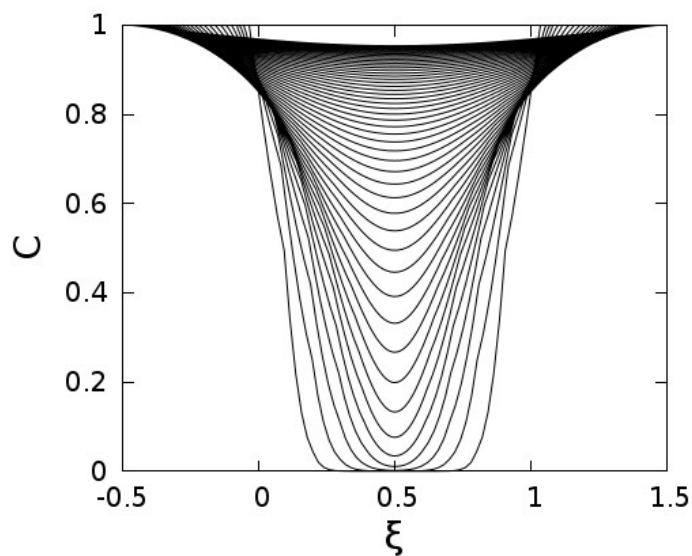

Figure 7.4 Time evolution of concentration profile for nonconstant volume and nonconstant penetrant diffusion coefficient ($\beta=2$). The process is assumed monodimensional and the material constant ν is set to 0.5. Lines refer to dimensionless time increments $\Delta\tau=0.02$. Reproduced by permission of The Royal Society of Chemistry, adapted from [V].

In order to accommodate the solvent molecules the polymer chains rearrange. With respect to

the diffusion of the solvent, part of the movement may be almost instantaneous and part relatively slow.[209] The instantaneous change consists of the movement of individual functional groups and/or small segments of chains. The instantaneous volume change takes place in the first part of Figure 7.5 (or Figure 7.6). The diffusion coefficient is concentration-dependent ($\beta=1$). Since the swelling process appears to be coupled with solvent penetration we set v to 0.76.

The slow response is triggered by internal stresses experienced by the polymer due to the presence of the diffusant. It involves the uncoiling/rearrangement of large segments of the polymer chains. The slow volume change appears in the second part of the Figure 7.5 (or 7.6). A similar behavior occurs to polymers under other circumstances, for instance polymers subject to a sudden increase in temperature. [210] When the temperature is suddenly increased the polymer undergoes an instantaneous expansion, followed by a slow shrinking. The description of the relaxation process is considered as proposed by Ishida. The experimental results are fitted as c=1.12, B=0.21.

As soon as the stresses are removed further uptake is possible. The polymer is solvated and the diffusion coefficient is no longer concentration dependent ($\beta=0$). The value of v is kept at 0.76. The process is slow and the volume changes. This feature is depicted in the third part of Figure 7.5 (or 7.6).

We assumed PLGA degradation to be negligible in the early stages of the process. The time scales of diffusion and degradation process are not the same. The polymer film has to be solvated before it can undergo hydrolysis. It has been reported that PLGA follows a first order degradation process, which starts after the first week. [211]

7.3 Conclusion

In summary, a model to gain understanding of the coupled diffusion-swelling process in PLGA is proposed. It describes the three regimes that have been experimentally observed (Figure 7.5 or Figure 7.6) 1D diffusion dominates in the first region. The initial swelling is followed by the polymer relaxation. As the stresses are dissipated by the viscous flow of the polymer, a second swelling is observed.
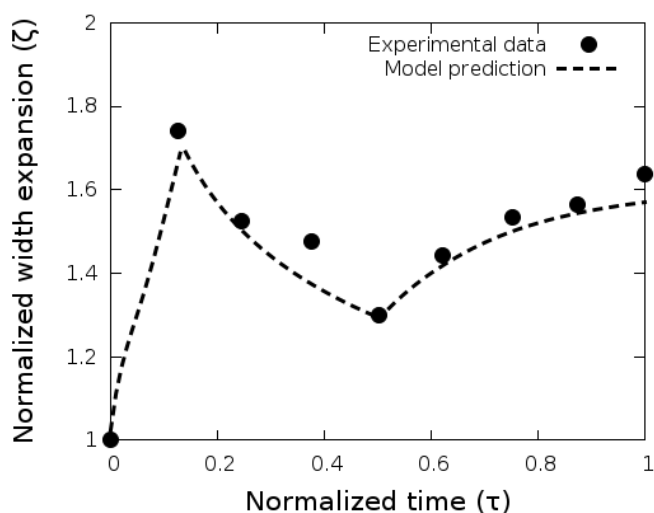
Figure 7.5 Normalized width expansion of the PLGA as a function of time. Experimental results are in agreement with the solution of the model, which is plotted as a dashed line. Reproduced by permission of The Royal Society of Chemistry, adapted from [V].
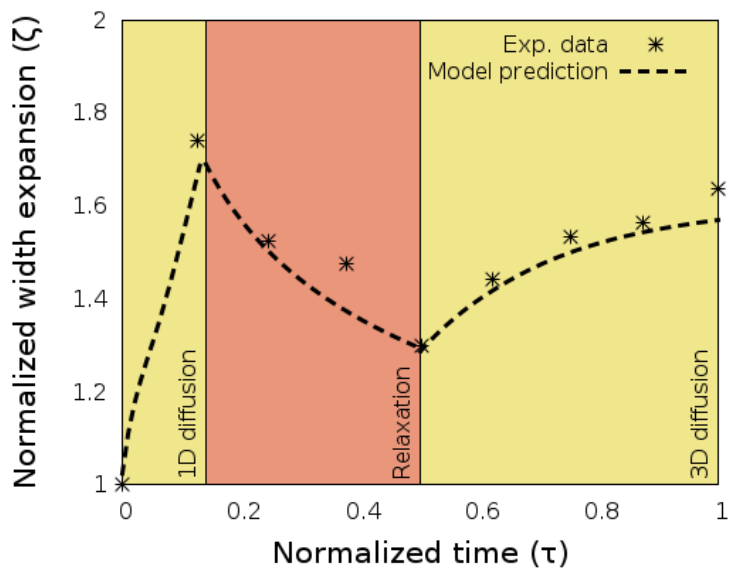

Figure 7.6 Normalized width expansion of the PLGA as a function of time. Three regimes of the polymer volume changes are highlighted: (1) Initial swelling, (2) Relaxation, (3) Final swelling. Experimental results are in agreement with the solution of the model, which is plotted as a dashed line. Reproduced by permission of The Royal Society of Chemistry, adapted from [V].

8. Concluding remarks

"*If we were to name the most powerful assumption of all, which leads one on and on in an attempt to understand life, it is that all things are made of atoms, and that everything that living things do can be understood in terms of the jigglings and wigglings of atoms.*" [212] Staying true to Feynman's quote, a classical description of biological systems like membranes, micelle and living cells is provided. Instead of the "jigglings and wigglings of atoms" the motion of particles, termed as bead, is considered. The systems are coarse grained to the level of hydrophobic and hydrophilic interactions. This second assumption extends the applicability of molecular dynamics over longer times and larger scales.

In this dissertation five chemistry-related problem are addressed by means of theoretical and computational methods. The main results can be outlined as follows.

A systematic study of the effect of the concentration, chain length, and charge of surfactants on fullerene aggregation is presented. [I] The location of C_{60} in micelles is recorded, step-by-step, during the dynamics and fullerenes are found in the hydrophobic region of the micelles. If the available hydrophobic space increased, C_{60} is localized in the inner part of the micellar core. Short, charged amphiphilic stabilizers are more effective at dispersing fullerenes monomolecularly. Two different phases of C_{60} are observed as the C_{60}/surfactant ratio varies. In the first, aggregates of C_{60} are entrapped inside the micelles, whereas, in the second, colloidal nanoC_{60} is formed with surfactants adsorbed on the surface.

The interactions between graphene sheet of increasing size and phospholipid membrane are quantitatively investigated. [II] Small hydrophobic graphene sheets pierce through the phospholipid membrane and navigate the double layer, intermediate size sheets pierce the membrane only if a suitable geometric orientation is met, and larger sheets lie mainly flat on the top of the bilayer where they wreak havoc with the membrane and create a patch of upturned phospholipids. The effect arises in order to maximize the interaction between hydrophobic moieties and is quantitatively explained in terms of flip-flops by the analysis of the simulations.

A model is proposed to study structure, stability, and dynamics of MoS_2, a material well-known for its tribological properties [III]. The telescopic movement of nested nanotubes and the sliding of MoS_2 layers is simulated. The friction coefficient is calculated via Amontons and Green-Kubo formalism. The model is used for qualitative as well as quantitative

predictions.

A soft matter cell model is developed to explore the interaction of living cell with artificial surfaces [IV]. The effect of the surface properties on the adhesion dynamics of cells are discussed. The investigation of morphology, dynamics of individuals, and collective behavior of clusters of cells on materials is possible. Distinctive features of cell behaviour are described.

A mathematical model to gain understaning of the coupled diffusion-swelling process in poly(lactic-co-glycolic acid), PLGA, is proposed. [V] The model is solved numerically using the finite element method. The numerical scheme is able to describe three regimes of the PLGA behaviour: initial swelling, relaxation, final swelling. The performed calculation help to rationalize the experimental data.

The following papers, referred to in the text by their Roman numerals, are reproduced to some extent in the thesis.

[I] Dallavalle, M., Leonzio, M., Calvaresi, M., and F. Zerbetto "Explaining fullerene dispersion by using micellar solutions." *ChemPhysChem*, 15 (2014): 2998

[II] Dallavalle, M., Calvaresi, M., Bottoni, A., Melle-Franco, M., and F. Zerbetto "Graphene can wreak havoc with cell membranes" *ACS Applied Materials & Interfaces,* 7 (2015): 4406

[III] Dallavalle, M., Sändig, N., and F. Zerbetto "Stability, dynamics, and lubrication of MoS_2 platelets and nanotubes." *Langmuir*, 28 (2012): 7393

[IV] Dallavalle, M., Lugli, F., Rapino, S. and F. Zerbetto "Morphology and dynamics of cells on materials surfaces" in preparation, (2015)

[V] Dumitru, A. C., Espinosa, F. M., Garcia, R., Foschi, G., Tortorella, S., Valle, F., Dallavalle, M., Zerbetto, F., and F. Biscarini" *In-situ* nanomechanical characterization of the early stages of swelling and degradation of a biodegradable polymer" *Nanoscale* accepted, (2015), DOI: 10.1039/c5nr00265f

References

[1] M. P. Allen, D. J. Tildesley, "Computer simulation of liquids." *New York: Oxford* 385 **(1989)**.

[2] D. Frenkel, B. Smit, "Understanding molecular simulation: from algorithms to applications." *Academic press* 1 **(2001)**.

[3] H. F. Schaefer, *Science* **1986**, 231, 1100-1107.

[4] K. B. Lipkowitz, *J. Chem. Educ.* **1995**, 72, 1070-1075.

[5] A. R. Leach, "Molecular Modelling: Principles and Applications" *Prentice Hall: Dorchester*, UK, **(2001)**.

[6] L. Verlet, *Phys. Rev.* **1967**, 159, 98-103.

[7] R. W. Hockney, *Methods Comp. Phys.* **1970**, 9, 136-211.

[8] C. S. William, C. A. Hans, H. B. Peter, R. W. Kent, *J. Chem. Phys.* **1982**, 76, 637-649.

[9] D. J. Beeman, *Comput. Phys.* **1976**, 20, 130-139.

[10] B. R. Brooks, "Algorithms for Molecular Dynamics at Constant Temperature and Pressure", *DCRT Report, NIH*, **(1988)**.

[11] R. D. Groot, P. B. Warren, *J. Chem. Phys.* **1997**, 107, 4423−4435.

[12] P. J. Hoogerbrugge, J. M. V. A. Koelman, *Europhys. Lett.* **1992**, 19, 155-160.

[13] Y. Duan, C. Wu, S. Chowdhury, M. C. Lee, G. Xiong, W. Zhang, R. Yang, P. Cieplak, R. Luo, T. Lee, J. Caldwell, J. Wang, P. J. Kollman, *Comput. Chem.* **2003**, 24, 1999-2012.

[14] T. C. Germann, K. Kadau, *International Journal of Modern Physics* C *2008*, 19, 1315-1319.

[15] B. M. Forrest, U. W. Suter. *The Journal of chemical physics* **1995**, 102, 7256-7266.

[16] P. Español, M. Serrano, I. Zuñiga, *International Journal of Modern Physics C* **1997**, 8, 899-908.

[17] S. Izvekov, G. A. Voth, *J. Chem. Phys.* **2005**, 123, 134105.

[18] H. Lei, B. Caswell, G. E. Karniadakis, *Phys. Rev. E* **2010**, 81, 026704.

[19] E. Brini, E. A. Algaer, P. Ganguly, C. Li, F. Rodríguez-Ropero, N. F. van der Vegt, *Soft Matter*, **2013**, 9, 2108-2119.

[20] P. Español, P. Warren, *Europhys. Lett.*, **1995**, 30, 191-196.

[21] R. D. Groot, J, *Chem. Phys.*, **2003**, 118, 11265-11277.

[22] T. Soddemann, B. Dünweg, K. Kremer, *Phys. Rev. E* **2003**, 68, 046702.

[23] P. Espanol, *Phys. Rev. E* **1995**, 52, 1734-1742.

[24] K. A. Dill, S. Bromberg, D. Stigter, "Molecular Driving Forces: Statistical Thermodynamics in Chemistry and Biology" *Garland Science*, **(2003)**.

[25] D. W. Van Krevelen, K. T. Nijenhuis. "Properties of polymers: their correlation with chemical structure; their numerical estimation and prediction from additive group contributions" *Elsevier*, **(2009)**.

[26] H. Elbs, G. Krausch, *Polymer* **2004**, 45, 7935-7942.

[27] E. A. Men'shikov, A. V. Bol'shakova, I. V. Yaminskii. *Protection of Metals and Physical Chemistry of Surfaces* **2009**, 45, 295-299.

[28] J. M. V. A. Koelman, P. J. Hoogerbrugge. *Europhys. Lett.* **1993**, 21, 363.

[29] E. S. Boek, P. V. Coveney, H. N. W. Lekkerkerker, P. P. A. M. van der Schoot, *Phys. Rev. E*, **1997**, 55, 3124.

[30] M. Calvaresi, M. Dallavalle, F. Zerbetto, *Small* **2009**, 5, 2191-2198.

[31] J. C. Shillcock, R. Lipowsky, *J. Chem. Phys.* **2002**, 117, 5048−5061.

[32] D. A. Fedosov, B. Caswell, G. E. Karniadakis, *Biophysical journal* **2010**, 98, 2215-2225.

[33] D. A. Fedosov, W. Pan, B. Caswell, G. Gompper, G. E. Karniadakis, *PNAS* **2011**, 108, 11772-11777.

[34] D. A. Fedosov, H. Lei, B. Caswell, S. Suresh, G. E. Karniadakis, *PLoS computational biology*, **2011**, 7, e1002270.

[35] L. Bai, D. Breen, *Journal of Graphics, GPU, and Game Tools* **2008**, 13, 53-60.

[36] K. M. Kadish, R. S. Ruoff, "Fullerenes: Chemistry, Physics, and Technology" *Wiley-Interscience*, New York, **(2000)**.

[37] P. Zhang, J. Lu, Q. Xue, W. Liu, *Langmuir* **2001**, 17, 2143–2145.

[38] S. Bosi, T. Da Ros, G. Spalluto, M. Prato, *Eur. J. Med. Chem.* **2003**, 38, 913–923

[39] N. O. Mchedlov-Petrossyan, *Chem. Rev.* **2013**, 113, 5149–5193

[40] P. J. Linstrom, W. G. Mallard, NIST Chemistry WebBook, NIST Standard Reference Database Number 69, July **2001**, National Institute of Standards and Technology, Gaithersburg, MD 20899 (http://webbook.nist.-gov).

[41] B. Zhang, M. Cho, J. B. Hughes, J.-H. Kim, *Environ. Sci. Technol.* **2009**, 43, 9124–9129.

[42] D. Y. Lyon, L. K. Adams, J. C. Falkner, P. J. J. Alvarez, *Environ. Sci. Technol.* **2006**, 40, 4360–4366.

[43] R. Qiao, A. P. Roberts, A. S. Mount, S. J. Klaine, P. C. Ke, *Nano Lett.* **2007**, 7, 614–619

[44] S. Deguchi, S. Mukai, M. Tsudome, K. Horikoshi, *Adv. Mater.* **2006**, 18, 729–732.

[45] G. V. Andrievsky, M. V. Kosevich, O. M. Vovk, V. S. Shelkovsky, L. A. Vashchenko, *J. Chem. Soc. Chem.* **1995**, 1281–1282.

[46] S. Deguchi, R. G. Alargova, K. Tsujii, *Langmuir* **2001**, 17, 6013–6017.

[47] A. Hirsch, *Angew. Chem. Int. Ed. Engl.* **1993**, 32, 1138 –1141.

[48] D. Canevet, E. M. Pérez, N. Martín, *Angew. Chem. Int. Ed.* **2011**, 50, 9248–9259

[49] E. M. Pérez, N. Martín, *Pure Appl. Chem.* **2010**, 82, 523–533

[50] M. Calvaresi, F. Zerbetto, *Nanoscale* **2011**, 3, 2873–2881

[51] A. Beeby, J. Eastoe, R. K. Heenan, *J. Chem. Soc. Chem. Commun.* **1994**, 173–175

[52] S. A. Jenekhe, X. L. Chen, *Science* **1998**, 279, 1903–1907

[53] H. Hungerbuehler, D. M. Guldi, K. D. Asmus, *J. Am. Chem. Soc.* **1993**, 115, 3386–3687

[54] B. Todorovic´ Markovic´, V. Jokanovic´, S. Jovanovic´, D. Kleut, M. Dramic´anin, Z. Markovic´, *Appl. Surf. Sci.* **2009**, 255, 7537–7541.

[55] M. Reiher, A. Hirsch, *Chem. Eur. J.* **2003**, 9, 5442–5452.

[56] M. Calvaresi, M. Dallavalle, F. Zerbetto, *Small* **2009**, 5, 2191–2198.

[57] F. Palazzesi, M. Calvaresi, F. Zerbetto, *Soft Matter* **2011**, 7, 9148–9156.

[58] J. N. Israelachvili, "Intermolecular and Surface Forces" *Academic Press*, New York, **(1991)**.

[59] I. Ramakanth, A. Patnaik, *Carbon* **2008**, 46, 692–698.

[60] J. D. Fortner, D. Y. Lyon, C. M. Sayes, A. M. Boyd, J. C. Falkner, E. M. Hotze, L. B. Alemany, Y. J. Tao, W. Guo, K. D. Ausman, V. L. Colvin, J. B. Hughes, *Environ. Sci. Technol.* **2005**, 39, 4307–4316

[61] R. J. Hickey, B. L. Sanchez-Gaytan, W. Cui, R. J. Composto, M. Fryd, B. B. Wayland, S.-J. Park, *Small*

2010, 6, 48–51.

[62] H. Li, J. Hao, *J. Phys. Chem. B* **2007**, 111, 7719–7724.

[63] Y. Wang, Y. Li, J. Costanza, L. M. Abriola, K. D. Pennell, Environ. Sci. Technol.2012, 46, 11761–11769.

[64] Y. I. Prylutskyy, A. S. Buchelnikov, D. P. Voronin, V. V. Kostjukov, U. Ritter, J. A. Parkinson, M. P. Evstigneev, *Phys. Chem. Chem. Phys.* **2013**, 15, 9351–9360

[65] J. Lee, J.-H. Kim, *Environ. Sci. Technol.* **2008**, 42, 1552–1557.

[66] . J. Park, O.-H. Kwon, K.-S. Lee, K. Yamaguchi, D.-J. Jang, J.-I. Hong, *Chem. Eur. J.* **2008**, 14, 5353–5359

[67] T. Tsoufis, V. Georgakilas, X. Ke, G. Van Tendeloo, P. Rudolf, D. Gournis, *Chem. Eur. J.* **2013**, 19, 7937–7943

[68] A. Mrzel, A. Mertelj, A. Omerzu, M. Cˇ opicˇ, D. Mihailovic, *J. Phys. Chem. B* **1999**, 103, 11256–11260.

[69] Culgi 4.0.1 program, http://www.culgi.com/default.asp.

[70] J. R. Lu, Z. X. Li, R. K. Thomas, E. J. Staples, I. Tucker, J. Penfold, *J. Chem. Phys.* **1993**, 97, 8012–8020.

[71] R. D. Groot, K. L. Rabone, *Biophys. J.* **2001**, 81, 725–736.

[72] K. Kostarelos, K. S. Novoselov, *Science* **2014**, 344, 261−263.

[73] L. Feng, Z. Liu, *Nanomedicine* **2011**, 6, 317−324.

[74] V. C. Sanchez, A. Jachak, R. H. Hurt, A. B.Kane, *Review. Chem. Res. Toxicol.* **2012**, 25, 15−34.

[75] P. Nguyen, V. Berry, *J. Phys. Chem. Lett.* **2012**, 3, 1024−1029.

[76] Y. Zhang, T. R. Nayak, H. Hong, W. B. Cai, *Nanoscale* **2012**, 4, 3833−3842.

[77] C. Cha, S. R. Shin, N. Annabi, M. R. Dokmeci, A. Khademhosseini, *ACS Nano* **2013**, 7, 2891−2897.

[78] C. Chung, Y.-K. Kim, D. Shin, S.-R. Ryoo, B. H. Hong, D.-H. Min, *Acc. Chem. Res.* **2013**, 46, 2211−2224.

[79] A. Servant, A. Bianco, M. Prato, K. Kostarelos, *Bioorg. Med. Chem. Lett.* **2014**, 24, 1638−1649.

[80] R. Zhou, H. Gao, *Wiley Interdiscip. Rev.: Nanomed. Nanobiotechnol.* **2014**, 6, 452−474.

[81] A. Bianco, *Angew. Chem., Int. Ed.* **2013**, 52, 4986−4997.

[82] W. Hu, C. Peng, W. Luo, M. Lv, X. Li, D. Li, Q. Huang, C. Fan, *ACS Nano* **2010**, 4, 4317−4323.

[83] O. Akhavan, E. Ghaderi, *ACS Nano* **2010**, 4, 5731−5736.

[84] Y. Zhang, S. F. Ali, E. Dervishi, Y. Xu, Z. Li, D. Casciano, A. S. Biris, *ACS Nano* **2010**, 4, 3181−3186.

[85] K.-H. Liao, Y.-S. Lin, C. W. Macosko, C. L. Haynes, *ACS Appl. Mater. Interfaces* **2011**, 3, 2607−2615.

[86] S. Liu, T. H. Zeng, M. Hofmann, E. Burcombe, J. Wei, R. Jiang, J. Kong, Y. Chen, *ACS Nano* **2011**, 5, 6971−6980.

[87] A. Sasidharan, L. S. Panchakarla, P. Chandran, D. Menon, S. Nair, C. N. R Rao, M. Koyakutty, *Nanoscale* **2011**, 3, 2461−2464.

[88] O. Akhavan, E. Ghaderi, A. Akhavan, *Biomaterials* **2012**, 33, 8017−8025.

[89] S. Liu, M. Hu, T. H. Zeng, R. Wu, R. Jiang, J. Wei, L. Wang, J. Kong, Y. Chen, *Langmuir* **2012**, 28, 12364−12372.

[90] J. Russier, E. Treossi, A. Scarsi, F. Perrozzi, H. Dumortier, L. Ottaviano, M. Meneghetti, V. Palermo, A. Bianco, *Nanoscale* **2013**, 5, 11234−11247.

[91] Y. Li, H. Yuan, A. Von dem Bussche, M. Creighton, R. H. Hurt, A. B. Kane, H. Gao, *Proc. Natl. Acad. Sci. U.S.A.* **2013**, 110, 12295−12300.

[92] Y. Tu, M. Lv, P. Xiu, T. Huynh, M. Zhang, M. Castelli, Z. Liu, Q. Huang, C. Fan, H. Fang, R. Zhou, *Nat. Nanotechnol.* **2013**, 8, 594−601.

[93] T. Lammel, P. Boisseaux, M.-L. Fernández-Cruz, J. M. Navas, *Part. Fibre Toxicol.* **2013**, 10, 27.

[94] J. Tang, Q. Chen, L. Xu, S. Zhang, L. Feng, L. Cheng, H. Xu, Z. Liu, R. Peng, *ACS Appl. Mater. Interfaces* **2013**, 5, 3867−3874.

[95] T.-W. Wang, A. Cao, Y. Jiang, X. Zhang, J.-H. Liu, Y. Liu, H. Wang, *ACS Appl. Mater. Interfaces* **2014**, 6, 2791−2798.

[96] Z. Ding, Z. Zhang, H. Ma, Y. Chen, *ACS Appl. Mater. Interfaces* **2014**, 6, 19797−19807.

[97] J. Linares, M. C. Matesanz, M. Vila, M. J. Feito; G. Gonçalves, M. Vallet-Regí, A. P. Marques, M. T. Portoles, *ACS Appl. Mater. Interfaces* **2014**, 6, 13697−13706.

[98] L. Hui, J.-G. Piao, J. Auletta, K. Hu, Y. Zhu, T. Meyer, H. Liu, L.Yang, *ACS Appl. Mater. Interfaces* **2014**, 6, 13183−13190.

[99] Y. Chang, S.-T. Yang, J.-H. Liu, E. Dong, Y. Wang, A. Cao, Y. Liu, H. Wang, *Toxicol. Lett.* **2011**, 200, 201−210.

[100] J.-H. Liu, S.-T. Yang, H. Wang, Y. Chang, A. Cao, Y. Liu, *Nanomedicine* (London) **2012**, 7, 1801−1812.

[101] C. Bussy, H. Ali-Boucetta, K. Kostarelos, *Acc. Chem. Res.* **2013**, 46, 692−701.

[102] Q. Mu, G. Su, L. Li, B. O. Gilbertson, L. H. Yu, Q. Zhang, Y.-P. Sun, B. Yan, *ACS Appl. Mater. Interfaces* **2012**, 4, 2259−2266.

[103] A. V. Titov, P. Kral, R. Pearson, *ACS Nano* **2010**, 4, 229−234.

[104] R. Guo, J. Mao, L.-T. Yan, *Biomaterials* **2013**, 34, 4296−4301.

[105] J. Wang, Y. Wei, X. Shi, H. Gao, *RSC Adv.* **2013**, 3, 15776−15782.

[106] J. Mao, R. Guo, L.-T. Yan, Nanosheets. *Biomaterials* **2014**, 35, 6069−6077.

[107] J. Liu, J. C. Conboy, *Biophys. J.* **2005**, 89, 2522−2532.

[108] P. F. Devaux, A. Herrmann, N. Ohlwein, M. M. Kozlov, *Biochim. Biophys. Acta* **2008**, 1778, 1591−1600.

[109] Y. Li, Y. Liu, Y. Fu, T. Wei, L. Le Guyader, G. Gao, R. Liu, Y. Chang, C. Chen, *Biomaterials* **2012**, 33, 402−411.

[110] M. Calvaresi, F. Zerbetto, *ACS Nano* **2010**, 4, 2283−2299.

[111] G. Zuo, Q. Huang, G. Wei, R. Zhou, H. Fang, *ACS Nano* **2010**, 4, 7508−7514.

[112] M. Calvaresi, F. Zerbetto, *Nanoscale* **2011**, 3, 2873−2881.

[113] G. Zuo, S.-G. Kang, P. Xiu, Y. Zhao, R. Zhou, *Small* **2013**, 9, 1546−1556.

[114] M. Calvaresi, S. Hoefinger, F. Zerbetto, *Chem.∂Eur. J.* **2012**, 18, 4308−4313.

[115] S.-T. Yang, Y. Liu, Y.-W. Wang, A. Cao, *Small* **2013**, 9, 1635−1653.

[116] M. Calvaresi, F. Zerbetto, *Acc. Chem. Res.* **2013**, 46, 2454−2463.

[117] M. Calvaresi, F. Arnesano, S. Bonacchi, A. Bottoni, V. Calò, S. Conte, G. Falini, S. Fermani, M. Losacco, M. Montalti, G. Natile, L. Prodi, F. Sparla, F. Zerbetto, *ACS Nano* **2014**, 8, 1871−1877.

[118] X. Sun, Z. Feng, T. Hou, Y. Li, *ACS Appl. Mater. Interfaces* **2014**, 6, 7153−7163.

[119] B. Luan, T. Huynh, L. Zhao, R. Zhou, *ACS Nano* **2015**, 9, 663−669.

[120] R. W. Carpick, *Science* **2006**, 313, 184−185.

[121] http://www.gft-ev.de/tribologie.htm.

[122] B. Shen, P. Kalita, A. J. Shih, A. P. Malshe, *Trans. NAMRI/SME* **2008**, 36, 357−364.

[123] H. Wu, R. Yang, B. Song, Q. Han, J. Li, Y. Zhang, Y. Fang, R. Tenne, C. Wang, *ACS Nano* **2011**, 5, 1276−1281.

[124] J. M. Martin, C. Donnet, T. Le Mogne, T. Epicier, *Phys. Rev. B* **1993**, 48, 10583−10586.

[125] T. Onodera, Y. Morita, R. Nagumo, R. Miura, A. Suzuki, H. Tsuboi, N. Hatakeyama, A. Endou, H. Takaba, F. Dassenoy, C. Minfray, L. Joly-Pottuz, M. Kubo, J. Martin, A. Miyamoto, *J. Phys. Chem. B* **2010**, 114, 15832−15838.

[126] M. Stefanov, A. N. Enyashin, T. Heine, G. Seifert, *J. Phys. Chem. C* **2008**, 112, 17764−17767.

[127] J. Tannous, F. Dassenoy, I. Lahouij, T. Le Mogne, B. Vacher, A. Bruhács, W. Tremel, *Tribol. Lett.* **2011**, 41, 55−64.

[128] A. K. Rappe, W. A., III Goddard, *J. Phys. Chem.* **1991**, 95, 3358−3363.

[129] N. Sändig, F. Zerbetto, *Chem.Commun.* **2010**, 46, 667−676.

[130] J. W. Ponder, F. M. Richards, *J. Comput. Chem.* **1987**, 8, 1016−1024.

[131] C. E. Kundrot, J. W. Ponder, F. M. Richards, *J. Comput. Chem.* **1991**, 12, 402−409.

[132] M. J. Dudek, J. W. Ponder, *J. Comput. Chem.* **1995**, 16, 791−816.

[133] R. J. Baxter, G. Teobaldi, F. Zerbetto, *Langmuir* **2003**, 19, 7335−7340.

[134] S. Rapino, F. Zerbetto, *Langmuir* **2005**, 21, 2512−2518.

[135] Y. Zhao, N. E. Schultz, D. G. Truhlar, *J. Chem. Theory Comput.* **2006**, 2, 364−382.

[136] P. J. Hay, W. R. Wadt, *J. Chem. Phys.* **1985**, 82, 270−283.

[137] W. R. Wadt, P. J. Hay, *J. Chem. Phys.* **1985**, 82, 284−298.

[138] P. J. Hay, W. R. Wadt, *J. Chem. Phys.* **1985**, 82, 299−310.

[139] J. D. Fuhr, J. O. Sofo, A. Saúl, *Phys. Rev. B* **1999**, 60, 8343−8347.

[140] Y. Morita, T. Onodera, A. Suzuki, R. Sahnoun, M. Koyama, H. Tsuboi, N. Hatakeyama, A. Endou, H. Takaba, M. Kubo, C. A. Del Carpio, T. Shin-yoshi, N. Nishino, A. Suzuki, A. Miyamoto, *Appl. Surf. Sci.* **2008**, 254, 7618−7621.

[141] V. Varshney, S. S. Patnaik , C. Muratore, A. K. Roy, A. A. Voevodin, B. L. Farmer, *Comput. Mater. Sci.*, **2010**, 48, 101.

[142] U. Becker, K. M. Rosso, R. Weaver, M. Warren, M. F. Hochella, *Geochim. Cosmochim. Acta* **2003**, 67, 923−934.

[143] G. Seifert, H. Terrones, M. Terrones, G. Jungnickel, T. Frauenheim, *Phys. Rev. Lett.* **2000**, 85, 146−149.

[144] P. P. Ewald, *Ann. Phys.* **1921**, 369, 253−287.

[145] T. Liang, S. R. Phillpot, S. B. Sinnott, *Phys. Rev. B* **2009**, 79, 245110 1−14.

[146] T. Onodera, Y. Morita, A. Suzuki, M. Koyama, H. Tsuboi, N. Hatakeyama, A. Endou, H. Takaba, M. Kubo, F. Dassenoy, C. Minfray, L. Joly-Pottuz, J. Martin, A. Miyamoto, *J. Phys. Chem. B* **2009**, 113, 16526−16536.

[147] J. Gao, W. D. Luedtke, D. Gourdon, M. Ruths, J. N. Israelachvili, U. Landman, *J. Phys. Chem. B* **2004**, 108, 3410−3425.

[148] Y. Mo, K. T. Turner, I. Szlufarska, *Nature* **2009**, 457, 1116−1119.

[149] P. Tangney, S. G. Louie, M. L. Cohen, *Phys. Rev. Lett.* **2004**, 93, 065503 1−4.

[150] I. L. Singer, R. N. Bolster, J. Wegand, S. Fayeulle, B. C. Stupp, *Appl. Phys. Lett.* **1990**, 57, 995−997.

[151] H. R. Hertz, "Über die Berührung elastischer Körper in Gesammelte Werke"; *Mohr Siebeck*: Tuebingen, Germany, **(1895)**.

[152] K. J. Wahl, M. Belin, I. L. Singer, *Wear* **1998**, 214, 212−220.

[153] I. B. Bischofs, F. Klein, D. Lehnert, M. Bastmeyer, U. S. Schwarz, *Biophys. J.* **2008**, 95, 3488-96.

[154] K. A. Kilian, B. Bugarija, B. T. Lahn, M. Mrksich, *Proc. Natl. Acad. Sci. USA* **2010**, 107, 4872-4877.

[155] W. L.Murphy, T. C. McDevitt, A. J. Engler, W. L. Murphy, T. C. McDevitt, A. J. Engler, *Nature Mater.* **2014**, 13, 547-557.

[156] D. Wirtz, K. Konstantopoulos, P. C. Searson, *Nat. Rev. Cancer.* **2011**, 11, 512-522.

[157] J. H. S. R. L. Hildebrand, "Regular solutions." *Englewood Cliffs,* N. J., **(1962)**.

[158] P. J. Flory, "Principles of polymer chemistry.", *Cornell University Press*, Ithaca, **(1953)**.

[159] A. P. Lyubartsev, A. Laaksonen, *Phys. Rev. E* **1995**, 52, 3730-3737.

[160] A. K. Soper, *Chemical Physics* **1996**, 202, 295-306.

[161] F. Muller-Plathe, *ChemPhysChem* **2002**, 3, 755-769.

[162] A. Lyubartsev, A. Mirzoev, L. J. Chen, A. Laaksonen, *Faraday Discuss.* **2010**, 144, 43-56.

[163] A. Chaimovich, M. S. Shell, *J. Chem. Phys.* **2011**, 134, 094112.

[164] Y. Ni, M. Y. M. Chiang, *Soft Matter* **2007**, 3, 1285-1292.

[165] S. Banerjee, R. Sknepnek, M. C. Marchetti, *Soft Matter* **2014**, 10, 2424-2430.

[166] I. B. Bischofs, S. S. Schmidt, U. S. Schwarz, *Phys. Rev. Lett.* **2009**, 103, 048101.

[167] X. Zeng, S. Li, J. Mech. *Behav. Biomed. Mater.* **2011**, 4, 180-189.

[168] J. L. Jones, M. Lal, J. N. Ruddock, N. A. Spenley, *Faraday Discuss.*, **1999**, 112, 129-142.

[169] M.J. Dalby, N. Gadegaard, R.O.C. Oreffo, *Nature Mater.* **2014**, 13, 558-569.

[170] W. R. Holmes, L. Edelstein-Keshet, *PLoS Comput. Biol.* **2012**, 8, e1002793.

[171] A. Mogilner, *J. Math. Biol.* **2009**, 58, 105-134.

[172] D. Shao, H. Levine, W.-J. Rappel, *Proc. Natl. Acad. Sci. USA* **2012**, 109, 6851-6856.

[173] E. Jabbarzadeh, C. F. Abrams, *J. Theor. Biol.* **2005**, 235, 221-232.

[174] M. C. Kim, D. M. Neal, R. D. Kamm, H. H. Asada, *PLoS Comput Biol* **2013**, 9, e1002926.

[175] S. V. Satyanarayana, A. Baumgaertner, *J. Chem. Phys.* **2004**, 121, 4255-4265.

[176] D. Campos, V. Méndez, I. Llopis, *J. Theor. Biol.* **2010**, 267, 526-534.

[177] A. A. Potdar, J. Jeon, A. M. Weaver, V. Quaranta, P. T. Cummings, *PLoS One* **2010**, 5, e9636.

[178] P. Dieterich, R. Klages, R. Preuss, A. Schwab, *Proc. Natl. Acad. Sci. USA* **2008**, 105, 459-463.

[179] T. H. Harris, E. J. Banigan, D. A. Christian, C. Konradt, E. D. Tait Wojno, K. Norose,   E. H. Wilson, B. John, W. Weninger, A. D. Luster, A. J. Liu, C. A. Hunter, *Nature* **2012**, 486, 545-548.

[180] M. Le Berre, Y.-J. Liu, J. Hu, P. Maiuri, O. Bénichou, R. Voituriez, Y. Chen, M. Piel, *Phys. Rev. Lett.* **2013**, 111, 198101.

[181] T. D. Yang, J.-S. Park, Y. Choi, W. Choi, T.-W. Ko, K. J. Lee, *PLoS ONE* **2011**, 6, e20255.

[182] D. J. Cohen, W. J. Nelson, M. M. Maharbiz, *Nature Mater.* **2014**, 13, 409-417.

[183] Y. Hegerfeldt, M. Tusch, E. B. Broecker. P. Friedl, *Cancer Res.* **2002**, 62, 2125-2130.

[184] J. P. Thiery, *Nat Rev Cancer* **2002**, 2, 442-454.

[185] D. Drasdo, S. Hoehme, M. Block, *J. Stat. Phys.* **2007**, 128, 287-345.

[186] I. Ramis-Conde, D. Drasdo, A. R. A. Anderson, M. A. J. Chaplain, *Biophys. J.* **2008**, 95, 155-165.

[187] F. Graner, J. A. Glazier, *Phys. Rev. Lett.* **1992**, 69, 2013-2016.

[188] J. A.Glazier, F. Graner, *Phys. Rev. E* **1993**, 47, 2128-2154.

[189] P. Gerlee, A. R. Anderson, *J. Theor. Biol.* **2007**, 246, 583-603.

[190] M. A. Stolarska, Y. Kim, H. G. Othmer, *Philos Trans. A. Math. Phys. Eng. Sci.* **2009**, 367, 3525-53.

[191] P. Macklin, S. McDougall, A. R. A. Anderson, M. A. J Chaplain, V. Cristini, J. Lowengrub, *J. Math. Biol.* **2009**, 58, 765-798.

[192] A. Gerisch, M. A. Chaplain, *J. Theor. Biol.* **2008**, 250, 684-704.

[193] M. Basan, J. Prost, J.-F. Joanny, J. Elgeti, *Phys. Biol.* **2011**, 8, 026014.

[194] J. Jeon, V. Quaranta, P. T. Cummings, *Biophys. J.* **2010**, 98, 37-47.

[195] N. Sepulveda, L. Petitjean, O. Cochet, E. Grasland-Mongrain, P. Silberzan, V. Hakim, *PLoS Comput. Biol.* **2013**, 9, e1002944.

[196] F. Frascoli, B. D. Hughes, M. H. Zaman, K. A. Landman, *PLoS One* **2013**, 8, e59249.

[197] A. D. Celiz, J. G. W. Smith, R. Langer, D. G. Anderson, D. A. Winkler, D. A. Barrett, M. C. Davies, L. E. Young, C. Denning, M. R. Alexander, *Nature Mater.* **2014**, 13, 570-9.

[198] S. Pagliara, K. Franze, C. R. McClain, G. Wylde, C. L. Fisher, R.J.M. Franklin, A.J. Kabla, U.F. Keyser, K. J. Chalut, *Nature Mater.* **2014**, 13, 638-644.

[199] C. Yang, M. W. Tibbitt, L. Basta, K. S. Anseth, *Nature Mater.* **2014**, 13, 645-652.

[200] T. Alfrey, E. F. Gurnee, W. G. Lloyd, *J. Polym. Sci. Part C* **1966**, 12, 249-261.

[201] J. S. Vrentas, C. M. Jarzebski, J. L. Duda, *AIChE J.* **1975**, 21, 894-901.

[202] F. Adib, P. Neogi. "Sorption with oscillations in solid polymers." *AIChE J.* **1987**, 33, 164-166.

[203] A. R. Berens, H. B. Hopfenberg, *Polymer* **1978**, 19, 489-496.

[204] R. W. Korsmeyer, S. R. Lustig, N. A. Peppas, *J. Polym. Sci. Part B Polym. Phys.* **1986**, 24, 395-408.

[205] www.comsol.com

[206] H. Fujita, "Diffusion in polymer-diluent systems" *Springer*, Berlin Heidelberg, **(1961)**.

[207] M. Uchidoi, A. Keiichiro, Y. Ishida, *Polym. J.* **1978**, 10, 161-167.

[208] J. Crank, "The mathematics of diffusion.", *Oxford Science Publication*, **(1975)**.

[209] J. Crank, *J. Polym. Sci.* **1953**, 11, 151-168.

[210] E. Jenckel, *Z Elktrochem Angew* **1937**, 43, 796-806.

[211] X. S. Wu, N. Wang. *J. Biomater. Sci., Polym. Ed.* **2001**, 12, 21-34.

[212] R.P. Feynman, R.B. Leighton, M. Sands, "The Feynman Lectures in Physics" *Addison-Wesley*, **(1963)**.